Important Notice

UNIVERSITY OF CALGARY

Seismic Signal Enhancement Using Time-Frequency Transforms

by

Victor Iliescu

A THESIS

SUBMITTED TO THE FACULTY OF GRADUATE STUDIES

IN PARTIAL FULFILLMENT OF THE REQUIREMENTS FOR THE

DEGREE OF MASTER OF SCIENCE

DEPARTMENT OF GEOLOGY AND GEOPHYSICS

CALGARY, ALBERTA

September, 2002

THE UNIVERSITY OF CALGARY

FACULTY OF GRADUATE STUDIES

The undersigned certify that they have read, and recommended to the Faculty of Graduate Studies for acceptance the thesis entitled "Seismic Signal Enhancement Using Time-Frequency Transforms" submitted by Victor Iliescu in partial fulfillment of the requirements for the degree of Master of Science.

_____

Supervisor, G., F. Margrave, Geology and Geophysics

_____

Dr. Larry Lines, Geology and Geophysics

_____

Dr. John Bancroft, Geology and Geophysics

_____

Dr. Len Bos, Mathematics and Statistics

September, 25, 2002
Date

ii

ABSTRACT

Two transforms (the Gabor transform, based on the Fourier transform, and the wavelet transform) are investigated and employed to achieve an increased temporal resolution of the seismic data. Unlike the Fourier transform, which maps a time series into a totally abstract domain, called the frequency domain, or the Fourier domain, the Gabor transform maps the time series into a joint time-frequency domain, called the Gabor domain. The Gabor domain, is suitable to analyze the data simultaneously in time and frequency, and to design, test, and evaluate new processing techniques. The hyperbolic smoother designed in the Gabor domain represents the main achievement of this thesis. It is shown that the Gabor deconvolution with the hyperbolic smoother successfully corrects the seismic data for the effects of anelastic attenuation and source signature, and effectively restores the relative amplitudes.

Two methods of using the wavelet transform in seismic signal analysis are also investigated in this research. The wavelet transform spectral whitening technique is a method introduced and investigated for the first time, similar to the classical time variant spectral whitening method. The second method, the wavelet transform filtering by semblance weighting, represents also a new technique, which demonstrates that the wavelet domain is suitable for suppressing random noise and enhancing the resolution of subtle stratigraphic features.

ACKNOWLEDGEMENTS

TABLE OF CONTENTS

LIST OF FIGURES

CHAPTER 1

1. STATIONARY DECONVOLUTION

1.1 Introduction

One of the most important steps in a seismic processing flow is the deconvolution process. Deconvolution appeared very early in the development of the digital signal processing methods. The deconvolution process was not present in the analog processing era and for this reason is considered a relatively modern technique (Robinson and Osman, 1996). A novel approach of deconvolution will be presented in this thesis, along with several classical methods for comparison. The classical approach of deconvolution uses approximations that hold for time-invariant convolutional models within limited temporal regions (i.e., time gates), or employ complementary techniques, such as time variant spectral whitening (TVSW) or gain correction. As a counterpart to these robust methods, in this work several time-varying methods of deconvolution are presented, as well as signal enhancement techniques based on nonstationary transforms such as short time Fourier transform (STFT), also called Gabor transform or windowed Fourier transform, and the wavelet transform (WT).

1.2 Wiener spiking deconvolution

The least-squares concept of the Wiener spiking deconvolution for a stationary seismic waveform will be herein explained. A seismic signal (e.g. recorded trace) is the result of a superposition of wavelets of constant shape (in the stationary case) weighted by the reflectivity series (Robinson and Treitel, 1980), thus it can be modeled as a convolution between the source signature (the embedded wavelet) and the reflectivity series. The purpose of deconvolution is to remove the embedded wavelet and thereby, maximize the vertical resolution of the seismic image (Berkhout, 1996). The

convolutional model used in the Wiener spiking deconvolution method is the simplest accepted model for the 1-D seismogram, however, this is not the only option to model a seismic trace. An extension to the convolutional model presented here is the surface consistent model, where the seismic trace is decomposed into the convolutional effects of source, receiver, offset, and earth's reflectivity (Taner and Coburn, 1981). Later in this thesis a nonstationary extension of the convolutional model that describes attenuation will be also presented.

1.2.1 The stationary convolutional model

The mathematical representation of the stationary convolutional model without noise and multiples is

$$s(t) = \int_{-\infty}^{\infty} w(t - \tau) r(\tau) d\tau \equiv w(t) \bullet r(t) = (w \bullet r)(t), \tag{1.1}$$

where "$\bullet$" denotes convolution, $w(t)$ - represents the source signature, also called the embedded wavelet, and $r(t)$ represents the reflectivity.

Stationary means that the shape of the wavelet doesn't change as it propagates through the medium. Computationally, Equation (1.1) can be represented by a multiplication between a Toeplitz matrix (representing the wavelet) with a time series vector representing the reflectivity series (shown in Figure 1.1) (e.g. Margrave, 1999).
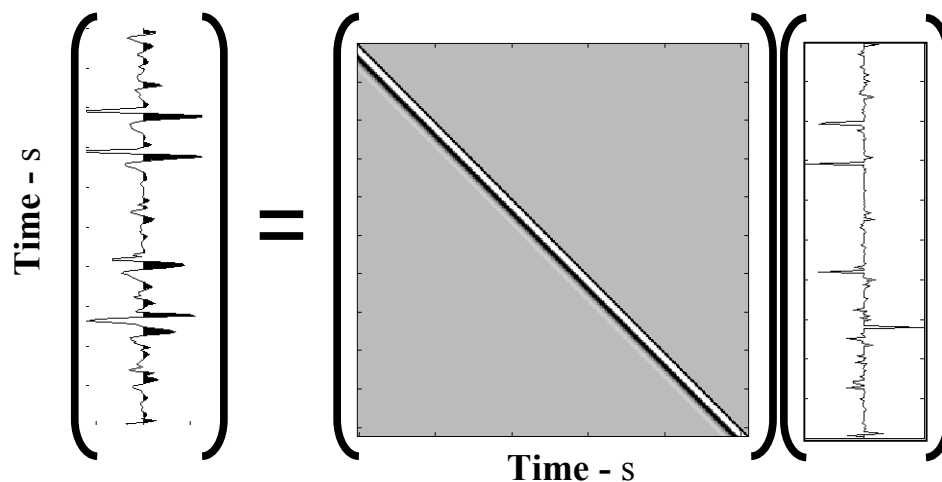
Figure 1.1.: Trace representation in time domain. The trace (column vector, on the left) is the result of the convolution (the convolution in time domain is seen as a matrix multiplication) between a minimum-phase seismic wavelet (time-shifted in the Toeplitz matrix, the square matrix in the center) and the reflectivity series (the column vector, on the right), (after Margrave, 1998).

When the signal is directed at normal incidence upon an interface between two media, the reflectivity coefficient r, relates incident and reflected trace amplitudes (Robinson and Treitel, 1980)

$$r = \frac{v_2\rho_2 - v_1\rho_1}{v_1\rho_1 + v_2\rho_2},\qquad (1.2)$$

where the product between the velocity (v_i) and the density (ρ_i) represents the acoustic impedance of a rock layer. From Equation (1.2) it can be observed that each boundary between different layers, with different impedances, generates a nonzero reflection coefficient.

1.2.2 Wiener spiking filter

The goal of the deconvolution is to estimate the reflectivity series, $r(t)$, given the seismic trace $s(t)$, and therefore, increase the resolution of the seismic image. Equation

(1.1) is considered the main model for stationary deconvolution and asserts that the wavelet, $w(t)$ is stationary. Recently, the theory of deconvolution evolved toward a more realistic, time-variant case explained in chapter 2. Here, the stationary case will be discussed.

The spiking deconvolution filter is designed such that the error between the real reflectivity and the estimated reflectivity is minimum. According to Robinson and Treitel, (1980) the least-squares error has the form:

$$I = \sum_t \left(r(t) - r_{est}(t) \right)^2 ,\tag{1.3}$$

where $r(t)$ is the desired output and $r_{est}(t)$ is the estimated reflectivity (i.e., the spiking filter output) and I denotes the error. The spiking filter output represents the convolution between the trace, $s(t)$, with an unknown filter, the deconvolution operator, $d_{op}(t)$, which is basically the inverse of the wavelet, $w(t)$, in the least square sense.
Thus,

$$r_{est}(t) = s(t) \bullet d_{op}(t).\tag{1.4}$$

The deconvolution operator (the inverse filter) and the wavelet should satisfy the equation

$$w(t) \bullet d_{op}(t) = 1.\tag{1.5}$$

where "1" denotes a vector with value of one for the first sample and zeros for all other samples.

Assuming that the wavelet is causal (see section 1.3 for a definition of causality) and using the matrix notation for discrete signals, Equation (1.5) can be written

$$\begin{bmatrix} w_0 & 0 & 0 & 0 \\ w_1 & w_0 & 0 & 0 \\ w_2 & w_1 & w_0 & 0 \\ \vdots & w_2 & w_1 & \ddots \end{bmatrix} \begin{bmatrix} d_0 \\ d_1 \\ d_2 \\ \vdots \end{bmatrix} = \begin{bmatrix} 1 \\ 0 \\ 0 \\ \vdots \end{bmatrix} \tag{1.6}$$

The zeros above the main diagonal in the wavelet matrix express the causality property of the wavelet. As explained in section 1.3, the inverse filter, denoted by the column vector "d_i," is also causal. Equations (1.5) and (1.6) also hold for the deterministic case where the wavelet is known (i.e., recorded source signature) and its inverse can be calculated without considering the least square problem presented from the beginning in this section. The difference between the inverse filtering and least-squares inverse filtering is that in the inverse filtering situation, the source waveform is assumed to be known, whereas in the Wiener deconvolution case the source waveform is unknown and the solution to the deconvolution problem is optimal in the least square sense (Yilmaz, 1987). Therefore, the terminology refers to the inverse filtering using the recorded source signature as the deterministic deconvolution whereas the Wiener type of deconvolution is known as the statistical deconvolution.

To obtain an exact solution in the statistical case, when the source signature is not known, an infinite number of rows are necessary in Equation 1.6. This problem can become meaningful for computation on a digital computer if we limit the number of coefficients of the filter (Robinson and Treitel, 1980), respectively the number of equations, obtaining an approximate solution for the inverse filter. The size of the inverse operator in samples is chosen smaller than the size of the wavelet (the number of rows in the wavelet matrix), therefore in Equation 1.6 there are more equations than unknowns, leading to the least squares approach in finding the terms of the inverse filter. Equation 1.6 can be written in a matrix form as

$$W \underline{D} = \underline{U} \ , \tag{1.7}$$

where W is the wavelet matrix, $\underline{D}$ is the inverse filter (or the deconvolution operator), and $\underline{U}$ is the unit vector, representing the desired unit spike at the zero lag. The normal equations are formed by multiplying from left by W^T, the transposed W matrix

$$W^T W \underline{D} = W^T \underline{U}. \tag{1.8}$$

In matrix notation, the multiplication by the transposed wavelet matrix, W^T, means that on the left hand side results the autocorrelation of the wavelet that multiplies the inverse filter. On the right hand side, instead of the unity vector the result is a scaled vector. Next, the scaled vector on the right is set to 1,

$$\begin{bmatrix} \Phi_0 & \Phi_1 & \Phi_2 & \cdots \\ \Phi_1 & \Phi_0 & \Phi_1 & \cdots \\ \Phi_2 & \Phi_1 & \Phi_0 & \cdots \\ \vdots & \vdots & \vdots & \ddots \end{bmatrix} \begin{bmatrix} d_0 \\ d_1 \\ d_2 \\ \vdots \end{bmatrix} \cong \begin{bmatrix} 1 \\ 0 \\ 0 \\ \vdots \end{bmatrix}. \tag{1.9}$$

In the system of Equations 1.9 the number of equations equals the number of unknowns (e.g., form a square set), therefore, is suitable for determination of the deconvolution operator, d. To conclude the derivation so far, starting from the system of equations (1.6), after several manipulations, in equations (1.9) only the autocorrelation of the unknown wavelet is necessary to determine its inverse, within a scale factor. Next, the autocorrelation of the wavelet can be approximated with the autocorrelation of the trace if the white noise assumption of the reflectivity is invoked. The autocorrelation of the trace can be obtained by convolving the trace by the time-reversed version of the trace

$$\Phi_{ss}(t) = s(t) \bullet s(-t). \tag{1.10}$$

Following from the convolutional model (Equation 1.1), the autocorrelation of the trace can be further developed

$$\Phi_{ss}(t) = [w(t) \bullet r(t)] \bullet [w(-t) \bullet r(-t)]. \qquad (1.11)$$

Regrouping the terms,

$$\Phi_{ss}(t) = [w(t) \bullet w(-t)] \bullet [r(t) \bullet r(-t)] = \Phi_{ww}(t) \bullet \Phi_{rr}(t). \qquad (1.12)$$

Assuming the reflectivity is a random sequence (has statistical properties of a random noise), its autocorrelation function has the form

$$\Phi_{rr}(t) = P\delta(0), \qquad (1.13)$$

where $\delta(0)$ is a spike (e.g. a unit impulse also called a delta distribution) at zero lag, scaled by its power, P. In the terminology proposed by Robinson and Treitel (1980), the power of a white noise series (the reflectivity series in this case) means the sum of squares of its amplitudes divided by the elapsed time, as time becomes infinite

$$P = \lim_{T \to \infty} \frac{1}{2T+1} \left(r_{-T}^2 + r_{-T+1}^2 + ... + r_{-1}^2 + r_0^2 + r_1^2 + ... + r_T^2 \right), \qquad (1.14)$$

where, T is the sampled observation time which tends to infinity and r is the reflectivity assumed as an infinitely long realization. Thus, we can estimate the autocorrelation of the wavelet from the autocorrelation of the trace by choosing a certain number of lags (windowing the autocorrelation) for the autocorrelation of the trace. The number of lags must be large enough such that, the power of the white noise denoted by P in relations (1.13) and (1.14) represents a scaling factor close to 1 ($P \cong 1$). Therefore, Equation (1.12) becomes

$$\Phi_{ww}(t) \cong \Phi_{ss}(t), \quad where \quad |t| \leq t_{\max} > 0. \qquad (1.15)$$

By windowing the autocorrelation a finite number of equations is included in the solution of the Wiener filter and the number of equations defines the length of the deconvolution operator in a deconvolution algorithm.

In Equation (1.9), the deconvolution operator can be determined using a windowed version of the autocorrelation of the trace. It follows that an estimate of the reflectivity can be obtained using Equation (1.4).

In the Wiener deconvoluion case, the only assumptions necessary in deriving the deconvolution operator are that the wavelet and its inverse are causal and the reflectivity has statistical properties of white noise (e.g. is random). It turns out that a causal wavelet with a causal inverse has the minimum-phase spectrum.

The minimum-phase wavelet can be reconstructed using the Hilbert transform. Often, the concept of minimum phase-lag refers to the frequency domain whereas in time domain the equivalent terminology uses the term "minimum delay" (Robinson and Treitel, 1980). There are at least two ways to compute the minimum phase wavelet. One way, is to compute the minimum phase wavelet from its autocorrelation function (Leinbach, 1996), using the autocorrelation function of the trace as described above. Another way is to compute the phase of the minimum-phase wavelet from its Fourier amplitude spectrum, then, using the inverse Fourier transform, the wavelet in the time domain is obtained. A detailed description of the minimum-phase concept is presented in section 1.2.4.

1.2.3 Frequency domain equivalent of the Wiener spiking filter

In the frequency domain, the convolutional model described by Equation (1.1) is

$$\hat{s}(f) = \hat{w}(f)\hat{r}(f), \tag{1.16}$$

where $\hat{s}(f)$, represent the Fourier spectrum of the trace $s(t)$, $\hat{w}(f)$ is the Fourier spectrum of the source signature, and $\hat{r}(f)$ represents the Fourier spectrum of the reflectivity series, $r(t)$. It can be observed from Equation (1.16) that the deconvolution

can be explained through a spectral factorization problem. In Equation (1.16), there are two unknowns ($\hat{w}(f)$ and $\hat{r}(f)$) and only one known, respectively $\hat{s}(f)$). Thus, $\hat{s}(f)$ must be separated into its factors, $\hat{w}(f)$ and $\hat{r}(f)$. In order to solve this equation for the reflectivity, some assumptions, which come from statistical properties explained in section 1.2.2, are required.

In the frequency domain the wavelet is characterized by its amplitude and phase spectrum. In designing the deconvolution operator in the frequency domain only the absolute values (meaning the amplitude spectrum) of the spectra in Equation (1.16) are used

$$\left|\hat{s}(f)\right| = \left|\hat{w}(f)\right|\left|\hat{r}(f)\right|. \tag{1.17}$$

Windowing the autocorrelation in time domain (described in the previous section) is equivalent to smoothing the power spectrum (squared amplitude spectrum) in frequency domain. Commonly the smoothing operation is performed on the Fourier amplitude spectrum instead. To make Equation (1.17) meaningful, the reflectivity is considered finite in time and bandlimited in frequency. Thus, a smoothed version of the reflectivity magnitude spectrum will be close to a constant, which can be set to 1 for all frequencies in the bandwidth, $\left|\overline{\hat{r}(f)}\right| \cong 1$ (the overbar denotes a smoothed term). Then, similar to section 1.2.2, smoothing the magnitude spectrum of the trace an estimate of the magnitude spectrum of the wavelet will be provided. The length of the smoother in frequency is inversely related to the length in time of the autocorrelation window in the Wiener deconvolution case. Thus, the deconvolution operator (denoted by D_{op} in the following equation) in the frequency domain can be determined similarly to the time domain ignoring the influence of the reflectivity series on the filter design

$$\left|D_{op}\right| = \frac{1}{\left(\left|\overline{\hat{s}(f)}\right| + \mu A_{\max}\right)}, \tag{1.18}$$

where μ is a small real number and A_{max} is the maximum value of the smoothed Fourier spectrum introduced to avoid any division by zero. In Equation (1.18) the wavelet and the reflectivity function have no common support, and therefore by smoothing the amplitude spectrum of the trace only an approximation of the embedded wavelet will be provided. More precisely, the inequality

$$\left|\hat{w}(f)\right| \neq \left|\overline{\hat{s}(f)}\right| \left|\overline{\hat{r}(f)}\right|, \tag{1.19}$$

can be approximated as an equality in many useful situations.

For the phase calculation of the deconvolution operator, the minimum-phase assumption is used. Therefore, the minimum-phase spectrum is given by

$$\phi(f) = H\left[\ln\left(\hat{s}(f)\right)\right], \tag{1.20}$$

where H denotes the Hilbert transform (see section 1.3 for a review of the minimum-phase concept).

1.3 Minimum-phase assumption versus zero-phase

1.3.1 Minimum-phase wavelet

Any filter (e.g. the wavelet or its inverse, the ideal deconvolution operator) is characterized by its transfer function (Robinson and Treitel, 1980). The transfer function is defined as the ratio of the output over the input (in the frequency domain). In the time domain, the equivalent of the transfer function is the impulse response of the filter (Sheriff, 1997). In the frequency domain, the magnitude of the transfer function is the filter's magnitude spectrum whereas the phase of the transfer function is known as the filter's phase spectrum. When referring to the phase of a filter, the "phase delay" is often used rather than the term "phase" (Robinson and Treitel, 1980). In this work also, any time when the term "minimum-phase" is used it must be understood as "minimum-phase delay" in the sense that Robinson and Treitel proposed. Writing the transfer function in polar form, the phase and the magnitude spectrum of the filter are given explicitly

$$\hat{w}(\omega) = |\hat{w}(\omega)| e^{i\psi(\omega)}, \qquad (1.21)$$

where ω is the angular frequency, $|\hat{w}(\omega)|$ is the magnitude spectrum of the filter, and $\psi(\omega)$, is the phase spectrum of the filter. The phase lag spectrum is defined as the negative of the phase spectrum (Robinson and Treitel, 1980)

$$\phi(\omega) = -\psi(\omega) = -\tan^{-1}\left(\frac{\text{Im}(\hat{w}(\omega))}{\text{Re}(\hat{w}(\omega))}\right), \qquad (1.22)$$

and Equation (1.21) is written as

$$\hat{w}(\omega) = |\hat{w}(\omega)| e^{-i\phi(\omega)}. \qquad (1.23)$$

In many situations, the field data approximate the convolutional model presented in section 1.2.1 but most of the time the real data is more complex, e.g. it can include more than one embedded wavelet. For example a surface waveform can interfere with a minimum phase reflection wavelet and the resulting seismogram will be in a non-minimum phase state. The convolutional model is also violated by multiple waves, commonly present in the field data. A more precise convolutional model would also include the background noise, which is considered as an additive signal. Thus, the seismogram in the stationary case is more completely represented by

$$s(t) = r(t) \bullet m(t) \bullet w(t) + n(t) , \qquad (1.24)$$

where $r(t)$ and $w(t)$ are the same as in Equation (1.1), $m(t)$ represents the multiple operator and $n(t)$ is the background noise. The multiple suppression process is not investigated in this thesis and all data are considered multiple free. However, it is important to mention that the minimum phase assumption is mandatory in removing the multiples using prediction-error filters (an extension of the Wiener filter presented in section 1.2.2) and is linked to the causality property also invoked in the development of the constant Q model of attenuation (explained in section 1.4). At the same time, zero phase filtering can suppress undesired waveforms to move the data towards the minimum phase state as an operation applied before the deconvolution in situations where the signal to noise ratio is very low (the background noise is very high), (Margrave, 1999).

A wavelet is defined as minimum phase if it is causal, has finite energy and its inverse is also causal and has finite energy (Robinson and Treitel, 1980). Thus, the minimum phase concept includes three important properties: causality, invertability and finite energy.

Causality is expressed mathematically by the Heaviside step function:

$$h(t) = \frac{1}{2}(1 + \text{sgn}(t)), \qquad (1.25)$$

where,

$$\text{sgn}(t) = \begin{cases} 1 & for \quad t > 0 \\ 0 & for \quad t = 0 \\ -1 & for \quad t < 0 \end{cases}. \tag{1.26}$$

A wavelet is considered to be causal if it vanishes for $t < 0$, and therefore

$$w(t) = w(t)h(t). \tag{1.27}$$

The finite energy concept arises in physics in the context of energy density. Mathematically, finite energy functions are L^2 functions. A function (e.g. seismic wavelet) is said to be of finite energy if it satisfies the equation:

$$\int_{-\infty}^{\infty} w^2(t)dt < \infty. \tag{1.28}$$

The inverse of the wavelet is the perfect deconvolution operator, and is described by the equation

$$\delta(t) = \int_{-\infty}^{\infty} w(\tau)d(t-\tau)d\tau = w(t) \bullet d(t), \tag{1.29}$$

where $\delta(t)$ is the Dirac delta distribution. As specified above, the deconvolution operator, (e.g., the inverse of the embedded wavelet), must also satisfy the conditions (1.27) and (1.28). It can be shown (Claerbout, 1976, Margrave, 1999) that any wavelet satisfying (1.27), (1.28), and (1.29) is necessarily minimum phase. This is often stated in another way that "a causal, stable inverse is minimum phase" (Karl, 1989).

Many distinct filters share the same amplitude spectrum (or the same autocorrelation) but have different phase spectra. The spectral factorization method finds a minimum-phase wavelet that has a given amplitude spectrum (Claerbout, 1976). The minimum-phase concept implies that the wavelet has the least amount of phase delay possible as a function of a given frequency content. Thus, the principal characteristic of

minimum-phase is that the energy is compressed towards the front. Robinson's energy delay theorem states that starting from zero to any time t, the energy summed over that time interval is greater or equal to that of any other wavelet with the same spectrum (Claerbout, 1976).

Mathematically, energy delay theorem has the form

$$E_{w_{min}}(\tau) \geq E_w(\tau), \tag{1.30}$$

where $E_{w_{min}}(t)$ is the partial energy of the minimum-phase wavelet, $E_w(t)$ the partial energy of a non-minimum-phase wavelet with the same amplitude spectrum. The partial energy of the wavelet has the form

$$E_w(\tau) = \int_0^\tau w^2(t)dt . \tag{1.31}$$

A proof of this theorem for the discrete case can by found in Claerbout (1976).

Using the Hilbert transform pair in the frequency domain, the phase of the minimum-phase causal wavelet with finite energy, can be estimated from the logarithm of the amplitude spectrum (or from the autocorrelation function) and vice versa, the logarithm amplitude spectrum can be estimated from its minimum-phase spectrum (Sheriff and Geldart, 1995)

$$\phi(\omega) = \frac{-1}{\pi} \int_{-\infty}^{\infty} \frac{\ln\left(\left|\hat{w}(\bar{\omega})\right|\right)}{\omega - \bar{\omega}} d\bar{\omega}, \tag{1.32}$$

and

$$\ln\left(\left|\hat{w}(\omega)\right|\right) = \frac{1}{\pi} \int_{-\infty}^{\infty} \frac{\phi(\bar{\omega})}{\omega - \bar{\omega}} d\bar{\omega}, \tag{1.33}$$

where ω (and $\overline{\omega}$) denotes the angular frequency, $|\hat{w}(\omega)|$ denotes the amplitude spectrum and $\phi(\omega)$ the phase spectrum of the wavelet, $w(t)$. The integrals in (1.32), and (1.33) are Hilbert transforms and are improper integrals because of the singularity in the denominator. They should be understood as limits of the Cauchy's principal values of an improper integral:

$$\int_{-\infty}^{\infty} = \lim_{\varepsilon=0}\left[\int_{-\infty}^{\omega-\varepsilon} + \int_{\omega+\varepsilon}^{\infty}\right]. \tag{1.34}$$

Thus, any given wavelet can be converted to a minimum phase equivalent, which has the same amplitude spectrum and a phase spectrum computed with the Hilbert transform described by Equation (1.32). Minimum-phase filters are often encountered in causal systems. For example, the dynamite source on land produces such a wavelet with the minimum-phase property (Robinson, 1966). Hargeaves (1992), states that the air-gun signature array is minimum phase for marine data. In these cases, the phase spectrum can be derived from the logarithm amplitude spectrum using the Hilbert transform. However, the minimum-phase assumption is controversial. For example, Ziolkowski (1991) argues that most marine sources are non-minimum phase, but admits that the dynamite source on land is minimum phase.

1.3.2 Zero-phase wavelet

The zero-phase wavelet has another important property. Berkhout (1974), demonstrated that the zero-phase wavelet is the shortest wavelet having a certain bandwidth. Any wavelet has an equivalent zero-phase wavelet with the same amplitude spectrum. The conversion from any wavelet to its zero-phase equivalent can be easily demonstrated (Ziolkowski, 1984). The Fourier transform of the wavelet is

$$\hat{w}(f) = \int_{-\infty}^{\infty} w(t) e^{-2\pi i f t} \, dt \, . \tag{1.35}$$

The amplitude and phase spectrum are computed from the Fourier spectrum as follows

$$\hat{w}(f) = |\hat{w}(f)| e^{i\phi_w (f)} . \tag{1.36}$$

Setting the phase to zero, $\hat{w}(f)$, can be converted to its zero phase correspondent. Using the inverse Fourier transform, the zero-phase (equivalent) wavelet has the form

$$w_0(t) = \int_{-\infty}^{\infty} |\hat{w}(f)| e^{2\pi i f t} \, df \, . \tag{1.37}$$

From Equation (1.36) also the negative frequency can be used in the inversion formula (1.37), resulting

$$w_0(-t) = \int_{-\infty}^{\infty} |\hat{w}(f)| e^{-2\pi i f t} \, df = \int_{-\infty}^{\infty} |\hat{w}(-f)| e^{2\pi i f t} \, df = w_0(t) \tag{1.38}$$

Equation (1.38) asserts that the zero-phase wavelet is symmetric (Ziolkowski, 1984). Subsequently, it results that the zero-phase wavelet is also noncausal, as opposed to a minimum-phase wavelet. The only signal that is both minimum- and zero-phase is the Dirac delta function which is also symmetric. The purpose of the deconvolution is to increase the resolution, and therefore to move the data toward the perfect zero-phase state.

CHAPTER 2

2. ATTENUATION CONCEPT AND THE COMPLEX TRACE ANALYSIS

The most significant definitions related to the seismic attenuation are reviewed in this chapter. The dominant idea in this chapter is the constant Q model of attenuation, which, will be used as a base to construct synthetic traces that decay in time and diminish in bandwidth as the wavefront propagates through the medium. The complex trace analysis represent useful tools that can provide quantitative measures of the seismic attenuation, such as, reflection strength, also called the amplitude of the envelope.

2.1 The attenuation concept

Attenuation refers to the amplitude decay observed in wave propagation. There are many attenuation mechanisms associated with the seismic wave propagation such as, absorption, spherical divergence, transmission losses, mode conversion, scattering effects, refractions and critical angles. Among these, absorption presents a special interest in this study because it is both, time and frequency dependent and will be described in detail, whereas for all other attenuation processes just a general definition along with a formula (if any) for compensating the undesired effect will be provided.

Spherical divergence, also known as geometric spreading, can be easily compensated for, using the total energy conservation principle. This states that the energy on the wavefront surface should be constant as the wavefront is traveling through medium. As the wavefront propagates through the medium, the surface of the wavefront (considered as a sphere in a homogenous medium) becomes greater and the wave amplitude decays with $1/R$, where R is the radius of curvature of the wavefront (Sheriff

and Geldart, 1995). It follows that to compensate for the geometric spreading it is sufficient to apply the equation

$$u(t) = u_0 \big/ R(t),$$ (2.1)

where u is the wave amplitude (u_0 for $t = 0$), and $R(t)$ can be considered as the distance traveled in the case of a constant velocity medium. As can be seen in Equation (2.1) the spherical divergence is independent of frequency (it is dependent on time only). The geometrical spreading of the wavefront is the most obvious mechanism of amplitude decay.

In the transmission losses mechanism, part of the wavefront energy is lost at layer interfaces, thereby, the more interfaces there are, the more energy is lost due to transmission losses. This effect is very difficult to explicitly define and depends on local geology in the sense that the energy loss is higher when the material grains of the medium are not elastically bonded. The transmission losses mechanism is dependent on time only and is usually compensated by the correction for the inelastic attenuation discussed below or it can be ignored.

A particular case of the transmission losses mechanism is the loss due to refractions and the associated critical angles, which are mostly present at the base of the weathering layer. As it results from the Snell's law, only a fraction from the total energy is transmitted below the weathering layer, the rest of it is reflected back (total reflection) to the surface as post-critical reflections and refractions (head waves). However, refractions are also present along deeper interfaces, depending on the incident angle of the wave and the medium impedance on both sides of the interface. Through these effects, part of the transmitted energy cannot be recorded, and therefore, constitutes an energy loss.

The mode conversion mechanism occurs since the seismic wavefield energy is converted from P to S waves at every impedance contrast (e. g. reflection point). More precisely, if the angle of incidence is greater than zero, an incident P wave will produce both, P and S reflected and transmitted waves. This phenomenon is called mode conversion. It is similar to the transmission losses but more general in the sense that it includes also the reflected waves. Mode conversion is only time dependent. Lay and Wallace (1995) explain that S waves are more attenuated than the P waves because of shear movement along grain boundaries. When only the vertical (P) component is recorded (as in conventional seismic), there is no direct information regarding the mode conversion effect and consequently, no correction can be applied.

The scattering effect is due to small heterogeneities present in geologic formations and causes the dispersion of the high frequency energy of the recorded wavefield. The scattering effect produces an apparent energy loss and sometimes can be visualized on 3D data, after migration. The scattering effect is highly dependent on sedimentation conditions and therefore, upon local geology.

Absorption is also known as inelastic attenuation. Part of the energy of the propagating wavefield is transformed into heat due to internal friction between the rock particles. The general subject of wave attenuation due to internal friction is also called intrinsic attenuation (Aki and Richards, 1980). In seismic theory, anelastic attenuation is often characterized by three essentially equivalent parameters, α, the attenation factor, δ, the logarithmic decrement, and Q, known as the quality factor.

A propagating 1-D plane wave is given as a function of the initial amplitude and phase

$$A(x,t) = A_0 e^{i(kx-\omega t)},\tag{2.2}$$

where A_0 is the reference amplitude, at $t = 0$ $x = 0$, ω is the angular frequency, and k is the wavenumber. Attenuation may be introduced by allowing the wavenumber or the frequency to be complex (Aki and Richards,1980).

When the wavenumber is complex $(k = k_r + i\alpha)$ equation (2.2) becomes

$$A(x,t) = A_0 e^{i((k_r + i\alpha)x - \omega t)} = A_0 e^{-\alpha x} e^{i(k_r - \omega t)}, \qquad (2.3)$$

where α is the attenuation parameter. It can be observed from Equation (2.3) that the amplitude decay is of exponential form.

If only the spatial dependence is considered, Johnston and Toksoz (1981), define the amplitude of an attenuated waveform as

$$A(x) = A_0 e^{-\alpha x}. \qquad (2.4)$$

Following that, α can be written as

$$\alpha = -\frac{1}{A(x)}\frac{dA(x)}{dx} = -\frac{d}{dx}\ln A(x). \qquad (2.5)$$

Considering that the wavefront passes through positions x_1 and x_2 having the amplitudes $A(x_1)$ and respectively $A(x_2)$,

$$\alpha = \frac{1}{x_2 - x_1}\ln\left[\frac{A(x_1)}{A(x_2)}\right]. \qquad (2.6)$$

The logarithmic decrement is defined as

$$\delta = \ln\left[\frac{A_1}{A_2}\right], \qquad (2.7)$$

where A_1 and A_2 are the amplitudes of two consecutive cycles of an oscillating system in free decay.

The relation between the attenuation factor and the logarithmic decrement is given by

$$\delta = \alpha\lambda = \alpha\frac{v}{f} \ ,$$

(2.8)

where λ is the wavelength, f is the frequency, and v is the velocity.

The Q factor was previously defined as the ratio between the peak stored energy over the energy lost during one cycle of deformation. O'Connell and Budiansky (1978) observed that this definition is not valid for large losses and proposed that mean stored energy be used instead of the maximum energy

$$Q = 4\pi\frac{E}{\Delta E} \ ,$$

(2.9)

where Q is the quality parameter, E is the mean stored energy (measured in Joules/second), ΔE is the energy loss during one cycle of sinusoidal deformation. The Q parameter is dimensionless (see Equation 2.9). If the energy loss is zero, the quality factor goes to infinity and this means that the medium is perfectly elastic. Using the definition from Equation (2.9), Kjartansson (1979) shows that $1/Q$ can be equivalently defined as

$$\frac{1}{Q} = \tan\beta \ ,$$

(2.10)

where, β is the phase lag of strain behind the stress.

A relation between the quality factor Q, and the attenuation coefficient is given by Hamilton (1972),

$$\frac{1}{Q} = \frac{\alpha\,v}{\pi f - \dfrac{\alpha^2 v^2}{4\pi f}} \; .$$

(2.11)

In anelastic media, the velocity, v and the quality factor Q, are functions of frequency (see Equations 2.8 and 2.11). The frequency dependence of v and Q causes the dispersion of the waveform, which tends to broaden as it propagates through the medium. Many studies have shown that the frequency dependence of Q is very weak within the bandwidth of interest (0 − 70 Hz), compared with the frequency dependence of velocity. These observations were exploited by Kjartanson (1979) in building the constant Q model of attenuation. Kjartansson developed the constant Q model of attenuation based on Equation (2.10) which states that Q is a function of the phase angle between stress and strain. In this model constant Q means that Q is independent of frequency (over the seismic bandwidth) but depends upon the medium. This model is based on two assumptions: causality and linearity. Both assumptions are valid for the range of deformations that occur in the nearly elastic media during the wave propagation. In this work, a frequency independent model of attenuation based on Kjartansson's theory has been chosen.

In Equation (2.11), the term $\alpha^2 v^2 \big/ 4\pi f$ can be dropped under the low-loss assumption, (Johnston and Toksoz, 1981) with the result

$$\frac{1}{Q} \approx \frac{\alpha\,v}{\pi f} \; .$$

(2.12)

Therefore, α becomes

$$\alpha = \frac{\pi f}{Qv} \; .$$

(2.13)

Equation (2.3) can be rewritten replacing α

$$A(x,t) = A_0 e^{-\frac{\pi f}{Qv}x} e^{i(k_r - \omega t)}. \qquad (2.14)$$

Further, replacing x/v with the traveltime, t, and ω with $2\pi f$, we get

$$A(x,t) = A_0 e^{-\frac{\pi f t}{Q}} e^{i(k_r - 2\pi f t)}. \qquad (2.15)$$

`The attenuation function is represented as an exponential decay that depends on traveltime, t, the frequency, f, and the quality factor, Q (see Equation 2.15). This time-frequency dependence of the attenuation shows that the wavelet loses the bandwidth as it travels in the media. In Equation (2.15) the third term denotes the combined phase of the propagating wave and attenuation function. It can be shown that under the causality condition (Aki and Richards, 1980) the phase spectrum of the attenuation function has the form

$$k_r = H\left(\ln\left(A_0 e^{-\frac{\pi f t}{Q}} \right) \right), \qquad (2.16)$$

where H denotes the Hilbert transform over f at constant t, used in calculating the phase spectrum of the attenuation function. The Hilbert transform implies that the attenuation is a minimum delay function (see section 1.3).

Thus, the attenuation function can be written as:

$$a(f,t) = e^{-\frac{\pi f t}{Q} - iH(\frac{\pi f t}{Q})}, \qquad (2.17)$$

which has an amplitude spectrum defined by

$$|a(f,t)| = e^{-\frac{\pi f t}{Q}}.$$
(2.18)

2.2 Complex trace analysis

The complex trace facilitates a useful separation of envelope amplitude and phase information (Taner et al., 1979). The envelope amplitude represents a basis for calculating the decay function of a trace affected by the attenuation (as in section 2.1.1) whereas the phase information is a basis for instantaneous frequency measurement.

2.2.1 The instantaneous frequency and the amplitude attribute

The instantaneous frequency and the envelope attributes can be used to examine the nonstationary character of the data. In order to calculate the instantaneous frequency and the envelope attributes, the analytic signal should be derived from a real signal.

A complex signal is defined by

$$s_{complex}(t) = s(t) + i\, s^*(t) = A(t)e^{i\phi(t)},$$
(2.19)

where $s(t)$ is the real part of signal and $s^*(t)$ represents the imaginary part of the signal.
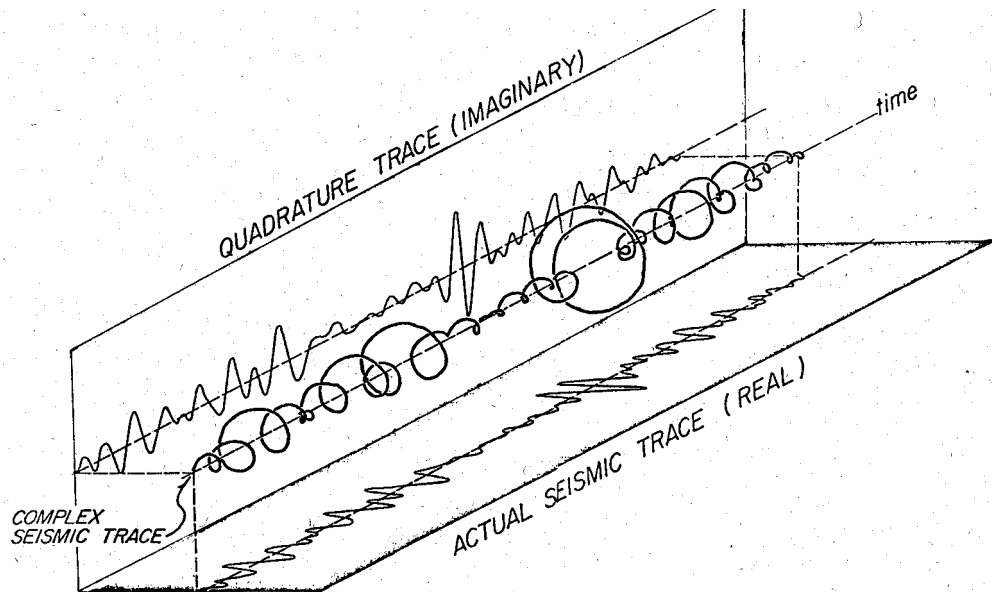
Figure 2.1.: 3D representation of a complex seismic trace (from an East Texas survey, after Taner et al., 1979)

In the Figure 2.1, both the real and quadrature signals are identical except phase shifted by 90^0. The imaginary part can be derived in two ways: by the quadrature method (Taner et al., 1979) and analytic signal method (Cohen, 1995). The conclusion of both procedures is that the complex signal has an amplitude spectrum twice as large as that of the real signal for positive frequencies and zero for the negative frequencies.

The quadrature method employs the use of the Fourier transform in calculating the conjugate (also called imaginary) component of a complex trace (Taner et al., 1979). Assuming that $s(t)$ is the real part of a complex trace and $-\infty < t < \infty$, the complex trace can be computed by zeroing the amplitudes for negative frequencies and doubling the amplitudes for positive frequencies in the Fourier domain (Taner et al., 1979),. Thus, if the inverse Fourier transform of a real trace is

$$s(t) = \int_{-\infty}^{\infty} \hat{s}(\omega) e^{i\omega t} d\omega \qquad (2.20)$$

this is equivalent to

$$s(t) = \int\limits_0^\infty 2\,|\,\hat{s}(\omega)\,|\cos(\omega t + \phi(\omega))d\omega\,, \tag{2.21}$$

where $\phi(\omega)$ represent the phase spectrum of the real trace for positive frequencies, $\omega > 0$. Then, the quadrature trace is

$$s^*(t) = \int\limits_0^\infty 2\,|\,\hat{s}(\omega)\,|\cos(\omega t + \phi(\omega) + \frac{\pi}{2})d\omega = \int\limits_0^\infty 2\,|\,\hat{s}(\omega)\,|\sin(\omega t + \phi(\omega))d\omega\,, \tag{2.22}$$

and the complex trace is

$$s_{complex}(t) = \int\limits_0^\infty 2\,|\,\hat{s}(\omega)\,|\,e^{i(\omega t + \phi(\omega))}d\omega\,. \tag{2.23}$$

Alternately the complex trace can be computed using the Hilbert transform, that is, the imaginary part is related to the real part by the Hilbert transform over time, denoted by H (Taner et al, 1979)

$$s^*(\tau) = H[s(t)] = \frac{1}{\pi}\int_{-\infty}^\infty s(t)\frac{1}{t-\tau}dt\,. \tag{2.24}$$

Computationally, the Hilbert transform can be accomplished by a convolution in time domain between the trace and the quadrature filter (the Hilbert kernel) (Claerbout, 1980). This yields the quadrature signal,

$$s^*(t) = \frac{1}{\pi}\sum_{-\infty}^\infty s(t - n\Delta t)\frac{1 - e^{i\pi n}}{n} = \frac{2}{\pi}\sum_{-\infty}^\infty s(t - n\Delta t)\frac{\sin^2\left(\dfrac{\pi n}{2}\right)}{n}\,. \tag{2.25}$$

Thus, the Hilbert kernel is of the form (see Figure 2.2):

$$q_n = \begin{cases} 0 \ for \ n \ even \\ -\dfrac{2}{\pi \, n} \ for \ n \ odd \end{cases}.$$
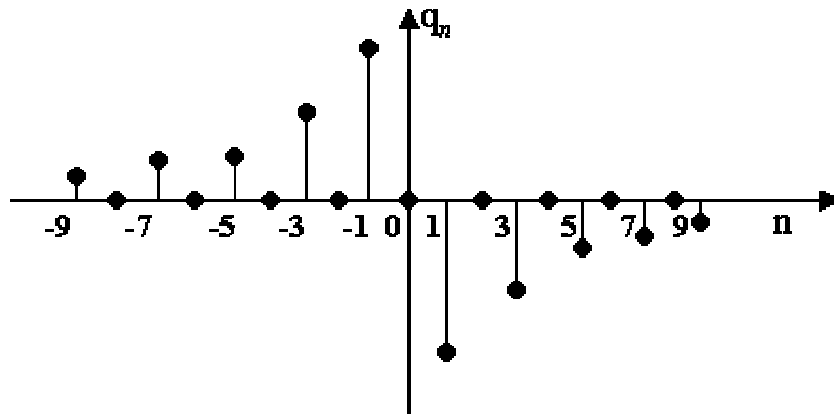
Figure 2.2.: Quadrature filter, truncated to nineteen points.

The Hilbert kernel in time domain is characterized by the following properties (Claerbout, 1976):

- does not vanish for negative samples
- has a singularity at $n = 0$
- it needs future samples for the present output (it is nonrealizable).

In practice, because all the samples are known it can be applied, usually in a modified truncated version (Taner, et al. 1979)

The time dependent amplitude of the complex signal (also called envelope) is given by

$$A_c(t) = \sqrt{s^2(t) + s^{*2}(t)}, \qquad (2.26)$$

and the time dependent phase by

$$\phi(t) = \tan^{-1}(\frac{s*(t)}{s(t)}) \tag{2.27}$$

which is time domain equivalent of relation (1.22) in section 1.3.

The envelope of the trace (as in Equation 2.26) is a useful tool to measure the decay in time of the embedded wavelet, assuming that the envelope of the plain reflectivity is stationary. The envelope of the trace is used in designing the gain functions used in the time variant spectral whitening (TVSW) method (explained in section 4.2.2.).

The real part of the signal (in time domain) can be expressed by the formula:

$$s(t)=A_c(t)\cos(\phi(t)), \tag{2.28}$$

and the imaginary part by

$$s*(t)= A_c(t)\sin(\phi(t)). \tag{2.29}$$

$A_c(t)$ is also called the reflection strength, and $\phi(t)$ the instantaneous phase (Bracewell, 1965).

For the analytic signal, the rate of change of the time-dependent phase gives a time-dependent frequency, named instantaneous frequency ($\omega_i(t)$).

$$\frac{d(\phi(t))}{dt} = \omega_i(t) = 2\pi f_i(t), \tag{2.30}$$

The envelope is a physically meaningful tool however, careful use of the instantaneous frequency attribute is recommended in applications. Cohen (1995) has encountered several paradoxes related to the instantaneous frequency. Some of them are: 1) the instantaneous frequency can be negative although the spectrum of the analytic signal is zero for negative frequencies; 2) the instantaneous frequency may be continuous

and range over infinite values for a spectrum consisting of only a few sharp frequencies; 3) the instantaneous frequency at a time t is of nonlocal nature since in calculating the analytic signal we have to know the signal for all time.

CHAPTER 3

3. GABOR DECONVOLUTION

Two types of nonstationary deconvolution will be presented in this section. First, an operator based nonstationary deconvolution, which is chronologically, a predecessor of the Gabor deconvolution, will be reviewed. Secondly, the principles of Gabor deconvolution, which is transform based, will be presented in detail, along with the new smoothing technique implemented in this work.

In this section, the nonstationarity of the signal is considered in the deconvolution process. As shown in section 1.4, the anelastic attenuation is time and frequency dependent. A successful attempt to compensate for the undesired effect of attenuation employs methods based on nonstationary linear filtering theory (Margrave, 1998). For this reason a basic idea of the nonstationary convolutional model will also be reviewed.

3.1 Mixed domain nonstationary deconvolution, operator based

The mixed-domain (the term "mixed" refers to simultaneous time and frequency dependence and will be defined later in this section) nonstationary deconvolution, operator based, is referred to as the nonstationary deconvolution (NSD), by Schoepp (1998). Nonstationary deconvolution compensates for the earth's attenuation effect acting on the source waveform. Anelastic attenuation is the main mechanism that causes frequency-dependent amplitude decay of the propagating waveform (See section 2.1 - The attenuation concept - for definition and a brief review of similar processes). Based on the nonstationary filter theory (Margrave, 1998), mixed-domain nonstationary deconvolution uses the time-frequency analyses to design the deconvolution operator

(Schoepp, 1998). In this section, a short review of the nonstationary filter theory will be provided prior to explaining the mixed-domain nonstationary deconvolution method.

Nonstationary filtering theory can be explained as an extension of the stationary convolution described in section 1.2.1. Alternately, stationary convolution can be viewed as a particular case of nonstationary filtering theory. Starting from the stationary case, if the filter is altered in time (due to the attenuation mechanism for example), the time dependence should be explicitly specified in the convolution integral

$$s(t) = \int_{-\infty}^{\infty} w(t-\tau, \tau) r(\tau) d\tau, \qquad (3.1)$$

where $w(t-\tau, \tau)$, shows the filter dependence on both input and output times, τ and t, and $r(t)$ represents the reflectivity series, as explained for Equation (1.1) and can be understood as the input signal, $s(t)$ is the output trace which can be viewed as the filtered signal. Computationally, Equation (3.1) can be represented by a multiplication between a nonstationary impulse response function (e.g. the attenuated wavelet) with a time series vector representing the reflectivity series. In Figure 3.1, an arbitrary wavelet (from the matrix in the middle) chosen at some time $t = v$ measured on the vertical from the top of the matrix (considered as the input time), represent the time-shifted impulse response $w(u-v, v)$ and is defined as a function of both, input and output time (denoted by u).
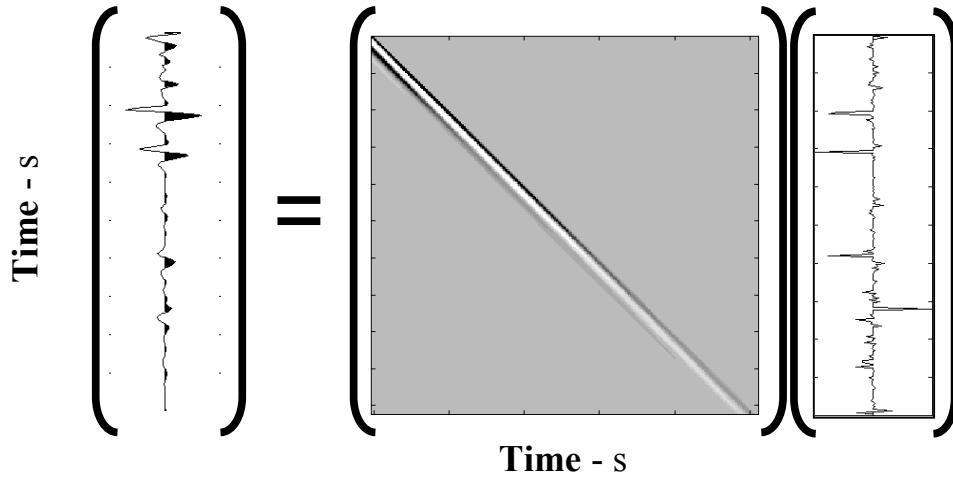
Figure 3.1.: Trace representation in time domain (Equation 2.1). The trace (column vector, on the left) is the result of the nonstationary convolution (matrix multiplication) between an attenuated minimum-phase seismic wavelet (represented in the square matrix in the middle) and the reflectivity series (the column vector, on the right). The nonstationary impulse response function was obtained by multiplying the stationary waveform of Figure 1.1 (the Toeplitz matrix) by a minimum-phase impulse response of a constant Q medium, (after Margrave, 1998).

Another version of the nonstationary filtering concept is called nonstationary combination and the filter dependence is linked to the output time

$$\tilde{s}(t) = \int_{-\infty}^{\infty} w(t-\tau,t) r(\tau) d\tau , \qquad (3.2)$$

where $w(t-\tau,t)$, shows the filter dependence on the output time, t , and $\tilde{s}(t)$ is the result of the nonstationary combination in the time domain. The relation between the nonstationary convolution and the nonstationary combination is of reciprocity, in the sense that in the Fourier domain, the nonstationary convolution becomes a nonstationary combination and vice versa, the nonstationary combination becomes a nonstationary convolution in frequency domain. A detailed mathematical demonstration can be found in Margrave (1998), here just the final results are shown. Thus, in the frequency domain, the nonstationary convolution becomes a nonstationary combination

$$\widetilde{s}(f) = \int_{-\infty}^{\infty} \hat{w}(f - F, f) \hat{r}(F) dF , \qquad (3.3)$$

and the nonstationary combination becomes a nonstationary convolution,

$$\hat{s}(f) = \int_{-\infty}^{\infty} \hat{w}(f - F, F) \ \hat{r} \ (F) \ dF , \qquad (3.4)$$

where, in Equations (3.3) and (3.4), $\hat{s}(f)$ represent the Fourier transform of the $s(t)$, $\hat{r}(f)$ is the Fourier transform of the $r(t)$, F is the input frequency and f is the output frequency. The dependence of the input filter in the nonstationary convolution or combination on either input or output frequency is similar to the time domain case. In Equation (3.3), $\hat{w}(f, F)$ is called the frequency domain connection function and is the 2D Fourier transform of the filter $w(t, \tau)$

$$\hat{w}(f, F) = \int_{-\infty}^{\infty} \int_{-\infty}^{\infty} w(t, \tau) \ e^{-2\pi i f t} e^{-2\pi F \tau t} dt d\tau . \qquad (3.5)$$

The mixed domain expression of the nonstationary convolution (as in Equation 3.1), is

$$\hat{s}(f) = \int_{-\infty}^{\infty} \Omega(f, \tau) r(\tau) e^{-2\pi i f \tau} d\tau , \qquad (3.6)$$

where

$$\Omega(f, \tau) = \int_{-\infty}^{\infty} w(t, \tau) e^{-2\pi i f t} dt , \qquad (3.7)$$

is called the nonstationary transfer function defined in the mixed time-frequency domain which is equivalent to a nonstationary wavelet (e.g. nonstationary impulse response) defined in the time domain.

The output of the mixed-domain convolution belongs to the frequency domain whereas the nonstationary transfer function is defined in the mixed time-frequency

domain. There is also a mixed domain formulation for the nonstationary combination (as in Equation 3.2) with the output in the time domain, (see Margrave, 1998 for a mathematical description).

For the deconvolution problem in the nonstationary case, similar to the stationary deconvolution case, an inverse filter should be designed from the data to recover the reflectivity series. As in the stationary case, in the Fourier domain deconvolution, the inverse filter can be obtained by smoothing the data in the mixed, time-frequency domain, using the nonstationary convolution approach. For example, the smoothed version of the amplitude spectrum (of an attenuated trace) in the time-frequency domain is an estimate of the transfer function described in Equation (3.7). Based on similar assumptions related to the statistical properties of the reflectivity (assuming a white reflectivity spectrum, in the time-frequency domain) the smoothed version of the amplitude spectrum can be inverted to form the deconvolution operator. The nonstationary transfer function contains two components, the source signature and the character of the attenuation function. The deconvolution operator can be designed minimum- or zero-phase. The relation between the deconvolution operator, $D(t,f)$ and the forward nonstationary transfer function as described in Equation (3.7) is

$$D(f,t)\Omega(f,t)=1, \hspace{3cm} (3.8)$$
$$\text{(Schoepp, 1998).}$$

An estimate of the reflectivity is obtained in the frequency domain applying the deconvolution operator to the trace in the mixed time-frequency domain

$$\hat{r}_{est}(f) = \int_{-\infty}^{\infty} D(f,\tau)\ s(\tau)\ e^{-2\pi i f \tau} d\tau , \hspace{2cm} (3.9)$$

where $s(\tau)$ is the attenuated trace in time domain which should be understood as the inverse Fourier transform of the nonstationary convolution (in the mixed domain)

between the nonstationary transfer function (the attenuated impulse response) and the reflectivity series (as in Equation 3.6)

$$s(\tau) = \int_{-\infty}^{\infty} s(f) e^{2\pi i f \tau} df = \int_{-\infty}^{\infty} \int_{-\infty}^{\infty} \Omega(f, \tau') r(\tau') e^{2\pi f (\tau - \tau')} d\tau' df \ . \qquad (3.10)$$

The last step of the mixed domain nonstationary deconvolution is an inverse Fourier transform applied in order to obtain the reflectivity estimate in time domain.

There are several limitations related to this method of deconvolution. The main drawbacks of the method come from the fact that the smoothing techniques act not only on the reflectivity character (ideal case) but also on the source signature, multiples (if present), and attenuation function. In order to avoid a biased result (affected by a systematic error), the multiples should be removed and an estimate of Q is required a priori. In addition the results of the mixed time domain deconvolution, (operator based) are limited by numerical precision (Schoepp, 1998).

3.2 Gabor domain nonstationary deconvolution, transform based

In this section a particular case of forward and inverse Gabor transform is presented. First, the continuous case will be shown followed by a discrete implementation of the theory. This particular Gabor transform uses a set of normalized, translated Gaussians in slicing the seismic signal (Margrave and Lamoureux, 2001). Based on this Gabor transform, a robust algorithm of the time-variant deconvolution will be presented.

3.2.1 Gabor transform

The classical Fourier spectrum of a signal that belongs to L^2 (functions of finite energy, or square integrable functions, presented in section 1.3 − Equation 1.28) shows the frequencies occurring in the signal but it does not contain any information on the time

of occurrence. In order to recover the time information, the Gabor transform (also called windowed Fourier transform or short time Fourier transform, STFT) is used. The essence of the windowed Fourier transform is that the signal is masked by a moving window g(t)

$$\hat{s}(\tau, f) = \int_{-\infty}^{\infty} s(t)\, g(t - \tau)\, e^{-2\pi ift}\, dt \quad, \tag{3.11}$$

where $\hat{s}(\tau, f)$ represent the Gabor spectrum of a signal, $s(t)$.

The windowed Fourier transform is therefore a regular inner product, like the classical Fourier transform. Generally, an inner product assigns a complex number to two signals. The physical interpretation of the inner product is that it represents a measure of the similarity between the signal $s(t)$ and an elementary function, $g(t - \tau)\, e^{-2\pi ift}$.

The window function $g(t - \tau)$, named the analysis function, is centered at time τ and is usually a real, even function. Multiplying the signal by the window function, the result is a modified signal that is a function of two times, the fixed time, τ, and the running time t.

The inner product can be written with the help of an operator, υ_g as follows,

$$\hat{s}(\tau, f) = \upsilon_g\, s(\tau, f) = \left\langle s, M_f T_\tau g \right\rangle. \tag{3.12}$$

The operator υ_g, is composed by two sub-operators, a translation operator and a modulation operator,

$$T_t\, g(\tau) = g(\tau - t), \tag{3.13}$$

$$M_f g(\tau) = e^{-2\pi i f\tau} g(\tau), \tag{3.14}$$

where, T represent the translation operator, and M the modulation operator.

The inverse transform, can be written in the same way as the forward transform with the help of a synthesis function, $\gamma(t)$, as follows,

$$s(t) = \int\limits_{-\infty}^{\infty}\int\limits_{-\infty}^{\infty} \upsilon_g \hat{s}(t,f)\gamma(t-\tau)e^{2\pi i f\tau}d\tau df. \tag{3.15}$$

In particular, g and γ should satisfy the condition (Mertins, 1999)

$$\int\limits_{-\infty}^{\infty} g(u)\gamma(u)du = 1. \tag{3.16}$$

This condition can be demonstrated replacing the term $\upsilon_g s(t,f)$ in the reconstruction relation by substituting Equation (3.11) into (3.15)

$$s(t) = \int\limits_{-\infty}^{\infty}\int\limits_{-\infty}^{\infty}\int\limits_{-\infty}^{\infty} s(\tau')g(\tau'-\tau)e^{-2\pi i f\tau'}d\tau'\,\gamma(t-\tau)e^{2\pi i ft}d\tau df, \tag{3.17}$$

interchanging the order of integration

$$s(t) = \int\limits_{-\infty}^{\infty}\int\limits_{-\infty}^{\infty}[\int\limits_{-\infty}^{\infty} g(\tau'-\tau)\gamma(t-\tau)d\tau]s(\tau')e^{2\pi i f(t-\tau')}d\tau'df, \tag{3.18}$$

and solving the integral depending on f

$$s(t) = \int\limits_{-\infty}^{\infty}[\int\limits_{-\infty}^{\infty} g(\tau'-\tau)\gamma(t-\tau)d\tau]s(\tau')\delta(t-\tau')d\tau', \tag{3.19}$$

recognizing that

$$\int_{-\infty}^{\infty} e^{2\pi i f(t-\tau')} df = \delta(t-\tau').$$
(3.20)

Changing the variable $u = \tau' - \tau$, in the inner integral and using the sifting property of the δ distribution, the identity is proved

$$\int_{-\infty}^{\infty}\int_{-\infty}^{\infty} g(u)\gamma(t-\tau'+u)du]\,\delta(t-\tau')s(\tau')d\tau' = s(t)\int_{-\infty}^{\infty} g(u)\gamma(\tau'-\tau'+u)du = s(t)\int_{-\infty}^{\infty} g(u)\gamma(u)du = s(t).$$

(3.21)

For the practical application of this theory, the discrete case of a particular case of the Gabor transform developed by Margrave and Lamouroux (2001) will be described.

In the discrete case, the window chosen to slice the signal is a normalized Gaussian (see Figure 3.2) of the form

$$g_k(t) = \frac{X}{\sqrt{\pi}} e^{-\alpha^2 (t-k\Delta)^2}$$
(3.22)

where $1/\alpha$ - represents the width of the window and Δ represents the time increment between two consecutives windows, and X is a normalization parameter which will be determined subsequently.

Time - s
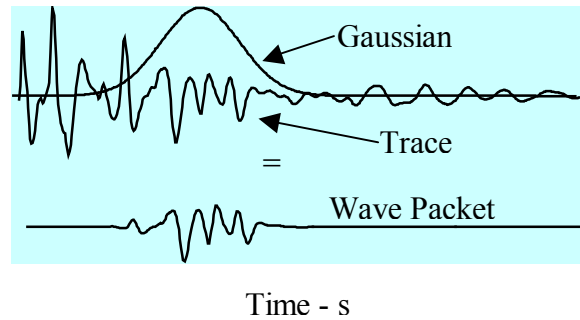
Figure 3.2.: The result of the multiplication between a seismic signal and a Gaussian (top) yields a sliced signal (bottom) also called wave packet.

The normalization constant (X), is computed in such a way that the overlapped windows sum to unity for every location in time. The set of the normalized Gaussian windows (shown in Figure 3.3) form a partition of unity (ideal case) (Margrave and Lamoureux, 2001), given by

$$\sum_k g_k(t) = 1 \qquad (3.23)$$
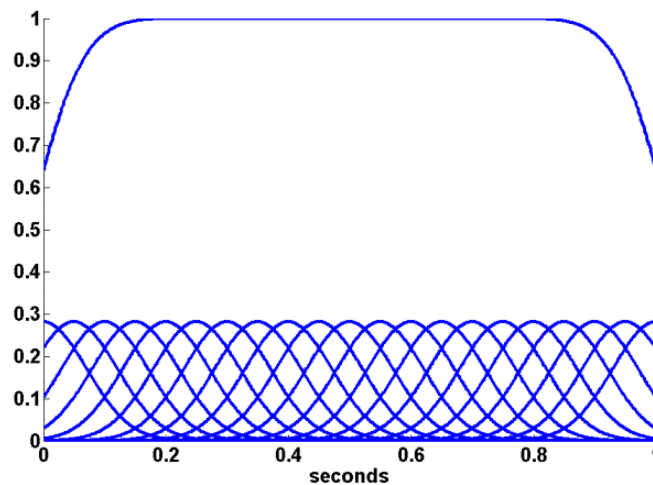
Figure 3.3.: A set of the normalized Gaussians form an approximate partition of unity (the summation curve at the top, after Margrave and Lamoureux, 2001).

The normalization step is performed to simplify the inverse Gabor transform, which in this case becomes an ordinary inverse Fourier transform after summing the

Gabor spectrum over the frequency axis (this observation holds also for the continuous case (Equation 3.15) and is demonstrated in the subsequent relations for the discrete case).

A signal *s(t)* can be written as a sum of windowed signals

$$s(t) = s(t)\sum_k g_k(t) = \sum_k s_k(t),$$ (3.24)

where s_k should be understood as the product between the signal, *s* and the window centered at position *k*, denoted by g_k.

Denoting the forward Fourier transform by $\Im$, and applying the Fourier transform to Equation (3.24) results

$$\Im[s(f)] = \hat{s}(f) = \sum_k \Im(s_k)(f) = \sum_k \hat{s}_k(f),$$ (3.25)

and the inverse windowed Fourier transform becomes an ordinary inverse Fourier transform of the windowed spectrum which is discrete in time and continuous in frequency

$$s(t) = \Im^{-1}[\hat{s}(f)] = \Im^{-1}[\sum_k \hat{s}_k(f)].$$ (3.26)

Equation (3.23) can be written as the convolution of the Gaussian with a comb function of the form

$$c(t) = \sum_k \delta(t - k\Delta),$$ (3.27)

where δ is the Dirac distribution, *k*, is the time sample of the Gaussian's center, and Δ is the time increment between two consecutive Gaussians.

The result of the convolution represents a new function, $h(t)$

$$(c \bullet g)(t) = h(t).$$ (3.28)

It is desirable to choose X in Equation (3.22) such that $h(t) = 1$ for all t. It is more convenient to calculate $h(t)$ in Fourier domain (using the property of the convolution theorem). Thus, in the frequency domain, the convolution of the Gaussian and the comb functions becomes a product

$$\hat{h}(f) = \hat{g}(f)\hat{c}(f).$$ (3.29)

The Fourier transform of the Gaussian and the comb function are (Brigham, 1974):

$$\hat{g}(f) = X e^{\frac{-\pi^2 f^2}{\alpha^2}},$$ (3.30)

and

$$\hat{c}(f) = \frac{1}{\Delta} \sum_n \delta(f - \frac{n}{\Delta}).$$ (3.31)

Returning to time domain, the inverse Fourier transform of the $\hat{h}(f)$ yields $h(t)$

$$h(t) = \Im^{-1}[h(f)] = \Im^{-1}[X e^{\frac{-\pi f^2}{\alpha^2}} \frac{1}{\Delta} \sum_n \delta(f - \frac{n}{\Delta})] = \frac{1}{\Delta} X \sum_n \Im^{-1}[e^{\frac{-\pi^2 f^2}{\alpha^2}} \delta(f - \frac{n}{\Delta})].$$ (3.32)

Writing the inverse Fourier transform explicitly, $h(t)$ has the form

$$h(t) = \frac{1}{\Delta} X \sum_n \int_{-\infty}^{\infty} e^{\frac{-\pi^2 f^2}{\alpha^2}} \delta(f - \frac{n}{\Delta}) e^{2\pi i f t} df = \frac{1}{\Delta} X \sum_n e^{\frac{-\pi^2}{\alpha^2}\left(\frac{n}{\Delta}\right)^2 + 2\pi i \frac{n}{\Delta} t}.$$ (3.33)

In the relation (3.33), the largest term occurs for n = 0, and then the next largest terms are the terms for n= +/- 1, +/- 2, and so on. Thus, the series (3.33) can be written as:

$$h(t) = \frac{X}{\Delta} + \frac{Xe^{\frac{-\pi^2}{\alpha^2}\frac{1}{\Delta^2}+\frac{2\pi it}{\Delta}}}{\Delta} + \frac{Xe^{\frac{-\pi^2}{\alpha^2}\frac{1}{\Delta^2}-\frac{2\pi it}{\Delta}}}{\Delta} + \cdots = \frac{X}{\Delta} + \frac{Xe^{\frac{-\pi}{\alpha^2}\frac{1}{\Delta^2}}}{\Delta}\left(e^{\frac{2\pi it}{\Delta}} + e^{\frac{-2\pi it}{\Delta}}\right) + \cdots =$$

$$= \frac{X}{\Delta} + \frac{X}{\Delta}e^{-\left(\frac{\pi}{\alpha\Delta}\right)^2}\cos\left(2\pi\frac{t}{\Delta}\right) + \cdots = \frac{X}{\Delta}\left(1 + 2e^{-\left(\frac{\pi}{\alpha\Delta}\right)}\cos\left(2\pi\frac{t}{\Delta}\right) + \cdots\right), \quad (3.34)$$

where the first term is defined for n = 0, the second for n = 1, the third for n = - 1, and the remaining terms are implied. In the current context only the first term is desired whereas the reminder (the second, third, and so on…) estimate a residual or "error". In the continuous case when $\Delta \to 0$, the error $\to 0$. This observation leads to the conclusion that $h(t) = 1$, if X in relation (3.22) takes the value of Δ, $(X = \Delta)$, which is exactly the increment between two consecutive windows.

Denoting $\alpha = \dfrac{1}{T}$, the Gaussian will have the form

$$g_k(t) = \frac{\Delta}{\sqrt{\pi}T}e^{\frac{-(t-k\Delta)^2}{T^2}}. \quad (3.35)$$

3.2.2 Gabor deconvolution

The Gabor deconvolution is presented in relation with the nonstationary filtering theory presented in section 3.1. The nonstationary convolutional model is that described by Equation (3.1). Taking the Gabor transform of such a trace (the attenuation model is based on the constant Q theory developed by Kjartanson, 1979, see section 2.1 for details) and considering just the absolute values of the Gabor spectrum denoted by the modulus symbol, we get

$$| \hat{s}(\tau, f) | \cong \left| \hat{w}(f) \right| | a(\tau, f) | | \hat{r}(\tau, f) |, \qquad (3.36)$$

where $\left| \hat{s}(\tau, f) \right|$ is the magnitude of the Gabor spectrum of a trace, $\left| \hat{w}(f) \right|$ - the magnitude of the Fourier spectrum of the source signature (stationary), $\left| a(\tau, f) \right|$ is the magnitude of the attenuation function, and $\left| \hat{r}(\tau, f) \right|$ is the magnitude of the Gabor spectrum of the reflectivity.

The relation between the attenuation function a in Equation (3.36) and the quality factor Q is (see section 2.1 for a description of the quality factor)

$$| a(\tau, f) | = e^{\frac{-\pi f \tau}{Q}}. \qquad (3.37)$$

In order to estimate the reflectivity from the trace, first, we estimate the source signature and the attenuation function. Assuming that the reflectivity series has the statistical properties of random white noise such that $\left| \overline{\hat{r}(\tau, f)} \right| = 1$ (where the overbar denotes smoothing), a smoothed version of the magnitude Gabor spectrum of the seismic signal will give an estimate of the product of the embedded wavelet and the attenuation

function. This is similar to the frequency domain deconvolution explained in section 1.2.3, and also, to the NSD operator based described in section 3.1. Two techniques of smoothing have been tested in Gabor deconvolution. First the boxcar smoother will be discussed and second, hyperbolic smoothing will be presented.

3.2.2.a The boxcar smoother

Smoothing the Gabor magnitude spectrum of the seismic trace through a 2D convolution with a 2D boxcar tends to suppress the reflectivity information and will therefore, estimate the source signature of the spectrum times the attenuation function (this method was previously implemented by Schoepp and Margrave, 1998, in the mixed domain deconvolution case, and Margrave and Lamoureux, 2001, in the Gabor deconvolution case). Using the boxcar smoother, the attenuation and the source signature are estimated as a single entity and the size of the boxcar, in time and frequency, significantly affects the result. The frequency dimension of the smoothing window determines the number of the points to be smoothed along the frequency axis and controls the temporal size of the assumed source signature estimate. Shorter source signatures have smoother spectra. The time dimension of the smoothing operator determines the number of spectral points to be smoothed in time. This parameter controls the nonstationarity of the deconvolution. The greater this value, the more stationary the deconvolution becomes. Assuming that $r(t,f)$ is a rapidly varying function with a white spectrum, while $w(f)$ and $a(t,f)$ are slowly varying functions, smoothing the magnitude Gabor spectrum will yield a combined estimate of the source signature and the attenuation function

$$\left| \overline{s(\tau, f)} \right| \cong \{ \left| \hat{w}(f) \right| \left| a(\tau, f) \right| \}_{est} \, .$$ (3.38)

Thus, the magnitude spectrum of the deconvolution operator will have the form

$$|D(\tau,f)| = \left(\{ \left| \hat{w}(f) \right| \left| a(\tau,f) \right| \}_{est} + \varepsilon A_{\max} \right)^{-1}, \tag{3.39}$$

where ε is a small real number and A_{max} is the maximum value of the smoothed Gabor spectrum (Equation 3.38) introduced to avoid any division by zero.

The phase information is calculated from the amplitude spectrum of the deconvolution operator with the Hilbert transform, assuming the minimum-phase condition, thus the deconvolution operator becomes

$$D(\tau,f) = \frac{e^{-iH\left(\ln |D(\tau,f)| \right)}}{\left| \hat{w}(f) \right| \left| a(\tau,f) \right| + \varepsilon A_{\max}}, \tag{3.40}$$

and the deconvolution equation in the Gabor domain has the form

$$\hat{r}(\tau,f)_{est} = D(\tau,f)\,\hat{s}(\tau,f). \tag{3.41}$$

This estimate of the Gabor transform of the reflectivity can be inverse transformed to give the reflectivity in the time domain.

3.2.2.b The hyperbolic smoother

This method is a novel approach developed in this work for the first time. The attenuation function described in Equation (3.37) is constant for $\tau f = constant$, that is, along a hyperbola in the time–frequency plane. Therefore, an average of Equation (3.36) along such a hyperbolic contour will estimate the magnitude of the attenuation function provided that the reflectivity and source signature terms average to unity along the contours. Without further justification, it is assumed that this is nearly the case.

Hyperbolic smoothing is achieved by calculating the average of the Gabor magnitude spectrum on constant time-frequency hyperbolae contours. Let $\sigma = \tau f$ be a hyperbolic contour of $\tau f = constant$. Then, let $\tau(f) = \sigma / f$, and the hyperbolically smoothed Gabor spectrum is given by

$$\left| \overline{\hat{s}(\tau, f)} \right|_{Hyp} = \frac{\int \left| \hat{s}(\tau(f), f) \right| df}{\int \tau(f) df} \equiv \left| a(\tau, f) \right|_{est}. \tag{3.42}$$

In equation (3.42), $\left| a(\tau, f) \right|_{est}$ denotes the hyperbolically smoothed spectrum, an estimate of the attenuation surface. Smoothing the magnitude spectrum on hyperbolic contours means that, along every hyperbola on the time-frequency plane, an average value is computed.

Dividing the Gabor magnitude spectrum by the hyperbolically smoothed spectrum, the attenuation information is removed and the source signature can now be estimated. Let $\mu(\tau, f)$ denote this non-attenuated spectrum,

$$\mu(\tau, f) = \frac{\left| \hat{s}(\tau, f) \right|}{\left| a(\tau, f) \right|_{est}}. \tag{3.43}$$

The (stationary) source signature can be estimated after averaging $\mu(\tau, f)$ over time, as

$$\left| \hat{w}(f) \right|_{est} = \frac{\int_{0}^{\tau_{max}} \mu(\tau, f) d\tau}{\tau_{max}}. \tag{3.44}$$

Smoothing this result by convolution with a frequency boxcar will improve the source signature estimate.

Next, the deconvolution operator is derived by multiplying the source signature (Equation 3.44) at all times with the hyperbolically smoothed spectrum, the estimated attenuation described by Equation (3.42), and inverting the result

$$
\left| D(\tau, f) \right| = \left(\left| \hat{w}(f) \right|_{est} \left| a(\tau, f) \right|_{est} + \varepsilon A_{max} \right)^{-1},
\tag{3.45}
$$

where εA_{max} is the same as in Equation (3.39).

The minimum-phase information and the estimated reflectivity can be calculated in the same way as in the boxcar smoother case (Equations 3.40 and 3.41).

3.3 Two methods of spectral estimation

A detailed discussion of the Burg spectral estimation is given by Robinson and Treitel (1980). In this section just a brief description of the spectrum is presented, along with some useful comments regarding this method.

The method of spectral estimation used in calculating the Gabor magnitude spectrum can be a straightforward discrete Fourier transform (DFT) or the Burg spectrum of the windowed signal. A synthetic trace is represented in time domain in Figure 3.4. The differences between the two methods of spectral estimation can be observed comparing Figure 3.5 (Gabor/ Burg magnitude spectrum) with Figure 3.6 (Gabor / DFT magnitude spectrum).
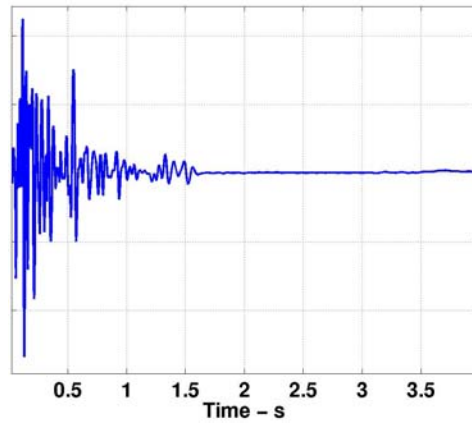
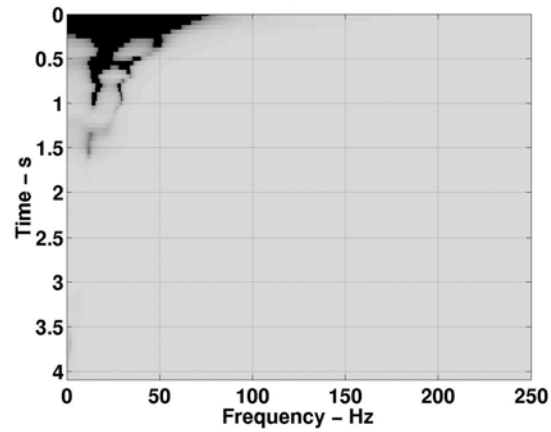Figure 3.4.: A synthetic attenuated (*Q*=25) trace in time domain.

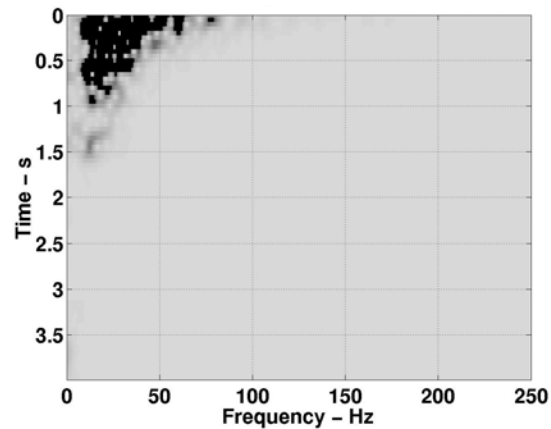Figure 3.5.: Gabor-MEM magnitude spectrum of the trace in Figure 3.4.

Figure 3.6.: Gabor-DFT magnitude spectrum of the trace in Figure 3.4.

The Burg method is also called the maximum entropy method (MEM), where entropy is a measure of disorder or unpredictability. The Burg method of calculating the spectrum produces a power spectral estimate corresponding to the most random and least predictable time series (Robinson and Treitel, 1980). In comparison to the straightforward DFT method, the Burg spectrum does not require a "window" geometry (Margrave, 1999). Another important characteristic of the Burg method is the smoothness already achieved when calculating the spectrum (see Figure 3.5 for the Burg estimate of the trace calculated with a prediction error filter (PEF) of order 5). This smoothness is controlled by the PEF length. Smoother filters yield smoother spectra estimates. Thus, the Burg method uses a PEF to achieve the predictability of a signal beyond its definition time, or off the ends. In the discrete Fourier transform case the frequency resolution of the data is limited by the assumption that the data contains all of its energy within an interval ΔT, which implies that the energy of the signal is zero outside this interval (Claerbout, 1976). In the frequency domain this statement is equivalent to saying that the energy of the signal is contained in a bandwidth of $\Delta f \geq 1/\Delta T$. In conformity to the Heisenberg's uncertainty principle, the frequency resolution is in the best case, equal to $1/\Delta T$. Using the Burg method of spectral estimation, theoretically, a finer frequency resolution can be achieved when the signal is predicted beyond the interval Δt (i.e., $\Delta f < 1/\Delta T$).

The Burg spectral estimate of a signal has the form

$$\hat{s}_B(\omega) = \frac{\sigma_m^2}{|P_m(\omega)|^2}, \tag{3.46}$$

where $\hat{s}_B(\omega)$, represent the MEM spectral estimate, σ_m^2 is the prediction error variance for an m + 1-length filter, and P_m is the PEF which has the coefficients determined directly from the data (Robinson and Treitel, 1980). In Equation (3.46), the spectrum of the input signal is represented indirectly by the inverse of the spectrum of the PEF.

According to Claerbout (1978), narrow spectral peaks are more easily represented by a denominator than by a numerator and this implies that the Burg method of spectral estimation provides superior frequency resolution in cases where such peaks occur.

3.4 Application on synthetic data of the Gabor deconvolution

This section is focused especially on the results. Even though the Gabor deconvolution parameters were previously tested prior to select the best of them, to avoid repeatability, they are explained and exemplified in detail in section 3.5 (Application on real data of the Gabor deconvolution). In summary, the parameters used in this section were: 1) the width of the Gaussian window was 0.2 ms; 2) the increment between two consecutive analysis windows was 0.05 ms; 3a) the frequency dimension of the boxcar smoother is 10 Hz; 3b) the corridor width of the hyperbolic smoother is 4Hz-sec ; 4a) the time dimension of the boxcar smoother was 0.5 seconds; 5) the phase of the deconvolution operator was minimum phase in both cases; 6) in the Burg spectral estimation case, the Burg order was 5;

Figure 3.7A illustrates a random reflectivity that has a low amplitude interval located between 1.5 – 3 seconds. The minimum-phase source signature convolved with this reflectivity model was attenuated with a constant Q filter (Q=25). This represents the input trace, before deconvolution (Figure 3.7G, same as in Figure 3.4). In Figure 3.7B, is illustrated the reflectivity after a nonstationary minimum-phase bandpass filter (8 - 13- 180 (at 1 second) – 240 (at 1 second) Hz) has been applied in the Gabor domain (see Figure 3.8).
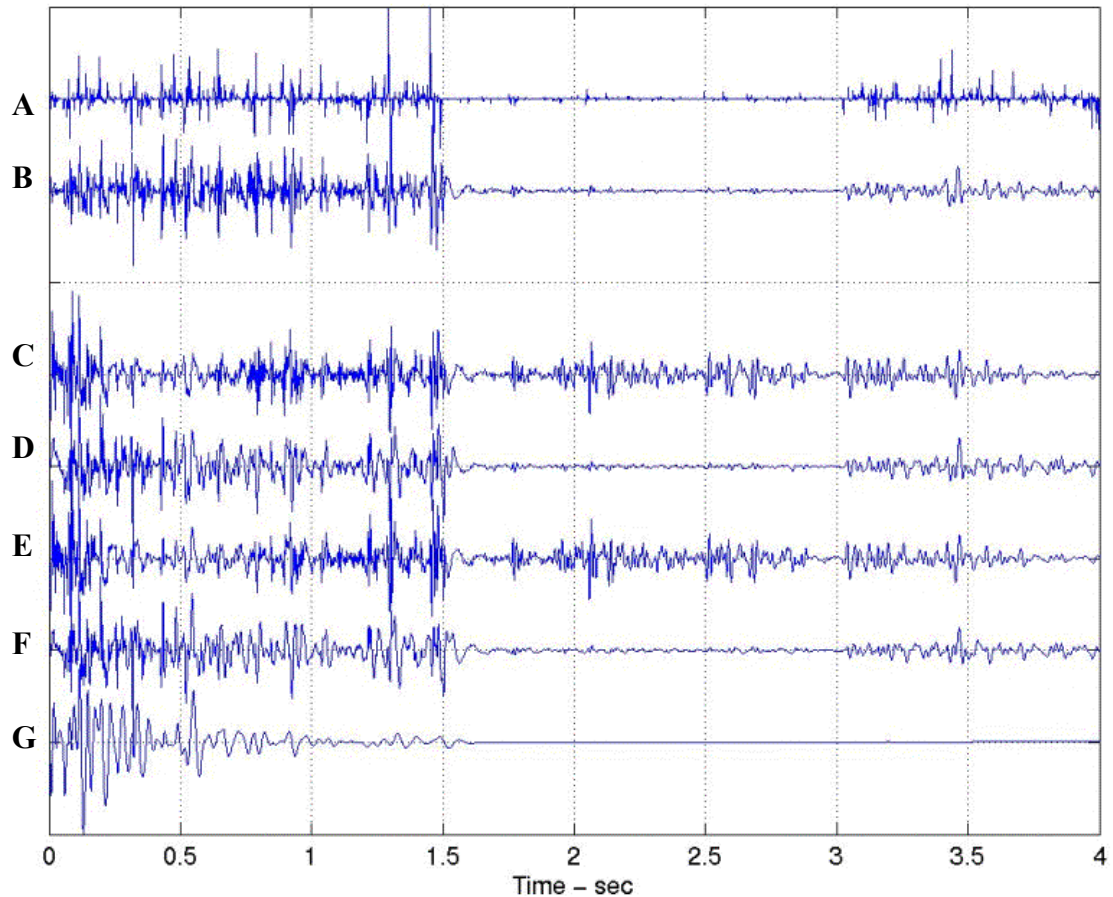
Figure 3.7.: Time domain results. Trace **A** is the exact reflectivity; trace **B** is the bandpass filtered version of the trace **A** (using the filter of Figure 3.8). Trace **C** is the result of the deconvolution using a boxcar smoother, DFT spectral estimation. Trace **E** is the result of the deconvolution using a boxcar smoother, Burg spectral estimation. Trace **D** is the deconvolution result from the hyperbolic smoother algorithm in the DFT case. Trace **F** is the deconvolution result from the hyperbolic smoother algorithm in the Burg case .Trace **G** is the attenuated trace (Q=25) that was input to the deconvolutions.

The high-cut value of the filter was set to a maximum 0.7 of the Nyquist frequency, this value decreasing hyperbolically (on a contour of $f\tau=constant$) for longer times (Figure 3.8). This bandlimited reflectivity will be compared with the deconvolution results. Since the frequency bandlimit tracks along a hyperbolic path in time-frequency domain, it corresponds to some constant power level in the attenuation function. Given a constant power background noise, we expect the signal to drop below

noise level along such a contour. The deconvolution results are also bandpass filtered with the same filter.
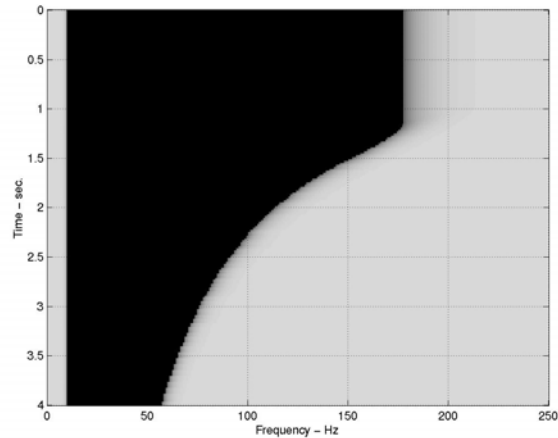

Figure 3.8.: Nonstationary bandpass filter in Gabor domain. Black is 1 and gray is 0, (filtered area).

In Figures 3.9a and 3.9b are represented the Gabor magnitude spectra (calculated with the DFT and Burg methods) of the attenuated trace (Figure 3.7G). The Burg spectral estimation is smoother than the straightforward DFT. Figure 3.10. represents the magnitude Gabor spectrum (DFT estimation) of the filtered reflectivity (Figure 3.7B), the reference plot to compare the results of the Gabor deconvolution. In both Figures 3.9a and 3.9b, the effect of the constant Q attenuation function can be easily observed.
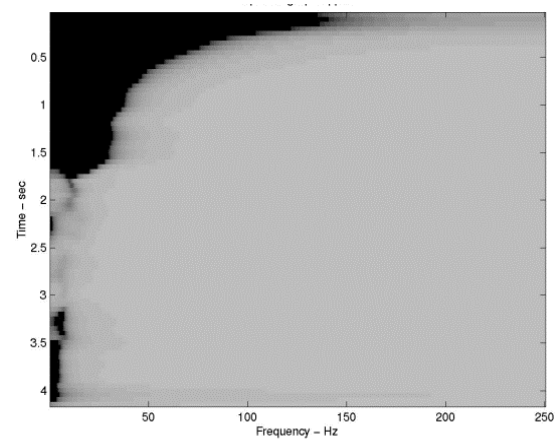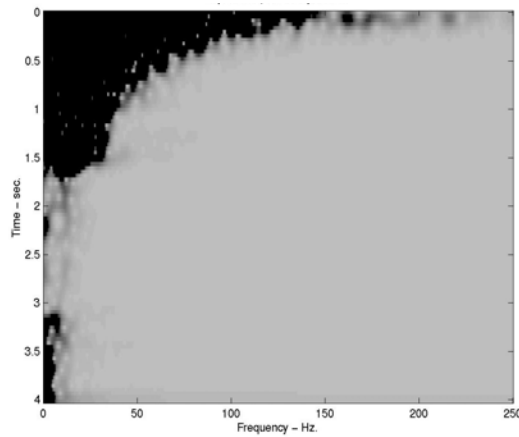
Figure 3.9a.: Gabor-magnitude spectrum (DFT estimation) of the attenuated trace (Figure 3.7E). This is displayed with a high gain to show subtle detail but the amplitude roll-off below 10 Hz is suppressed. Black represents positive numbers and light gray is 0.

Figure 3.9b.: Gabor-magnitude spectrum (Burg estimation) of the attenuated trace (Figure 3.7E). This is displayed with a high gain to show subtle detail but the amplitude roll-off below 10 Hz is suppressed. Black represents positive numbers and light gray is 0.
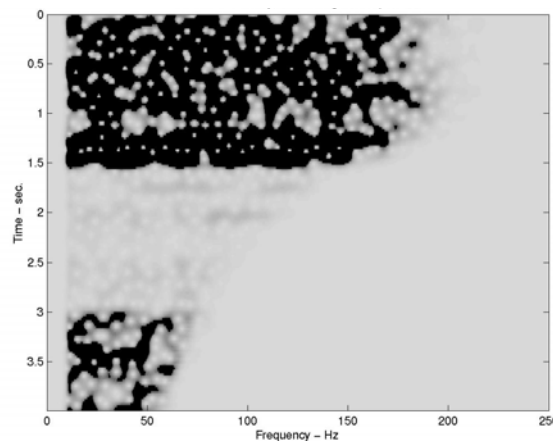
Figure 3.10.: Gabor magnitude spectrum (DFT estimation) of the filtered reflectivity (trace B in Figure 3.7). Black represents positive numbers and light gray is 0.

In Figures 3.11a and 3.11b (3.11a - DFT spectral estimation, 3.11b - Burg spectral estimation) is illustrated the product $\{|\hat{w}(f)||a(\tau, f)|\}_{est}$, as described by Equation (3.38). These are the smoothed magnitude spectra in the boxcar case. The time dimension of the boxcar was set to 0.5 seconds and the frequency dimension was 10 Hz.

Figure 3.11a.: Smoothed Gabor magnitude spectrum (DFT estimation) in the boxcar case (Equation 2.38). This is displayed with a high gain to show subtle detail but the amplitude roll-off below 10 Hz is suppressed. Black represents positive numbers and light gray is 0.
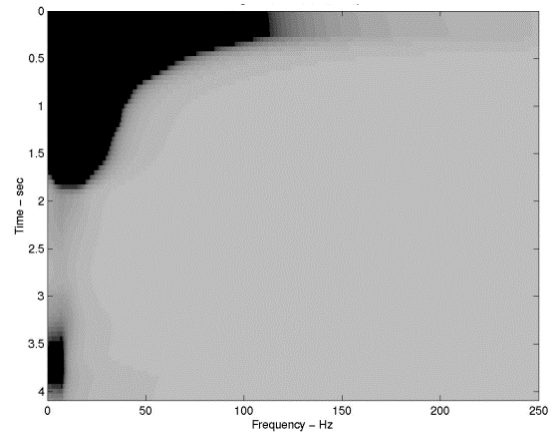
Figure 3.11b.: Smoothed Gabor magnitude spectrum (Burg estimation) in the boxcar case (Equation 2.38). This is displayed with a high gain to show subtle detail but the amplitude roll-off below 10 Hz is suppressed. Black represents positive numbers and light gray is 0.
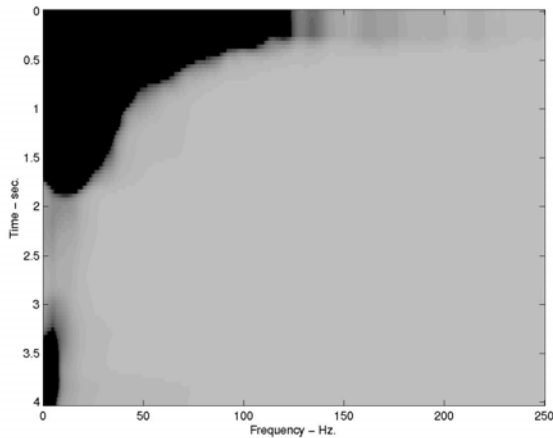
The results of the deconvolved traces using the boxcar smoother are illustrated in Figures 3.12a and 3.12b. The spectra of Figures 3.12a and 3.12b are obtained by dividing the spectra of Figures 3.9a and 3.9b by those of Figure 3.11a and 3.11b. Analyzing Figures 3.10, 3.11 and 3.12, as well as the traces in the time domain (in Figure 3.7, trace 3.7B to be compared with 3.7C-DFT, 3.7E-Burg), it is apparent that the boxcar has equalized the amplitudes in the weak and strong reflectivity zones in both cases of the spectral estimation. It is concluded that the boxcar has an effect similar to an AGC (or TVSW) operator applied to the trace, whereas, as it will be discussed below, the hyperbolic smoother more accurately restored the relative amplitudes.
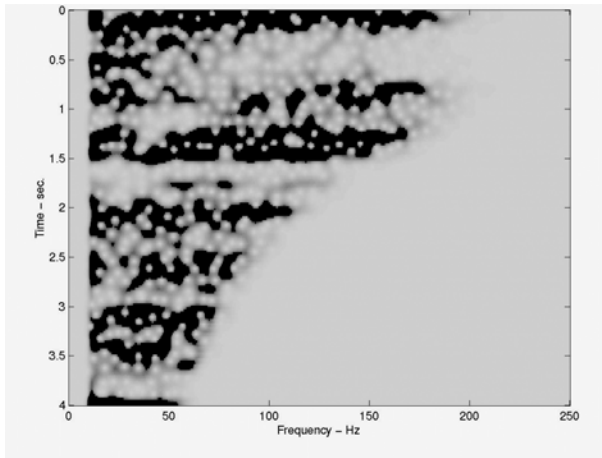
Figure 3.12a.: Gabor magnitude spectrum (DFT estimation) of the deconvolved trace, boxcar smoother, size 0.5 sec. x 10 Hz in time domain trace at position 3.7C in Figure 3.7). Black represents positive numbers and light gray is 0.
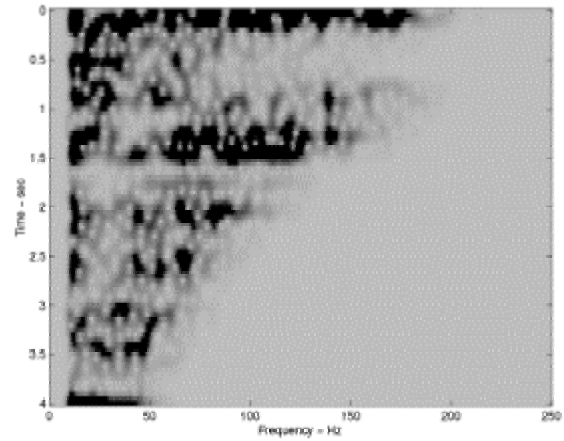
Figure 3.12b.: Gabor magnitude spectrum (Burg estimation) of the deconvolved trace, boxcar smoother, size 0.5 sec. x 10 Hz in time domain trace at position 3.7E in Figure 3.7). Black represents positive numbers and light gray is 0.

Figures 3.13a (DFT spectral estimation) and 3.13b (Burg spectral estimation) represent the results of the product $\left|\hat{w}(f)\right|_{est}\left|a(\tau,f)\right|_{est}$, as described by Equation (3.42) before inversion.

Figure 3.13a.: Smoothed Gabor magnitude spectrum (DFT estimation), hyperbolic smoother case. Equation (3.42) before inversion. Black represents positive numbers and light gray is 0.
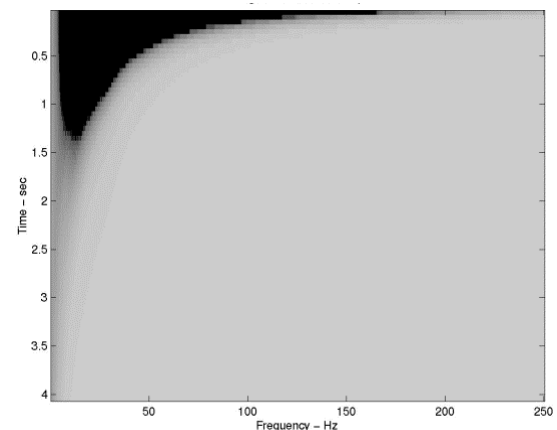
Figure 3.13b.: Smoothed Gabor magnitude spectrum (Burg estimation), hyperbolic smoother case. Equation (3.42) before inversion. Black represents positive numbers and light gray is 0.

A (physically) valid estimate of the product $\left|\hat{w}(f)\right|\left|a(\tau,f)\right|$ must show steadily decreasing power with increasing time. In particular, the estimates of Figures 3.11a and 3.11b cannot be physically correct because the power increases abruptly at about 3 seconds. The low power zone from approximately 1.5 seconds to 3 seconds is a residual imprint of the reflectivity that was not removed by the boxcar smoother in either case of spectral estimation, DFT or Burg. The estimates of Figures 3.13a and 3.13b are much more plausible though it is not mathematically proved in this work that hyperbolic smoothing will always give a correct result.

In Figures 3.14a. (DFT spectral estimation) and 3.14b (Burg spectral estimation) are the results of the hyperbolic smoother (Gabor domain), the traces at positions D and F in Figure 3.7. The spectra of Figures 3.14a and 3.14b were obtained by dividing the spectra of Figure 3.9a and 3.9b by that of Figures 3.13a and 3.13b.
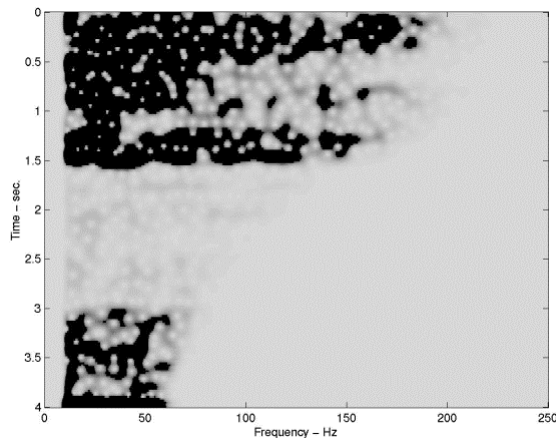
Figure 3.14a.: Gabor magnitude spectrum (DFT estimation) of the deconvolved trace, hyperbolic smoother. Compare to Figure 3.10.
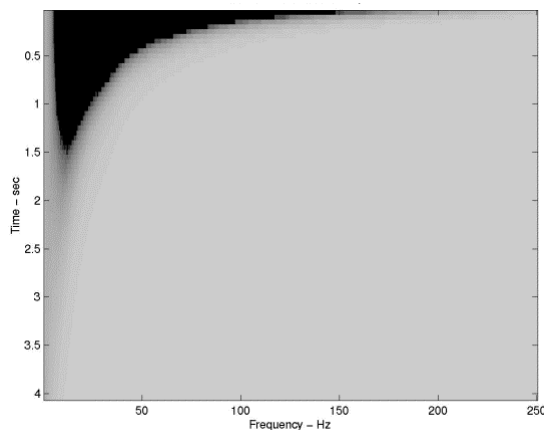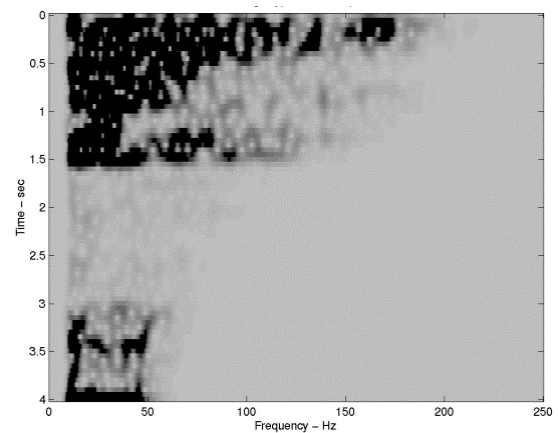
Figure 3.14b.: Gabor magnitude spectrum (Burg estimation) of the deconvolved trace, hyperbolic smoother. Compare to Figure 3.10.

3.4.1 Discussion and conclusions for the synthetic case

The relative amplitudes of the particular model, tested in this section, are more correctly restored by the Gabor deconvolution performed with a hyperbolic smoother. In the boxcar smoother case the restoration of the relative amplitudes is poor and this constitutes a major drawback of this type of smoother. The temporal size of the smoother, as well as the length in frequency are important parameters in designing the deconvolution operator but in any case, the result of the boxcar smoother will be limited by the fact that it cannot provide simultaneously a satisfactory whitening level and amplitude restoration.
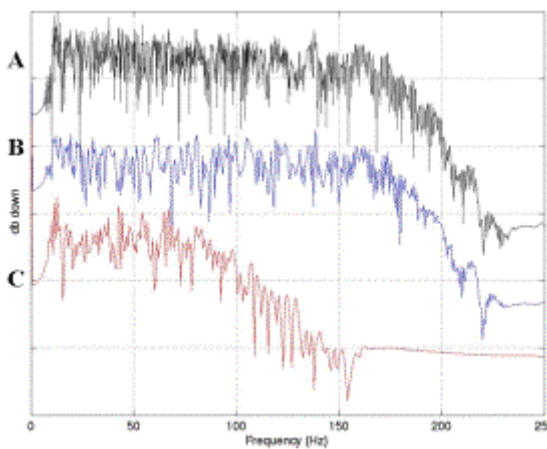
Figure 3.15a.: Frequency magnitude spectrum of the trace deconvolved with a boxcar (DFT estimation). A – whole trace, B - windowed between 0-1.5 seconds, C - windowed between 1.5-3 seconds.
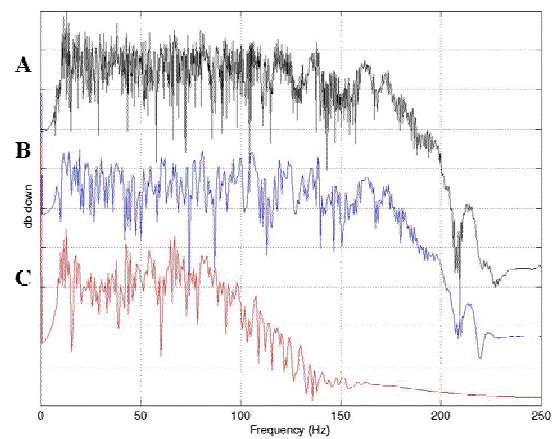
Figure 3.15b.: Frequency magnitude spectrum of the trace deconvolved with a boxcar (Burg estimation). A – whole trace, B - windowed between 0-1.5 seconds, C - windowed between 1.5-3 seconds.
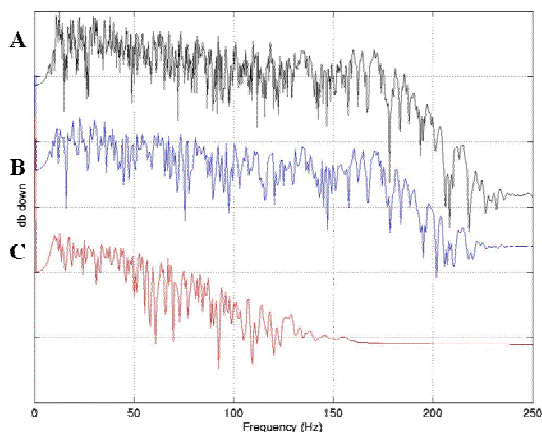
Figure 3.15c.: Frequency magnitude spectrum of the trace deconvolved with the hyperbolic smoother (DFT estimation). A – whole trace, B - windowed between 0-1.5 seconds, C - windowed between 1.5-3 seconds.
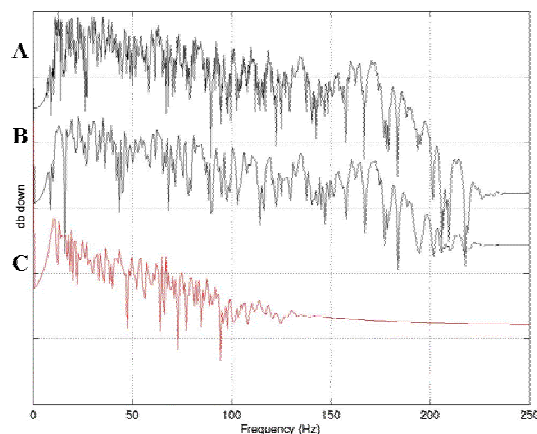
Figure 3.15d.: Frequency magnitude spectrum of the trace deconvolved with the hyperbolic smoother (Burg estimation). A – whole trace, B - windowed between 0-1.5 seconds, C - windowed between 1.5-3 seconds.

In Figure 3.15a at position A is the Fourier magnitude spectrum of the entire trace deconvolved with the boxcar (Figure 3.7C) and using the DFT approach for spectral estimation. At position B is the Fourier magnitude spectrum of the same trace windowed between 0 to 1.5 seconds and at position C the Fourier magnitude spectrum of the trace windowed between 1.5 to 3 seconds. The whitening achieved by the boxcar filter is excellent in all three cases. The same statement can be repeated in the Burg spectral estimation case (illustrated in figure 3.15b). In the case of the hyperbolic smoother, the whitening level achieved after deconvolution is illustrated in Figure 3.15c (in the DFT case), positions A, B, and C. The Fourier magnitude spectrum of the entire trace that was deconvolved with the hyperbolic smoother is at position A, whereas positions B and C the windowed intervals are between 0 to 1.5 seconds and 1.5 to 3 seconds, respectively. In the hyperbolic smoother example, the magnitude spectrum is slightly less white than in the case of the boxcar smoother. Similar to the DFT spectral estimation, in the hyperbolic Burg case (Figure 3.15d), the magnitude spectrum is slightly less white than in the boxcar Burg example.

The superiority of the hyperbolic smoother comes from the form of the constant Q attenuation function in Equation (2.17). Figures 3.13a and 3.13b illustrate the estimates of the attenuation combined with the source signature in DFT and Burg cases of the trace in the time-frequency plane obtained from the input trace, Equation (3.45), before inversion. Physically, these estimates are more plausible than the estimates provided by the boxcar smoother (Figures 3.11a and 3.11b). When analyzing the Fourier magnitude spectrum of the deconvolved trace on different time intervals, in the hyperbolic smoother case, (see Figures 3.15c and 3.15b) it is noted that the degree of whitening is not at the same level as in the boxcar smoother case. For all three intervals analyzed (the entire trace in examples A, from 0 to 1.5 seconds in examples B, and from 1.5 to 3 seconds in examples C, the degree of decaying of the power in frequency domain is relatively constant in all cases.

3.5 Application on real data of the Gabor deconvolution

This section compares, from an interpretation point of view, the results of stationary Wiener deconvolution (described in section 1.2) and Gabor deconvolution (described in section 3.2.2). The Wiener deconvolution is followed by time variant spectral whitening (TVSW) technique applied to the stacked section as a standard procedure to increase resolution. Gabor deconvolution was applied before stacking to the raw data, and again after stack, replacing the TVSW technique.

In the Gabor deconvolution case, either minimum phase or zero phase can be chosen whereas the TVSW technique is only a zero phase process. In this test, Gabor deconvolution was applied with a minimum-phase operator after stacking and a comparison with the Wiener section (Wiener spiking, minimum-phase deconvolution, before stacking, and TVSW technique, after stacking) will be presented at the end.

3.5.1 Acquisition parameters and a brief geological description

The Blackfoot field is located in Township 23, Range 23, West of the 4th Meridian, near Strathmore, Alberta. The line was recorded in 1997 using 3C geophones and is oriented east to west in the Blackfoot field. From the three components recorded the vertical component was used to test the Gabor deconvolution because it represents the industry standard. The receiver interval was 20 m and there were 151 receiver stations in total. The stacking fold is about 159 in the middle of the line. The exploration objective of this line was to image the incised paleo-valleys within the Glauconitic sandstones of the Lower Cretaceous Mannville Group. The Glauconitic sandstones ranges from zero to 40 m in thickness and are found in structural and stratigraphic traps. Reservoir rocks are subdivided in this area into three units corresponding to three phases of incision (Figure 3.16): Lower Channel, Lithic Channel, and Upper Channel. According to Miller et al. (1995), all three units may not be present everywhere. On the seismic displays in this section, the incised channels appear between the CDP's 320 to 380, in the time window from 1.05 to 1.1 seconds.
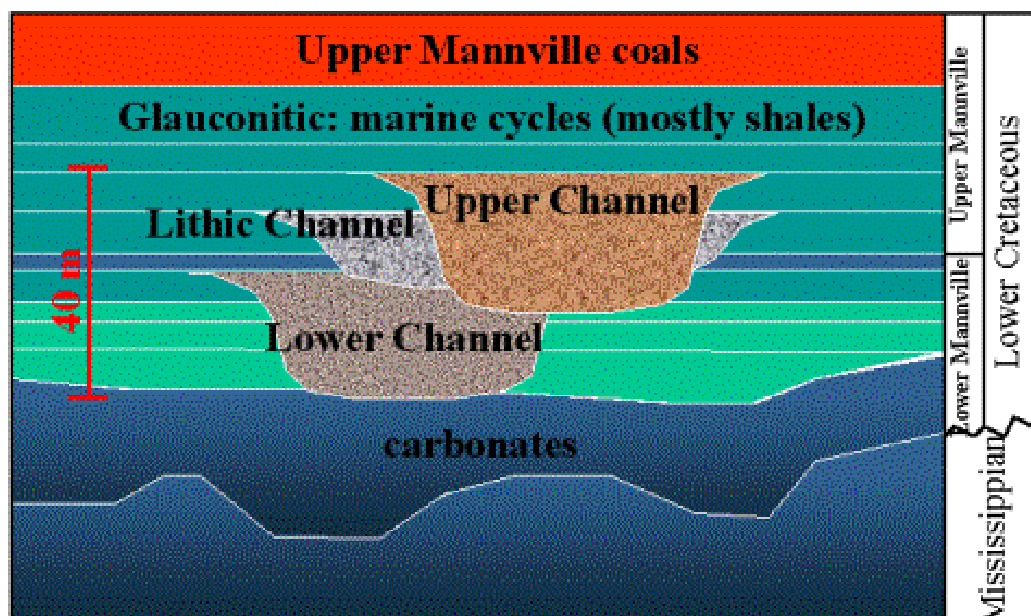
Figure 3.16.: Schematic stratigraphy of the Blackfoot area showing the three different incised valleys. After Margrave, 2001.

3.5.2. Gabor deconvolution parameters

Gabor deconvolution was implemented in Promax by Henley and Margrave, (2001) and an equivalent presentation of these parameters may be found in the CREWES report of 2001 (or in the documentation of the ProMAX processing software under CREWES modules).

The width of the analysis window is an important parameter in the sense that a wide analysis window will have excellent resolution in frequency but poor temporal resolution and a short analysis window will have greater time resolution but poor frequency resolution. There is little physical justification in using a window narrower than the length of the embedded wavelet, which is presumed to be within 0.1-0.4 seconds in length. A real trace (in time domain) from the Blackfoot data is represented in Figure 3.17. In Gabor domain, a short analysis window length provides detailed time

information at the expanse of the frequency resolution, in conformity to the Heisenberg's uncertainty principle. The Gabor magnitude spectra for an analysis window of 0.2 seconds are illustrated in Figures 3.18a (DFT spectral estimation) and 3.18b (Burg spectral estimation of order 5).

Figure 3.17.: Real trace from Blackfoot data.

Figure 3.18a.: Gabor magnitude spectrum (DFT estimation) of the real trace from Figure 3.17). Gaussian length = 0.2 seconds. Time increment = 0.04 seconds.

Figure 3.18b.: Gabor magnitude spectrum (Burg estimation, order 5) of the real trace from Figure 3.17). Gaussian length = 0.2 seconds. Time increment = 0.04 seconds.

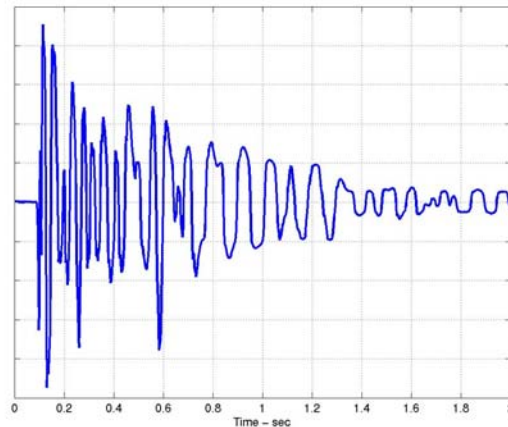In Figures 3.19a (DFT spectral estimation) and 3.19b (Burg spectral estimation of order 5) are illustrated the Gabor magnitude spectra for an analysis window of 0.4 seconds.

Figure 3.19a.: Gabor magnitude spectrum (DFT estimation) of the real trace from Figure 3.17). Gaussian length = 0.4 seconds. Time increment = 0.04 seconds.

Figure 3.19b.: Gabor magnitude spectrum (Burg estimation, order 5) of the real trace from Figure 3.17). Gaussian length = 0.4 seconds. Time increment = 0.04 seconds.

In this application, the length of the Gaussian window was chosen to be 0.4 seconds.

Another important parameter is the time increment between analysis windows. This parameter controls the redundancy of the Gabor spectrum and directly influences the computation time. It also determines the minimum possible time scale on which the algorithm can adapt. This parameter depends on the window width described above and it should usually be set to less than the analysis window width. In Figures 3.18 and 3.19 the time increment between two consecutive windows was 0.04 seconds. In Figures 3.20 are shown , for comparison the Gabor magnitude spectra calculated with a time increment of 0.1 seconds. The resolution becomes coarser with a larger value for the time increment. For the Blackfoot data the time increment was set at 0.04 seconds for computational reasons, although the finer resolution is achieved when this parameter is set to 0.01 seconds (See Figures 3.21a and 3.21b for DFT and Burg order 5 spectral estimations).
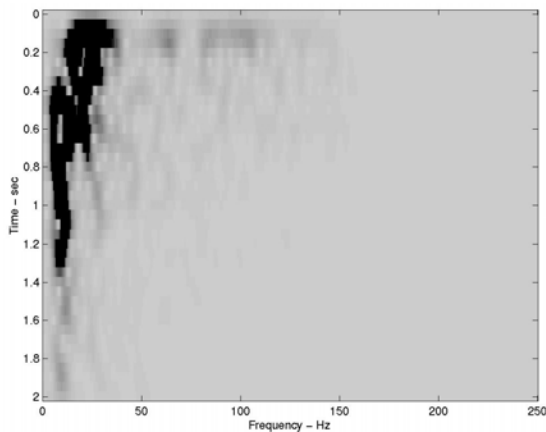
Figure 3.20a.: Gabor magnitude spectrum (DFT estimation) of the real trace from Figure 3.17). Gaussian length = 0.4 seconds. Time increment = 0.1 seconds.

Figure 3.20b.: Gabor magnitude spectrum (Burg estimation, order 5) of the real trace from Figure 3.17). Gaussian length = 0.4 seconds. Time increment = 0.1 seconds.
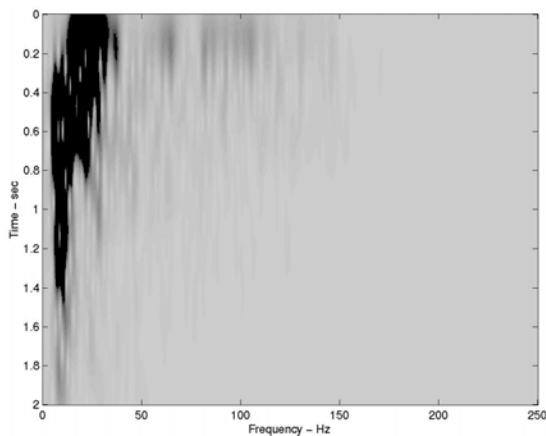
Figure 3.21a.: Gabor magnitude spectrum (DFT estimation) of the real trace from Figure 3.17). Gaussian length = 0.4 seconds. Time increment = 0.01 seconds.
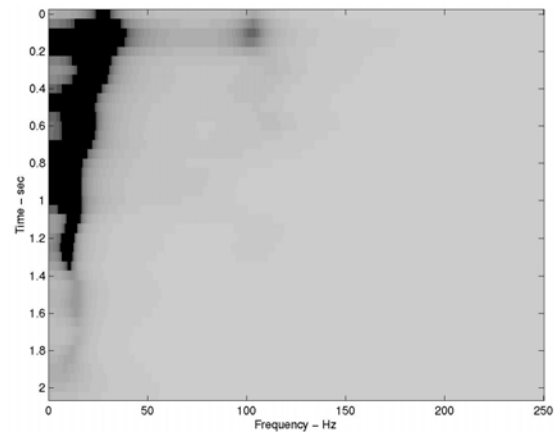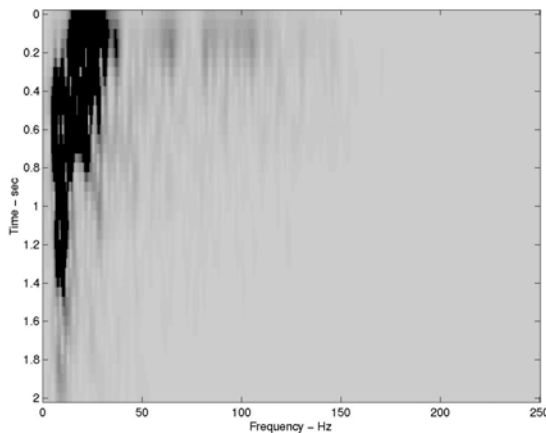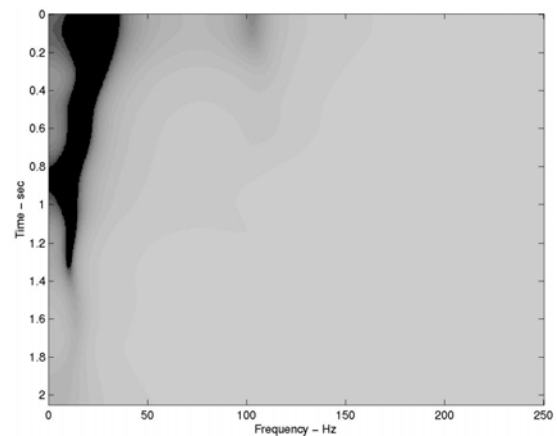

Figure 3.21b.: Gabor magnitude spectrum (Burg estimation, order 5) of the real trace from Figure 3.17). Gaussian length = 0.4 seconds. Time increment = 0.01 seconds.

The third parameter used in the Gabor deconvolution is the method of spectral estimation, which can be a straightforward DFT or the Burg spectrum (Claerbout, 1976) of the windowed signal, as discussed in section 2.4. In Figures 3.18 to 3.21 at position a is the straightforward DFT spectral estimation whereas at position b, the Burg of order 5. In the case of the Burg algorithm, the order of the PEF coefficients used in calculating the

Burg spectrum is inversely proportional to the smoothness of the resulting spectral estimate. For example, a small coefficient number is similar to using the Fourier estimation and applying stronger smoothing. In the processing flow, five coefficients were used for the deconvolution of the raw data and twelve for whitening the stacked data. The Gabor magnitude spectrum calculated with Burg PEF of order 12 is illustrated in Figure 3.22 for a comparison to Figure 3.21b (Burg spectral estimation of order 5). The computational time also increases when a larger order is used.
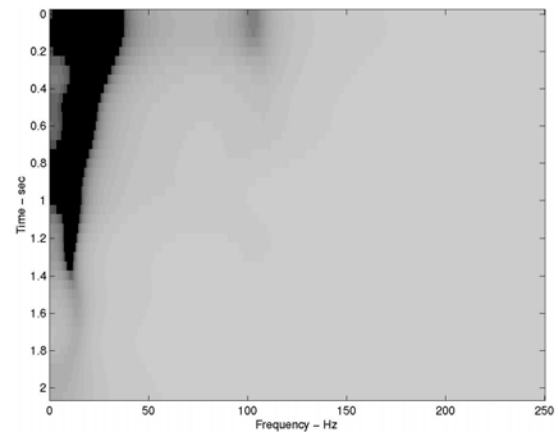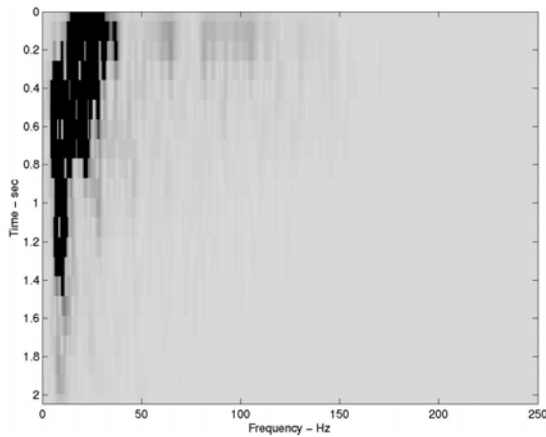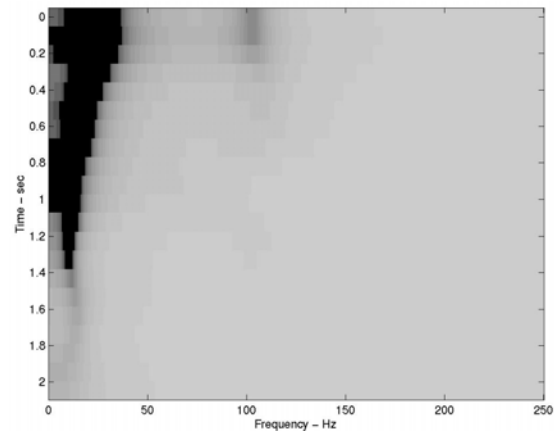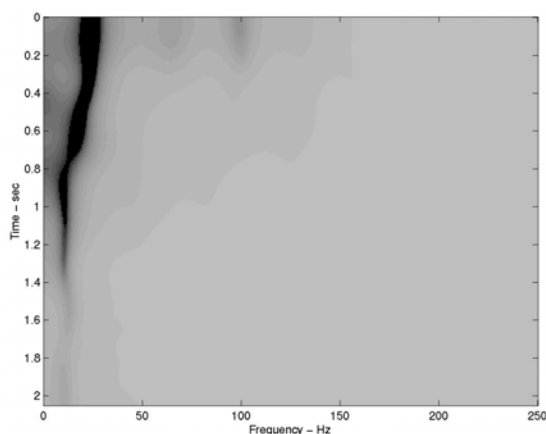

Figure 3.22.: Gabor magnitude spectrum (Burg estimation, order 12) of the real trace from Figure 3.17). Gaussian length = 0.4 seconds. Time increment = 0.01 seconds. To be compared to Figure 3.21b.

The fourth parameter controls the phase of the deconvolution operator, which can be zero phase or minimum phase. Both of these options were tested. Assuming that the data is minimum phase, the minimum-phase option is to be preferred to zero phase. This was the first option for the Gabor deconvolution applied before and after stack.

The deconvolution operator can be derived from the magnitude (linear) Gabor spectrum or from the logarithmic Gabor spectrum of the data. Both choices were examined and the magnitude spectrum was used because it resulted in a stronger whitening of the data.

The number of passes of the smoothing operator is a parameter which determines how many times the smoother is applied to the Gabor spectrum for wavelet estimation.

This parameter was set to unity for the Fourier and Burg method in the Gabor deconvolution applied before stack and 16 for the second application, after stacking. If the smoother geometry is a boxcar, applying it many times is similar to smoothing with a very large Gaussian. (This is a consequence of the central limit theorem; Claerbout, 1976.)

Two types of smoothing of the magnitude spectrum were used, the boxcar smoother and the hyperbolic smoother.

In the boxcar smoother case, the frequency dimension of the smoothing window determines the number of the points to be smoothed along the frequency axis. This parameter was set to 21 Hz first pass in the flow and 16 Hz second time, after stacking. The frequency dimension controls the temporal size of the assumed wavelet estimate. Shorter wavelets have smoother spectra. The time dimension of the smoothing operator determines the number of spectral magnitude points to be smoothed in time. This parameter was set to 0.8 seconds in the first pass in the flow, and 0.5 seconds in the post-stack process. This parameter controls the nonstationarity of the deconvolution. The longer this value, the more stationary the deconvolution becomes.

In the hyperbolic smoother case, the corridor width of the hyperbolic smoother in Hz and seconds is a parameter which set the width of the hyperbolic contour. After several tests it was determined that, in the Blackfoot data example, this parameter has no significant role, and the final value was set to 4 Hz-seconds.

The stability factor is similar to adding white noise as in stationary deconvolution, to prevent any division by zero. The value was set to 0.0001.

3.5.3 Spiking deconvolution & TVSW parameters

In the case of Wiener spiking deconvolution some parameter testing was done and the parameters with the best results were established. A detailed description of these parameters can be found in Yilmaz (1987) and the documentation of the ProMAX processing software.

The type of deconvolution was minimum phase spiking with a deconvolution operator length of 0.24 seconds. The Wiener design gate was set between 700 and 1900 milliseconds. The white noise level was set to 0.001.

For the TVSW technique the spectral-balancing scalar length was 1 second and 12 filter panels were used. The lowest frequency whitened was 10 Hz and the highest was 100 Hz. Yilmaz (1987) describes this method.

3.5.4 Processing flows

Two similar processing sequences have been used in parallel to test Gabor deconvolution and to compare it with the familiar Wiener deconvolution. In the case of Wiener spiking deconvolution the flow is shown in Figure 3.23. The Gabor deconvolution processing flow is shown in Figure 3.24. Comparing these two processing sequences a number of differences become evident. In the case of Gabor deconvolution the exponential gain correction was omitted from the flow because the nonstationary nature of the process causes it to boost the amplitudes. Second, for velocity analysis and residual statics only a bandpass filter was necessary in the Gabor deconvolution case, whereas in the Wiener case, automatic gain correction (AGC) was applied to the traces before the bandpass filtering. A third difference is after stacking where, in order to enlarge the bandwidth of the data (to increase the resolution of the sections), the TVSW process was applied to the Wiener spiking section, whereas for the Gabor sections, the

Gabor deconvolution was run a second time, with the parameters specified above, in section 3.5.2.

```
┌─────────────────────────────────────────┐
│   SEG -Y FORMATTED DE-MULTIPLEXED INPUT  │
└─────────────────────────────────────────┘
          2D GEOMETRY ASSIGNMENT
               TRACE EDIT
         SPHERICAL DIVERGENCE CORR.
         EXPONENTIAL GAIN CORR.
       WIENER SPIKING DECONVOLUTION
```

AGC/BP filter ← ELEVATION STATICS

VELOCITY ANALYSIS → NORMAL MOVEOUT → AGC/BP filter

RESIDUAL STATICS ← RESIDUAL STATICS ANALYSIS

AGC or TE

CDP STACK — Correlation model →

TIME VARIANT SPECTRAL WHITENING

SPATIAL PREDICTION

PHASE SHIFT MIGRATION
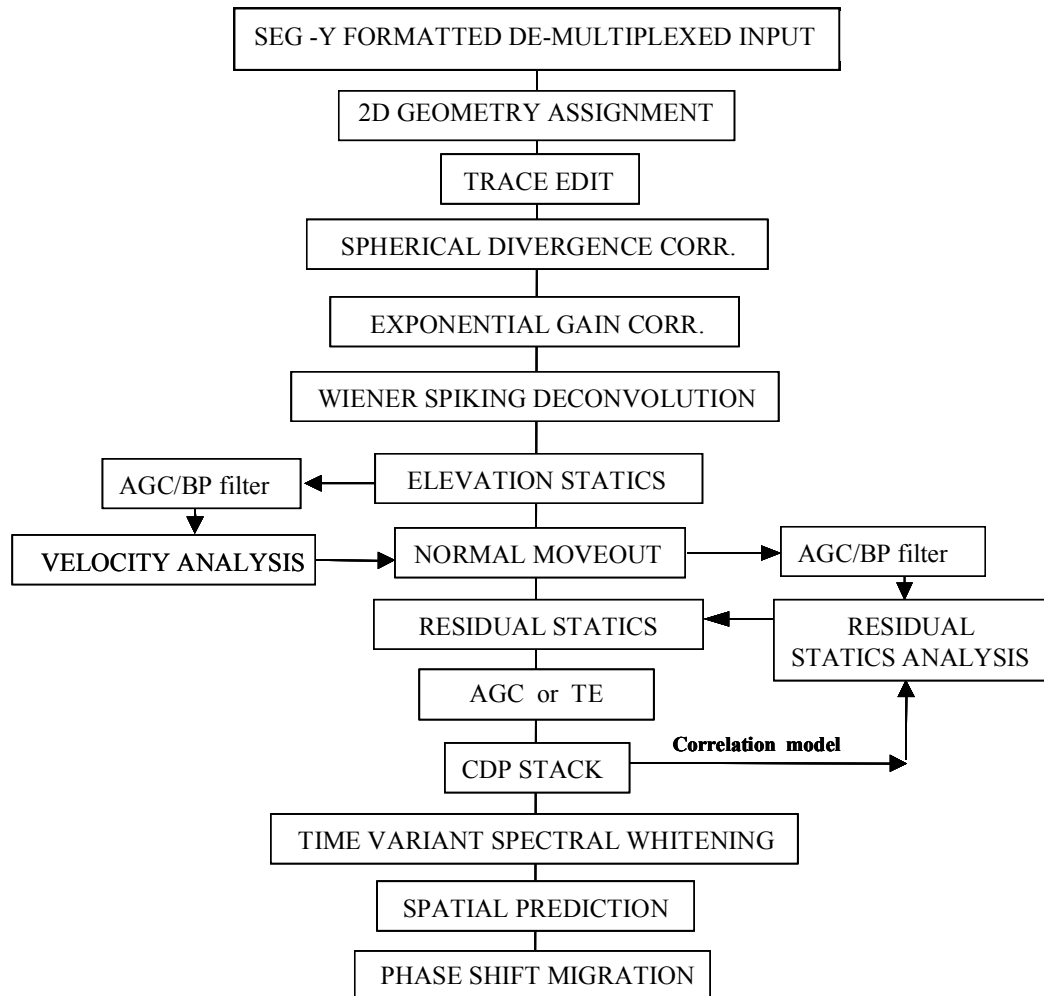
Figure 3.23.: The processing flow of the Wiener spiking deconvolution. The result of this flow is the Wiener/TVSW section.

```
            ┌─────────────────────────────────────────────┐
            │   SEG -Y FORMATTED DE-MULTIPLEXED INPUT      │
            └─────────────────────────────────────────────┘

                ┌─────────────────────────────┐
                │   2D GEOMETRY ASSIGNMENT     │
                └─────────────────────────────┘

                     ┌──────────────┐
                     │  TRACE EDIT  │
                     └──────────────┘

                ┌──────────────────────────────┐
                │  SPHERICAL DIVERGENCE CORR.   │
                └──────────────────────────────┘

┌────────────────────────────────────────────────────────────────────────────┐
│ GABOR DECONVOLUTION, MIN PHASE: BOXCAR{DFT/BURG} or HYPERBOLIC{DFT/BURG}     │
└────────────────────────────────────────────────────────────────────────────┘

        ┌──────────────┐       ┌───────────────────────┐
        │   BP filter  │◄──────│   ELEVATION STATICS    │
        └──────────────┘       └───────────────────────┘

  ┌───────────────────┐       ┌────────────────────┐      ┌──────────────┐
  │  VELOCITY ANALYSIS│──────►│   NORMAL MOVEOUT    │─────►│   BP filter  │
  └───────────────────┘       └────────────────────┘      └──────────────┘

                       ┌────────────────────┐      ┌──────────────────────┐
                       │  RESIDUAL STATICS   │◄─────│   RESIDUAL STATICS    │
                       └────────────────────┘      │      ANALYSIS         │
                                                   └──────────────────────┘
                         ┌──────────────┐
                         │   CDP STACK  │
                         └──────────────┘
                              Correlation model
┌────────────────────────────────────────────────────────────────────────────┐
│ GABOR DECONVOLUTION, MIN PHASE: BOXCAR{DFT/BURG} or HYPERBOLIC{DFT/BURG}     │
└────────────────────────────────────────────────────────────────────────────┘

                       ┌────────────────────┐
                       │  SPATIAL PREDICTION │
                       └────────────────────┘

                       ┌────────────────────┐
                       │ PHASE SHIFT MIGRATION│
                       └────────────────────┘
```
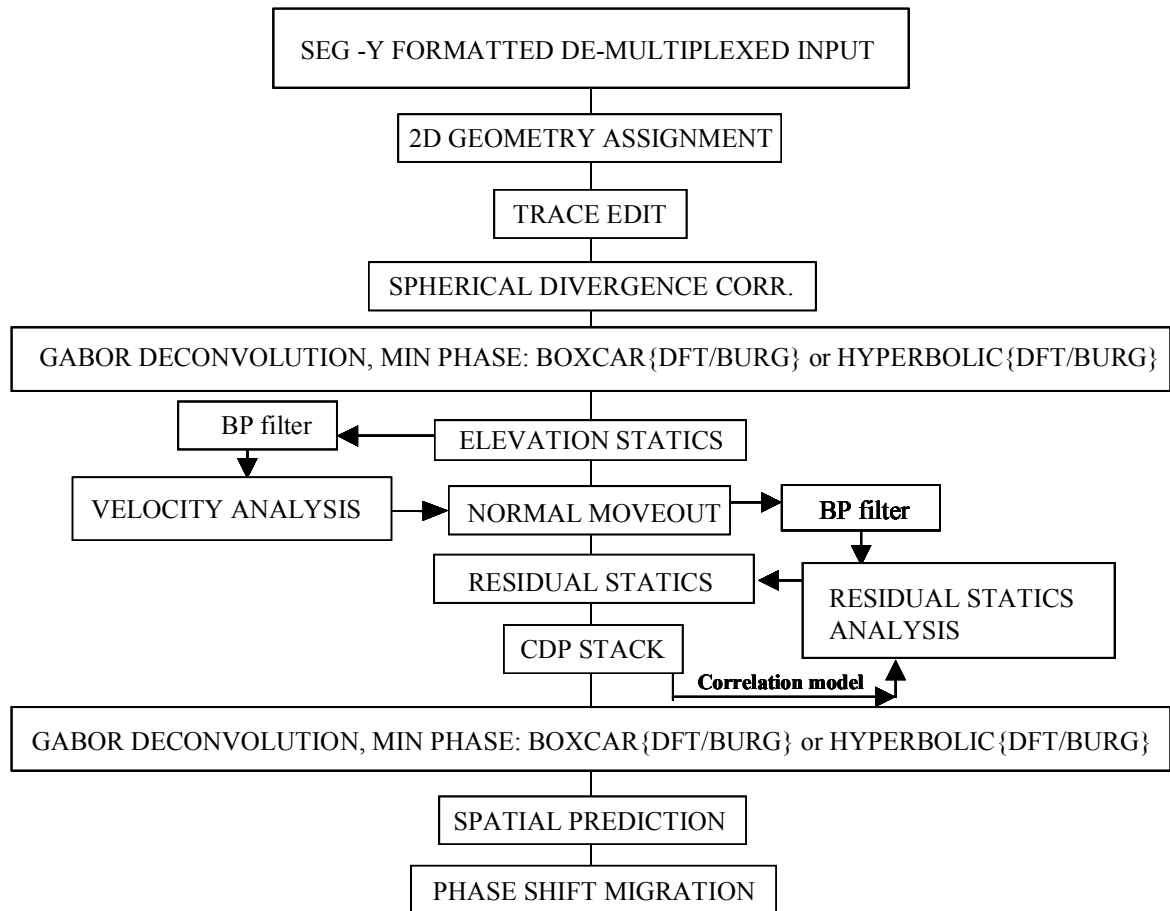
Figure 3.24.: The processing flow of the Gabor deconvolution sections. Four final sections can be generated by this flow: Gabor/DFT-boxcar, Gabor/Burg-boxcar, Gabor/DFT hyperbolic, and Gabor/Burg – hyperbolic. From these final sections only the Gabor/Burg with the boxcar and hyperbolic smoother were selected for a comparison to the Wiener deconvolution section.

3.5.5 Discussion and conclusions for Gabor deconvolution

A typical shot record is shown in Figure 3.25. Figure 3.26 displays the result of the Wiener deconvolution. The same shot record after the Gabor deconvolution (Burg method with boxcar smoother) is illustrated in Figure 3.27. Before Wiener deconvolution, exponential gain correction was applied to the data whereas Gabor deconvolution was

applied right after the spherical divergence correction without the exponential gain (see the processing flows in diagrams 3.23 and 3.24).

At least three significant differences are observed on these displays. First, Wiener deconvolution has overwhitened the data above the deconvolution gate, set between 0.7 and 1.9 seconds. A strong reflection can be seen at approximately 0.3 seconds in Figure 3.27 (Gabor deconvolution) but there is nothing coherent in Figure 3.26 (Wiener deconvolution). The overwhitening is a side-effect, typical in stationary processes where the operator is designed within a gate and then is applied to the whole data, due to the differences in the spectral ratios in different temporal windows. Secondly, in the zone of interest (0.8-1.4 seconds), events on Gabor display seem to be tighter and more compressed (better resolution). Thirdly, the ground roll has been better suppressed by Gabor deconvolution.
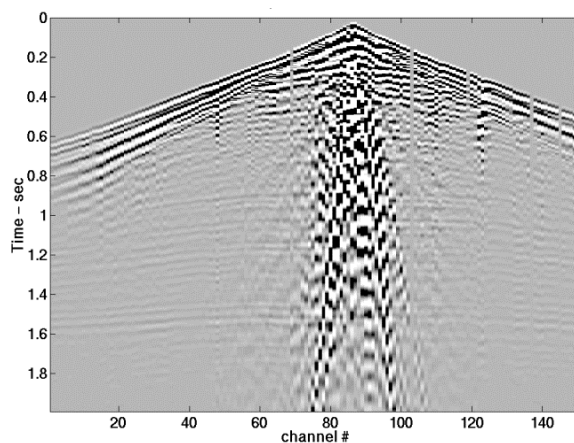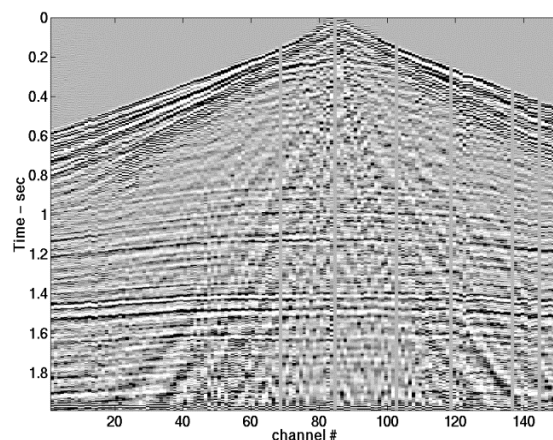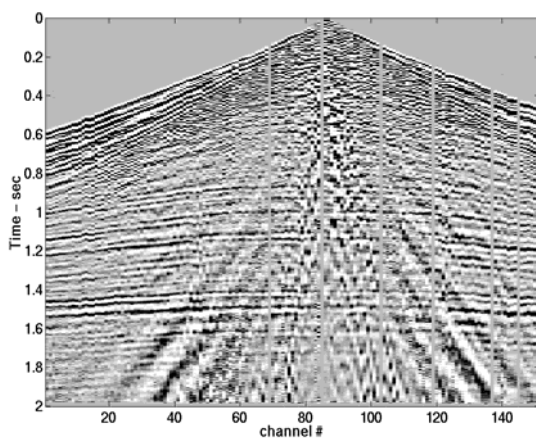
Figure 3.25.: Raw shot # 81.

Figure 3.26.: Shot # 81 after Wiener deconvolution. Trace Equalization (0.8 – 1.6 seconds) applied for display purpose.

Figure 3.27.: Shot # 81 after Gabor/Burg boxcar smoother deconvolution.

After deconvolution, elevation and static corrections were applied and a velocity analysis was conducted individually in both processing flows. Next, moveout corrections were applied using a set of preliminary velocity picks. Then residual statics corrections were calculated and applied. The velocity analysis were repeated to update the previous velocity picks and NMO corrections were applied again in an iterative process.

During the stacking process, the incoherent noise induced in the data by the deconvolution process is suppressed. Stacking process alone acts as a signal enhancement by attenuating the noncoherent noise. Even an f-k filter was unnecessary for the Blackfoot data, because the deconvolution processes (either the Wiener or Gabor) provided very good results in suppressing the coherent noise trains (e.g. ground roll).

The final sections, after the phase-shift migration, are illustrated in Figures 3.28 (Wiener section), 3.29 (Gabor/Burg with the boxcar section) and 3.30 (Gabor/Burg with the hyperbolic smoother). The Wiener deconvolution section (Figure 3.28), with a design gate of the deconvolution operator set in the zone of interest (0.7-1.9 seconds), lacks of coherence at shallow zones (0-0.4 seconds) compared to the Gabor method. This observation is consistent with the idea that the stationary deconvolution can work well within its design gate but not elsewhere. Nonstationary Gabor deconvolution is at least equal to Wiener in the latter's design gate and superior elsewhere.
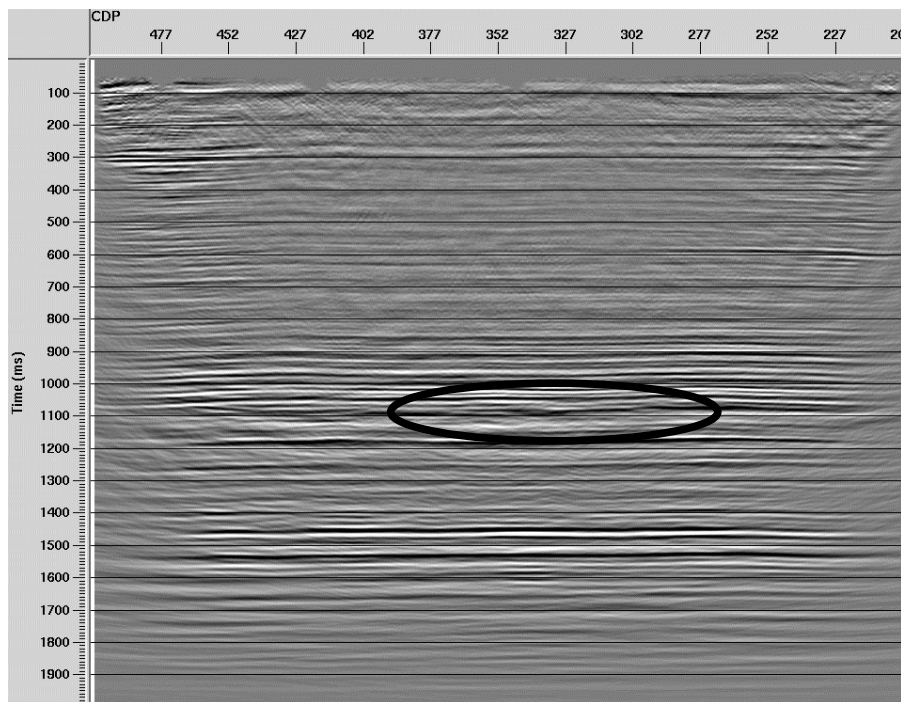

Figure 3.28.: Wiener/TVSW, final section . The Glauconitic channels are displayed in the black oval, around 1.1 seconds, between CDP's # 327-377.
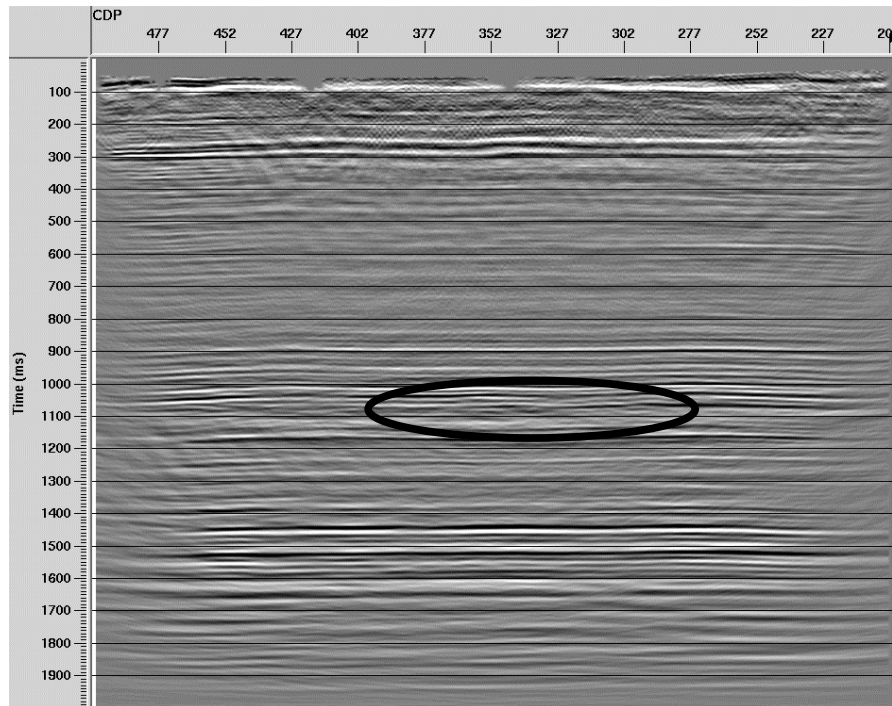
Figure 3.29.: Gabor/Burg boxcar smoother, final section. The Glauconitic channels are displayed in the black oval, around 1.1 seconds, between CDP's # 327-377.
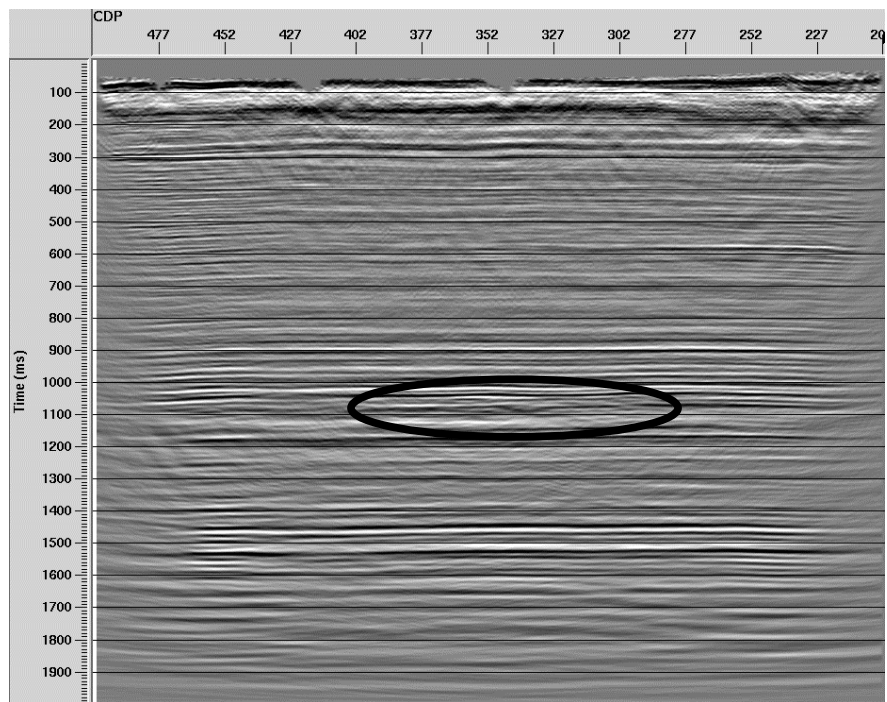

Figure 3.30.: Gabor/Burg hyperbolic smoother, final section. The Glauconitic channels are displayed in the black oval, around 1.1 seconds, between CDP's # 327-377.

Figures 3.31, 3.32, and 3.33 show in detail the Glauconitic channels (inside the black ovals), from the Wiener/TVSW (in Figure 3.28), Gabor/Burg boxcar (in Figure 3.29), and respectively Gabor/Burg hyperbolic (in Figure 3.30) sections. The difference between zero-phase TVSW technique applied in the Wiener flow and minimum-phase Gabor deconvolution applied after stacking can be better observed on these detailed figures. In the Gabor sections, all horizons are raised to earlier times because the zero-phase TVSW method applied after stacking cannot remove the residual wavelet phase effect, therefore, the events in the Gabor sections must be closer to the right position.
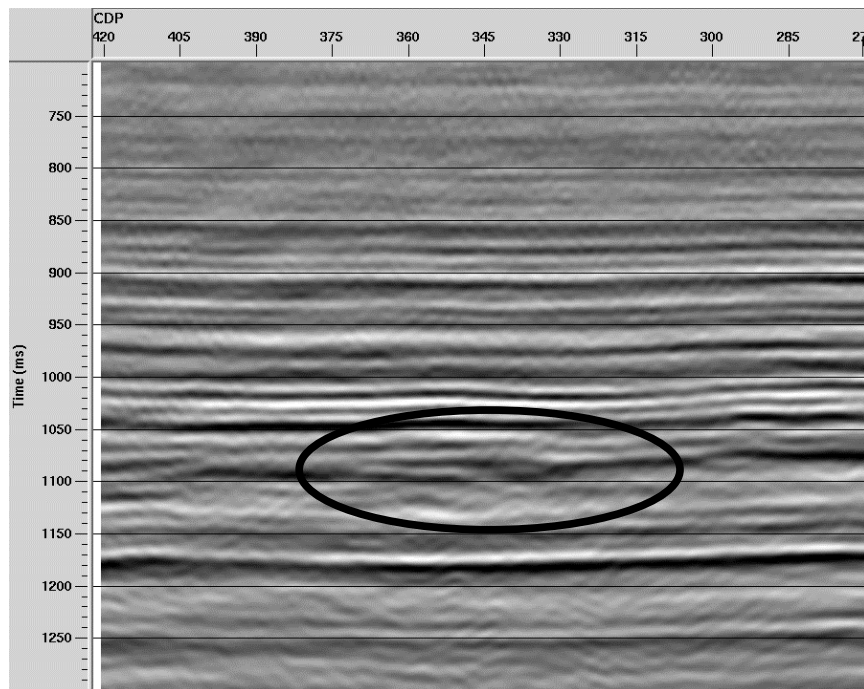

Figure 3.31.: Wiener/TVSW, final section, detail. The Glauconitic channels are inside the black oval.
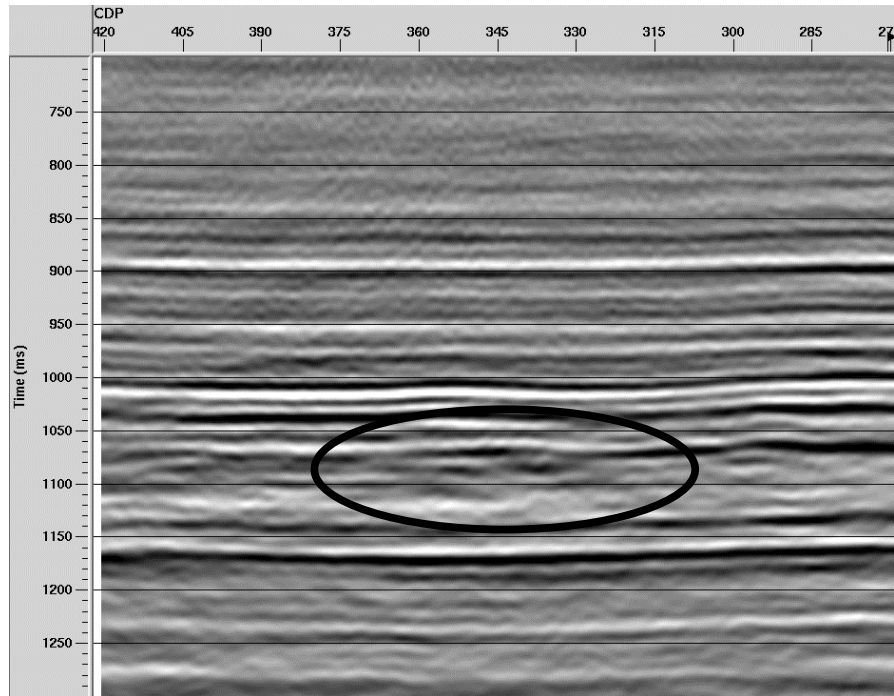
Figure 3.32.: Gabor/Burg boxcar smoother, final section, detail. The Glauconitic channels are inside the black oval.
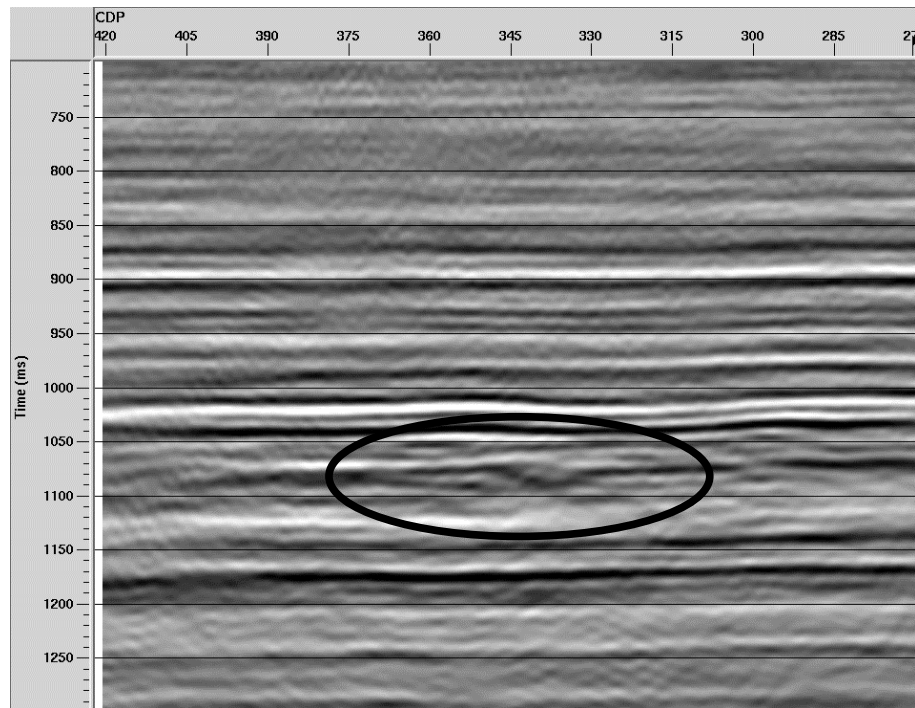

Figure 3.33.: Gabor/Burg hyperbolic smoother, final section, detail. The Glauconitic channels are inside the black oval.

3.5.6 Comparison of Gabor deconvolution and Wiener spiking deconvolution to synthetic seismograms

A zero-phase wavelet was used to create a set of synthetic seismograms from the well 09-08. In this section, the set of synthetic seismograms will be compared to the results from Gabor deconvolution (with the boxcar and hyperbolic smoother) and to the Wiener spking deconvolution, between 0 to approximately 1.07 seconds.

Three traces around the CDP # 337 from the Wiener stacked section (in dark gray) and three synthetic traces (in light gray) calculated from the well 0908, overlaid on the seismic traces are illustrated in Figure 3.34. The crosscorrelation between the synthetics and the real traces has been calculated to obtain a quantitative measure of the match. The crosscorrelation in the zero phase case (for the synthetics) was of 0.2034. In order to find the maximum value of the crosscorrelation the synthetic seismogram is rotated with constant phase angles from 0° to 180°. The maximum crosscorrelation in the Wiener deconvolution case was obtained for a rotation of 32 degrees (cc=0.2997).

Figure 3.35 illustrates the traces from the Gabor deconvolution in the boxcar smoothing case (in dark gray), overlaid by the synthetics (in light gray) from the same well. The crosscorrelation between the real data and the synthetics in the zero phase case (for the synthetics) was of 0.2404. The maximum crosscorrelation for the Gabor/Burg boxcar case was obtained for a rotation of 6° degrees (cc=0.2419).

Figure 3.36 illustrates the traces from the Gabor deconvolution in the hyperbolic smoothing case (in dark gray) which are overlaid by the synthetics (in light gray). The crosscorrelation between the real data and the synthetics in the zero phase case was of 0.3408. The maximum crosscorellation in this case was obtained for a rotation of 3° degrees (cc=0.3422) applied to the synthetics.

From these quantitative calculations results that the Gabor/Burg with the hyperbolic   smoother deconvolution performed best in this example. This statement is based upon the assumption that the deconvolution must yield a zero-phase result, and the maximum crosscorrelation value (for a phase rotation of 3° applied to the synthetics) was obtained in the Gabor/Burg deconvolution using the hyperbolic smoother. As explained in section 1.2.3, the purpose of deconvolution is to increase the resolution thereby the data is moved toward the zero-phase state. In this matter, Gabor deconvolution performed better in either example, with the boxcar or with the hyperbolic smoother.
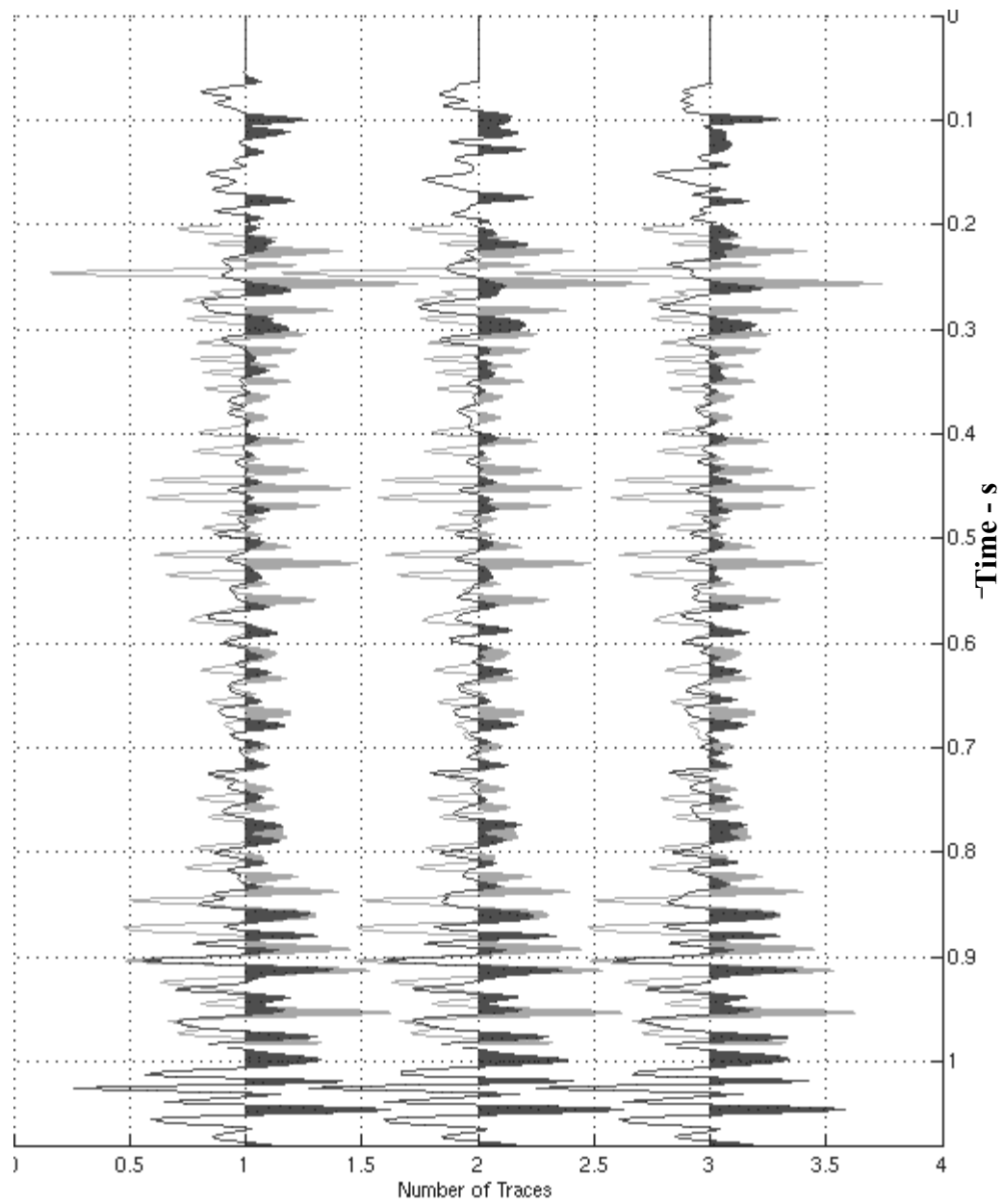
Figure 3.34.: A comparison of the 09-08 synthetic seismogram(light gray) to results from Wiener Spiking deconvolution (dark gray)
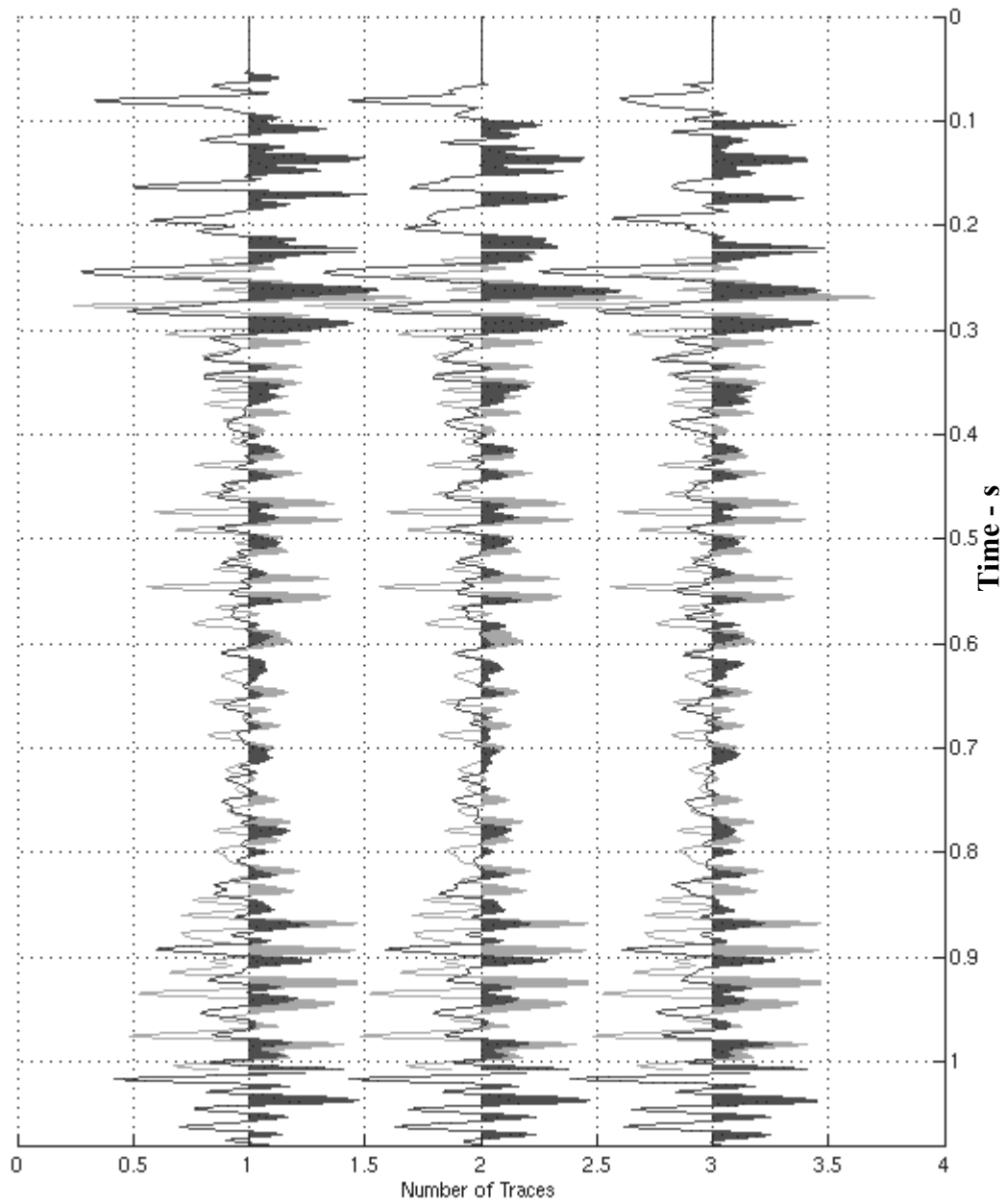
Figure 3.35.: A comparison of the 09-08 synthetic seismogram (light gray) to results from Gabor deconvolution -boxcar smoother- (dark gray).
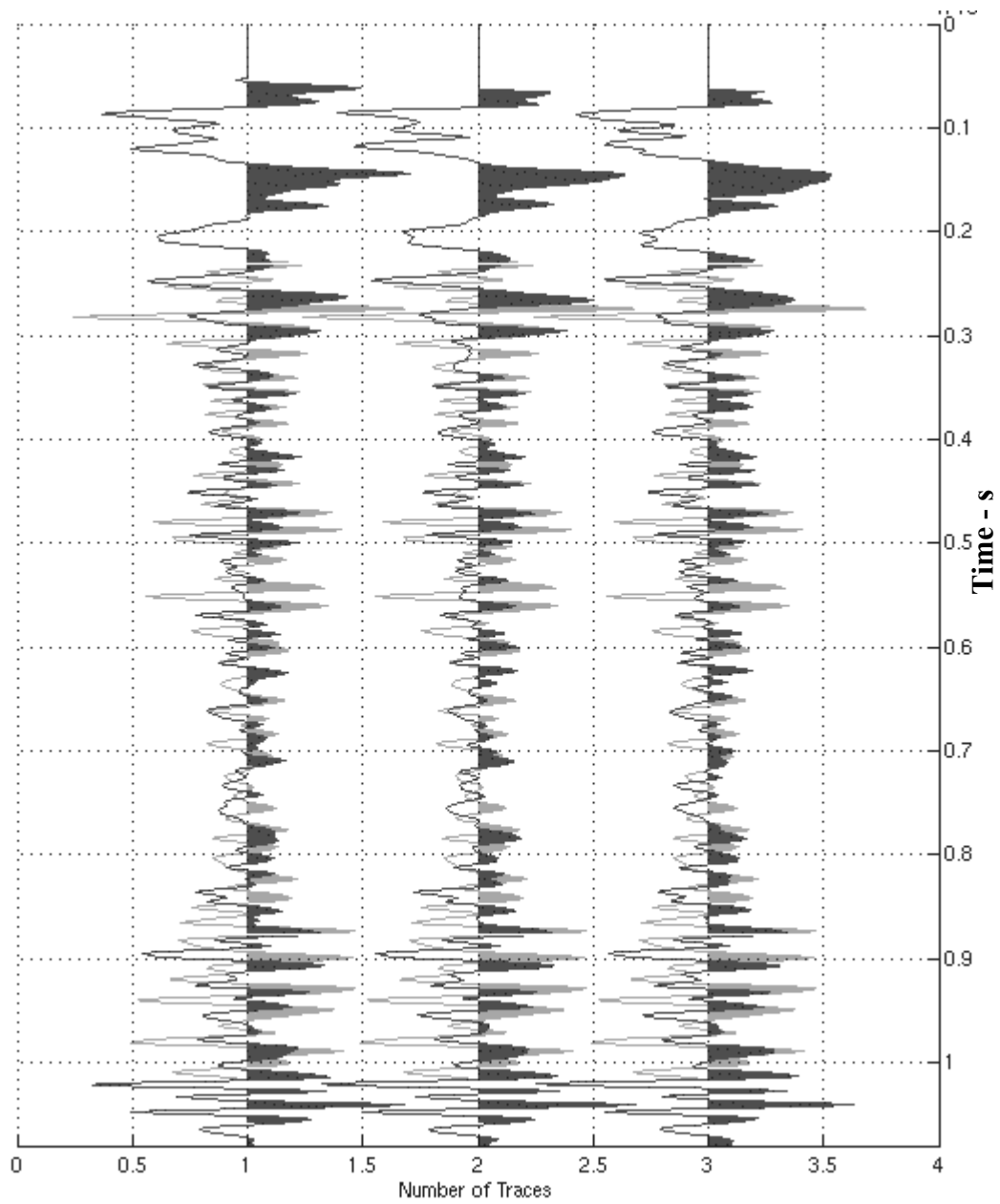
Figure 3.36.: A comparison of the 09-08 synthetic seismogram (light gray) to results from Gabor deconvolution -hyperbolic smoother- (dark gray).

CHAPTER 4

4. WAVELET TRANSFORM WITH APPLICATIONS TO SEISMIC REFLECTION DATA

The wavelet transform (WT) is a relatively new signal analysis and processing approach. There are few applications of the wavelet transform in geophysical data processing. Most of the examples involve data compression (Donoho et al., 1995), but there are also applications to time-frequency analysis, filtering and interpretation using plots (Chakraborty and Okaya, 1994), and phase correction (Rodriguez and Mansar, 1995). The WT of a signal depends on two variables: scale and time. The strength of the WT representation is due to its ability to separate a signal into different scale levels. The result of the wavelet decomposition consists of coefficients that are influenced by local events that can be potentially identified, analyzed, and filtered. In this chapter, the WT is used to increase the resolution of seismic data. Two techniques have been implemented and tested for this purpose, WT filtering by semblance weighting and a method similar to time variant spectral whitening (TVSW) technique, using the WT. In the beginning, a summary of the WT mathematical background will be presented.

4.1 Mathematical background

The WT is, like the Fourier transform, an inner product between the signal and a set of basis functions. The expansion coefficients measure the similarity between the signal and the elementary basis functions. The elementary functions are also called

analysis functions. The result of the inner product represents the expansion coefficient and the set of all expansion coefficients represents the wavelet domain.

There are two types of WT: the continuous wavelet transform (CWT) and the discrete wavelet transform (DWT).

4.1.1 The CWT

The CWT can be thought of as the inner product of the signal with the basis functions $\psi_{a,b}(t)$, (Daubechies, 1992), ($\psi(t)$ is called the mother wavelet).

$$CWT_{(a,b)} = \langle s(t), \psi_{a,b}(t) \rangle = \frac{1}{\sqrt{|a|}} \int_{-\infty}^{\infty} s(t)\, \psi_{a,b}{}^{*}(t)dt. \tag{4.1}$$

In this expression, $\psi_{a,b}{}^{*}(t)$ is the complex conjugate of

$$\psi_{a,b}(t) = \frac{1}{\sqrt{|a|}} \psi(\frac{t-b}{a}), \tag{4.2}$$

where the scale index, a, is ,very roughly, the reciprocal of the frequency whereas b, indicates time shifting (also called translation). For $\psi(t)$ real, $\psi^{*} = \psi$. The normalizing constant $a^{-1/2}$ is chosen so that the total energy of the wavelet in the time domain is equal to the energy in the frequency domain. The wavelet energy can be expressed in the form

$$\left\| \psi_{(a,b)} \right\|^{2} = \int_{-\infty}^{\infty} |\Psi(\omega)|^{2} d\omega = \int_{-\infty}^{\infty} |\psi(t)|^{2} dt, \tag{4.3}$$

where the $\|\psi_{(a,b)}\|$ represents the Euclidean norm for L^{2} functions. Equation (4.3) represents Parseval's theorem applied to the wavelet and states that the total energy should be the integral of $|\Psi(\omega)|^{2}$, (where $\Psi(\omega)$ is the Fourier spectrum of the wavelet)

over all frequencies and should equal the total energy of the wavelet in the time domain. This property can be extended to the signal in the wavelet domain (Qian and Chen, 1996)

$$\int_{-\infty}^{\infty} |s(t)|^2 = \frac{1}{C_\psi} \int_{-\infty}^{\infty} \int_{-\infty}^{\infty} \frac{|CWT_{(a,b)}|}{a^2} da\,db , \tag{4.4}$$

where C_ψ should satisfy the admissibility condition given by:

$$C_\psi = \int_{-\infty}^{\infty} \frac{|\Psi(\omega)|^2}{|\omega|} d\omega < \infty . \tag{4.5}$$

The Parseval's theorem applied to the WT states that the weighted energy of the signal in the wavelet domain is equal to the energy of the signal in the time domain. When *a* is small, which corresponds to small support length, the wavelet transform picks up higher frequency components. If the admissibility condition is not satisfied the reconstruction is not possible because the inverse wavelet transform will diverge (Qian and Chen, 1996).

All coefficients of the CWT measure the closeness of the signal to the wavelet at the current scale. If the signal has a major component of the frequency corresponding to the current scale, then the wavelet at the current scale will be similar or close to the signal at the particular location where this frequency component occurs. Therefore, the CWT coefficient computed at this point in the time scale plane will be a relatively large number. The definition of the CWT shows that the wavelet analysis is a measure of similarity between the basis functions (wavelets) and the signal itself. Here, the similarity is in the sense of similar frequency content (Qian and Chen, 1996).

The inverse transform of the CWT is given by :

$$s(t) = \frac{1}{\sqrt{C_\psi}} \int_{-\infty}^{\infty} \int_{-\infty}^{\infty} \frac{1}{\sqrt{a}} \psi(\frac{t-b}{a}) \frac{1}{a^2} CWT_{(a,b)} dt\,da . \tag{4.6}$$

A perfect reconstruction of the signal is possible, but depends on the choice of the elementary function $\psi_{a,b}(t)$. The CWT is highly redundant and therefore is computationally time consuming. The DWT computes only those scales and translations needed for a complete representation and reconstruction of the signal. For this reason, the DWT is more efficient and has been used in this experiment.

4.1.2 The DWT and multi-resolution analysis

In the discrete wavelet transform (DWT), the dilation parameter a and the translation parameter b take only selected discrete values. Besides the CWT, another way to introduce wavelets is through multi-resolution analysis (MRA) (Mallat, 1999). The concept of the MRA is the key to the construction of orthogonal wavelet bases and for the fast decomposition of a signal into frequency bands. If $s(t)$ is a signal from a certain subspace denoted by $V_{-1} \in L^2(R)$, a decomposition is performed into a high and low-frequency parts. The low-frequency part, P_0S (called the approximation coefficients) is obtained by an orthogonal projection into a smaller subspace $V_0 \subset V_{-1}$ which contains only the smoothed functions of V_{-1}. The orthogonal complement of V_0 in V_{-1} will be denoted by W_0. The projection of the signal $s(t)$ into W_0 will be denoted by Q_0S (called the detail coefficients). Thus, we have $s(t)= P_0S + Q_0S$ $(V_{-1} = V_0 \oplus W_0)$. The procedure can be repeated to decompose P_0S into a coarser level of approximation and detail and so on. The result is an MRA of $L^2(R)$ (the space of finite energy functions) defined as a sequence of closed subspaces V_k of $L^2(R)$, $k \in Z$, with the following properties:

1. $... V_2 \subset V_1 \subset V_0 \subset V_{-1} \subset V_{-2} ... \subset L^2(R)$;

2. $s(t) \in V_k \Leftrightarrow s(2^k t) \in V_0$;

3. $s(t) \in V_k \Leftrightarrow s(t+1) \in V_k$;

4. $\bigcup_{j=-\infty}^{\infty} V_j$ is dense in $L^2(R)$ and $\bigcap_{j=-\infty}^{\infty} V_j = \{0\}$;

5. A scaling function $\phi \in V_0$, with a non vanishing integral exists such that the set of $\{\phi(t-l) \mid l \in Z\}$ is an orthonormal basis for V_0.

In consequence there exist ψ such that

$$P_{V_k-1}S = P_{V_k}S + \sum_{k \in Z}\langle S, \psi_{j,k}\rangle \psi_{k,j} \tag{4.7}$$

holds (Daubechies, 1992).

Some of these properties are more of a technical nature. The essential properties are (2) which expresses the fact that all spaces of an MRA are scaled versions of the base space V_0 and (5) which implies that ϕ and ψ should be in a complementary relationship. Since $\phi \in V_0 \subset V_{-1}$ and the $\phi_{-1,l}(t) = 2^{1/2} \phi(2t-l)$ is an orthonormal basis for V_{-1} , there exist $\alpha_l = 2^{1/2}\langle \phi, \phi_{-1,l}\rangle$ so that $\phi(t) = \Sigma_l \phi(2t-l)$. This leads to the relation between ϕ and ψ, $\psi(t) = \Sigma_l (-1)^l\alpha_{-l+1} \phi(2t-l)$ (Daubechies, 1992). The space V_0 itself is spanned by shifted versions of the so-called scaling function, ϕ.

To understand the MRA concept the Haar function is convenient. The Haar scaling function is defined as $\phi(t) = 1$ for $0 < t < 1$, $\phi(t) = 0$ otherwise. Then there exists a function ψ and a family ψ_{kj} defined by

$$\psi_{k,j}(t) = 2^{-\frac{k}{2}}\psi(2^{-k}t - j). \tag{4.8}$$

For k fixed, the ψ_j 's are orthonormal bases (they never overlap) of the orthogonal complement W_k of V_k in V_{k-1}. In Figures 4.1a and 4.1b the Haar scaling wavelet and the Haar analyzing function are shown.
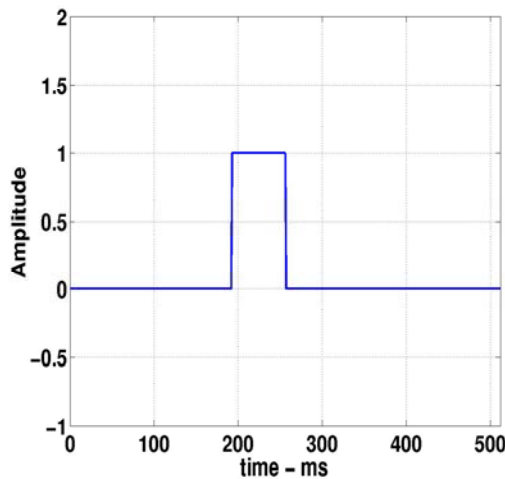

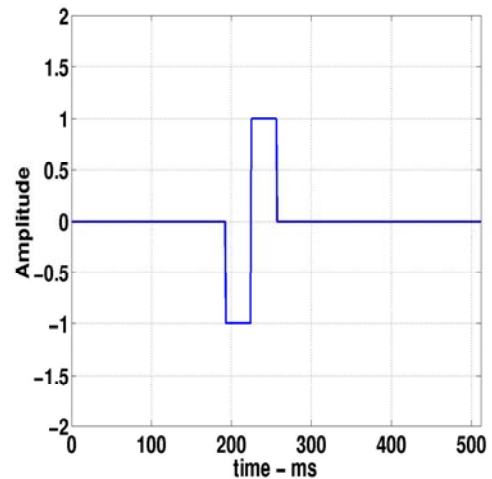Figure 4.1a.: Haar scaling function or father wavelet of an arbitrary scale and position.

Figure 4.1b.: Haar analyzing function or mother wavelet, at the same scale and position as the father wavelet.

The formula (4.8), represents a scaled version the of mother wavelet $\psi(t)$. The set $\psi_{k,j}(t)$ is a family of wavelet functions generated from the mother wavelet through dilatation determined by the parameter k (a in the continuous case) which governs frequency and shift controlled by the parameter j which determines translation (b in the continuous case). For any scale 2^{-k}, $\{\psi_{k,j}(t)\}_{k\in Z}$ is an orthonormal basis of W_k. For all scales, $\{\psi_{k,j}(t)\}_{k\in Z}$ is an orthonormal basis of $L^2(R)$, (Mallat, 1999).

Similarly, $\phi_{k,j}(t)$, represent the scaling functions. The family $\{\phi_{k,j}(t)\}_{k\in Z}$ is an orthonormal basis of V_k, (Mallat, 1997).

The functions in the discrete case $\phi(t)$ and $\psi(t)$ are also used to measure the signal's local behavior, (as only "$\psi(t)$ " in the continuous case) that is: the scaling

functions $\phi(t)$ and analyzing wavelets $\psi(t)$ are localized in both time and frequency. All the functions that are used are the dilated (or compressed) and shifted versions of the mother wavelet and scaling function. In addition, $\phi(t)$ should be consistent with the averaging interpretation, that is,

$$\int \phi(t)dt = 1, \tag{4.9}$$

and the analyzing wavelet should be consistent with the differencing interpretation, ($\psi(t)$ is a function of zero mean),

$$\int \psi(t)dt = 0. \tag{4.10}$$

These properties can be observed in Figures 1a, and 1b of the Haar wavelets. There are infinitely many function families that satisfy these conditions and can be used as a wavelet basis. The selection of a particular basis is a major and difficult decision in a practical wavelet application.

Using the MRA concept, the DWT can be implemented by high- and low-pass filters that successively decompose the input signal by dyadic downsampling (decimated) convolutions (Mallat, 1999). An arbitrary signal can be represented in such way by the formula

$$s(t) = \sum_j c_j^{(k)} \phi_j^{(k)}(t) + \sum_k \sum_j d_j^{(k)} \psi_j^{(k)}(t). \tag{4.11}$$

For k (level of decomposition) fixed, there are two types of wavelet coefficients, c_j and d_j,

$$c_j^{(k)} = \langle s, \phi_{k,j} \rangle = \sum_{l \in Z} h_{l-2j} \langle s, \phi_{k-1,l} \rangle = \sum_{l \in Z} h_{l-2j} c_l^{(k-1)}, \tag{4.12}$$

$$d_j^{(k)} = \langle s, \psi_{k,j} \rangle = \sum_{l \in Z} g_{l-2j} \langle s, \phi_{k-1,l} \rangle = \sum_{l \in Z} g_{l-2j} c_l^{(k-1)}. \tag{4.13}$$

If $k = 1$, c_j^1 represent the coefficients of the projection P_1S of $s(t)$ in the space V_1 and d_j^1 represents the coefficients of the projection Q_1S of $s(t)$ in the space W_1 (Keller, 2000).

The variables of *g* and *h* represent the coefficients of the high respectively low pass filters. The coefficients $d_j^{(1)}$ are already a final result. They are the coefficients of the wavelet spectrum of *s*(*t*) on the scale 1. In order to obtain the wavelet spectrum on the coarser scales 2, 3, 4 and so on, the procedure will be repeated for c_j^1. The two equations (4.12) and (4.13) constitute the Mallat's algorithm for the fast computation of the wavelet coefficients of an arbitrary signal, *s*(*t*). This procedure can be described using decomposition operators *H* and *G,* denoting the signal by *c* (for level 0 of decomposition)

$$H : applied \rightarrow c = \{(Hc)_j = \sum_{l \in Z} h_{l-2j} c_l\}, \tag{4.14}$$

$$G : applied \rightarrow c = \{(Gc)_j = \sum_{l \in Z} g_{l-2j} c_l\}. \tag{4.15}$$

This leads to the scheme for the computation of the wavelet spectrum shown in Figure 4.2. In this example the decomposition goes up to the fourth level, with level 1 containing the highest frequency components.
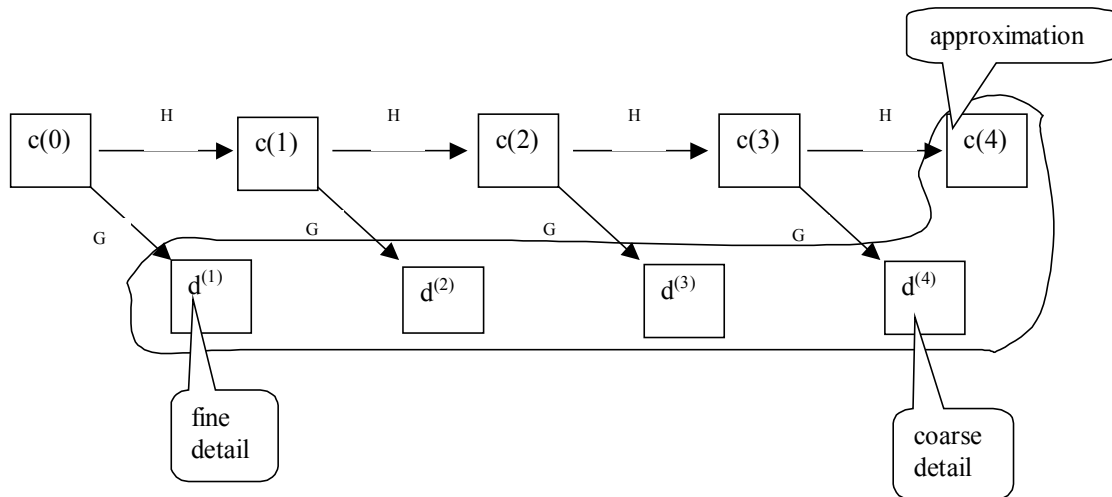

Figure 4.2.: Scheme of the wavelet domain for four levels of decomposition. Those boxes inside the curve form the discrete wavelet transform (DWT).

This transform is invertible and the signal is recovered by

$$c_j^{(0)} = \sum_{l \in Z} (c_l^{(1)} h_{2l-j} + d_l^{(1)} g_{2l-j}). \qquad (4.16)$$

4.2 Applications of the wavelet transform in seismic processing

Two methods of seismic signal enhancement using the WT are investigated in this section. The first method is similar to the conventional time variant spectral whitening (TVSW) technique. The second method is an original filtering technique applied in the wavelet domain. Both methods are designed to increase the resolution of seismic data.

4.2.1 Basis selection and decomposition level

For applications, such as data compression or noise removal, there are preferred classes of wavelet bases, which approximate the signals with few non-zero wavelet coefficients (Mallat, 1999). In addition, wavelet bases with this property offer the advantage of less computational time. The wavelet bases must be chosen, such that, in the wavelet domain a large number of coefficients that are close to zero must be produced. In this thesis a different criteria in choosing the optimum wavelet basis was used.

The Battle-Lemarie (Daubechies, 1992) wavelet was used in this research because of its good localization in time and frequency. The wavelet transform provides a time-frequency picture and a good localization in both variables is desired. The Haar wavelet described in the representation of the multiresolution analysis has a poor localization in frequency. Figures 4.3a and 4.3b show the amplitude spectrum of the analysing and the scaling Haar function.
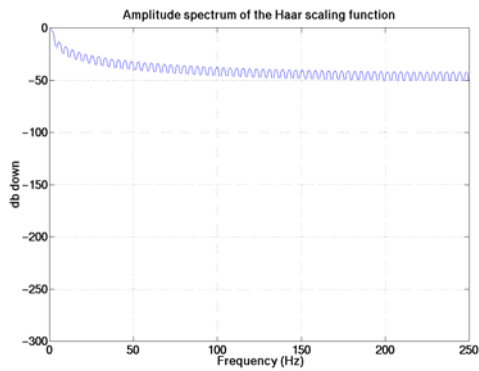
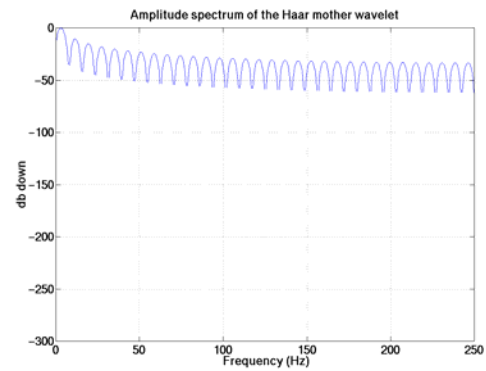Figure 4.3a.: Haar scaling function in frequency domain.

Figure 4.3b.: Haar analysing function in frequency domain.

The Battle-Lemarie wavelets (in Figures 4.4a and 4.4b) are spline functions with fast exponential decay in time. Figures 4.4c and 4.4d show the representation of the Battle-Lemarie scaling and analysing functions in frequency domain. Battle-Lemarie wavelets are used in this experiment because in the frequency domain they have a good localization.
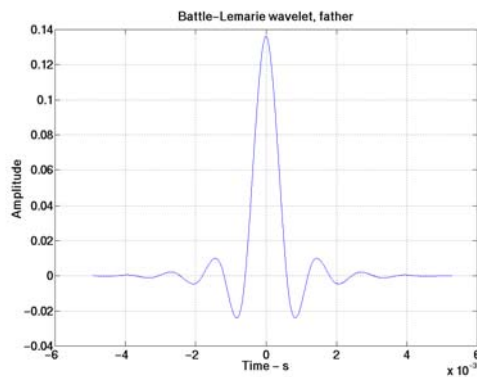

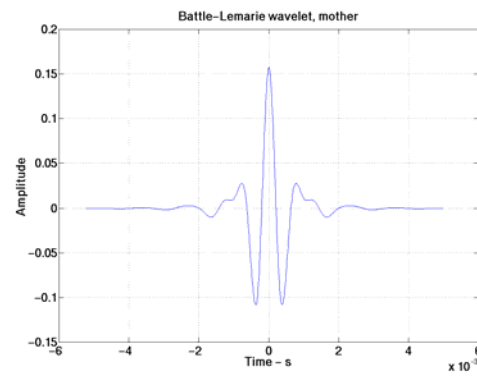
Figure 4.4a.: Battle-Lemarie scaling function.

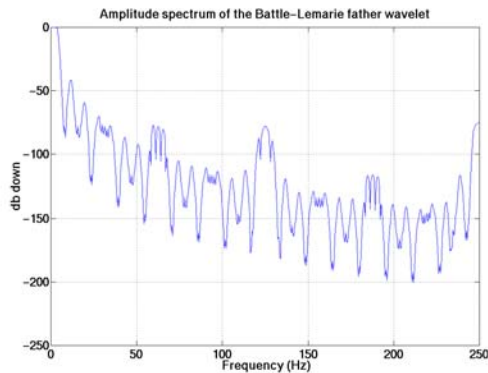Figure 4.4b.: Battle-Lemarie analysing function.

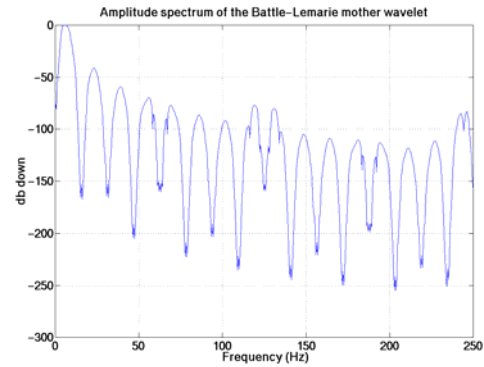Figure 4.4c.: Battle-Lemarie scaling function in frequency domain.

Figure 4.4d.: Battle-Lemarie scaling function in frequency domain.

4.2.2 Example on synthetic trace of the WT whitening method

First, a brief description of the conventional TVSW technique is provided, and next the new filtering method based on the WT will be investigated. This method is tested, along with the conventional TVSW method for comparison on the synthetic model used to test the Gabor deconvolution in section 3.2.2.

The TVSW technique was developed to compensate for the frequency attenuation effects described in section 2.1. TVSW uses a complete set of band-pass filters to decompose a signal (presumed to have the amplitude spectrum attenuated toward the high frequencies) into a set of narrow band signals. To describe the decay rates for each frequency band, the envelope (as described in section 2.2.1) of the band-pass filtered trace is computed (Yilmaz, 1987). The next step is to calculate the inverses of these envelope functions and to apply them to the (respectively) narrowband signal. The last step is to sum the resultant signals back together to form an enhanced signal with a flat spectrum (this algorithm is illustrated in diagram 4.5). The result of the TVSW technique

is similar to the zero-phase deconvolution, although there is no theoretical proof of this (Yilmaz, 1987).
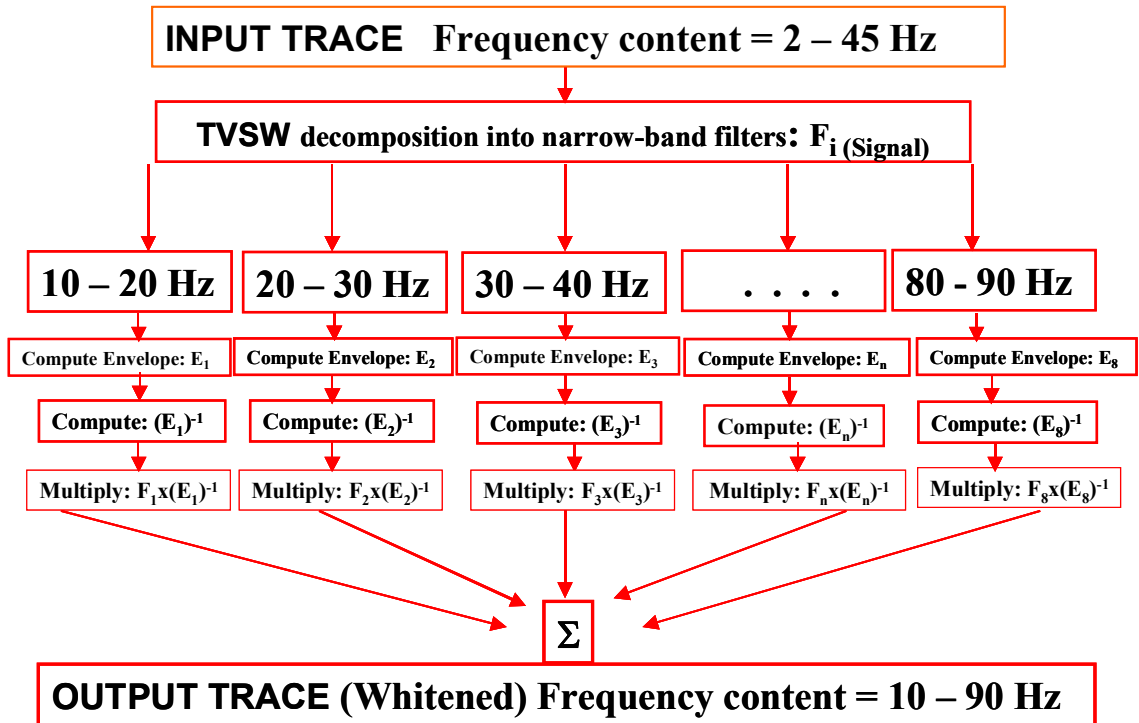
Figure 4.5.: The time variant spectral whitening (TVSW) algorithm.

In this section, the DWT is used to achieve a kind of TVSW technique described above. As explained in section 4.1.2 the wavelet domain provides a time series containing the detail found in the signal at that scale. For each scale level, the corresponding signal is divided by a smoothed version of its Hilbert envelope, then the enhanced signal is inverse transformed from the wavelet domain to the time domain (see Figure 4.6).

Figure 4.6.: The wavelet transform spectral whitening (WTSW) algorithm.

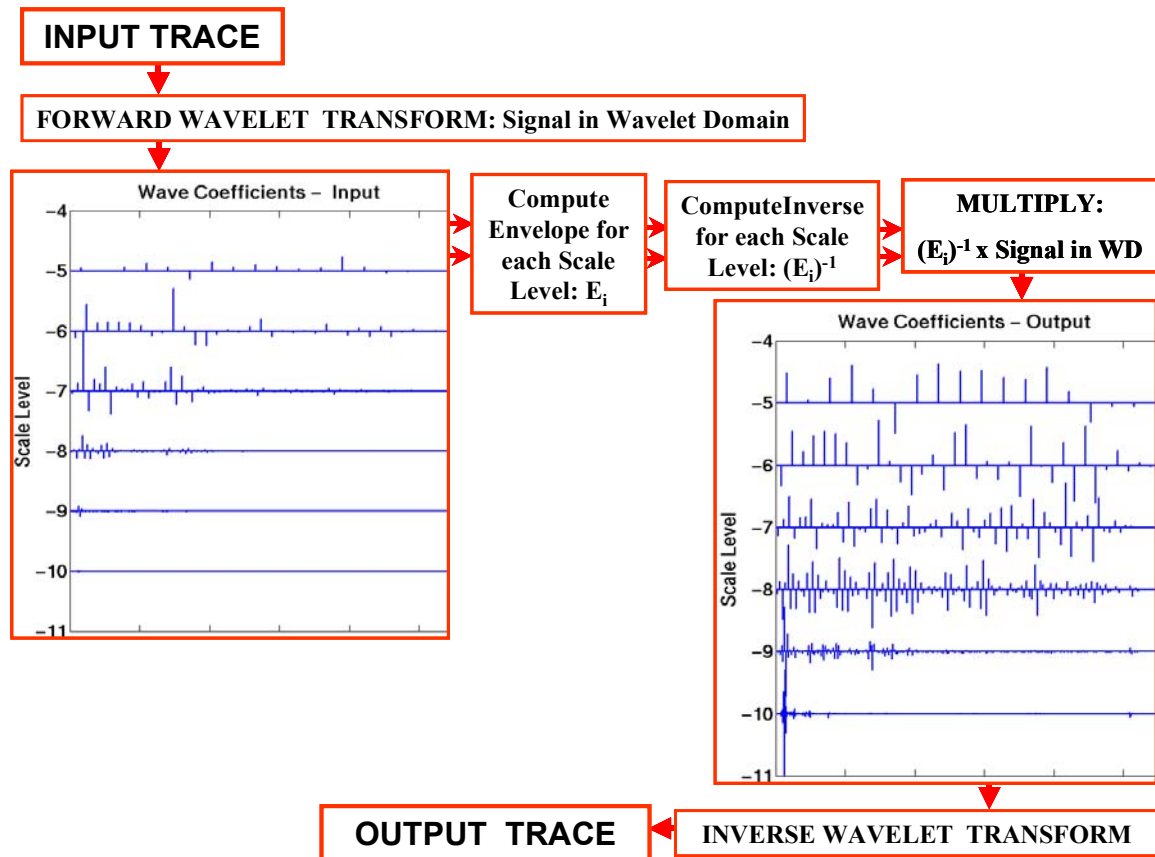In Figure 4.7, the reflectivity series is at position A. Position B is a filtered version of this reflectivity with a bandwidth of 10-90 Hz. The result of the conventional TVSW technique is at position C. The result of the WT spectral whitening (WTSW) is at position D. At position E is the input trace (Q=25). As explained in section 3.4, in the boxcar smoother example, the TVSW technique (trace C) has leveled all the three intervals encountered in the reflectivity series (high, low the moderate amplitude intervals, compare to trace C). In the WT whitening case, the low amplitude interval (from 1.5 to 3 seconds) was better restored and can be identified after the high amplitude interval (from 0 to 1.5 seconds), although the moderate amplitude interval (from 3 to 4 seconds) cannot be recognized.
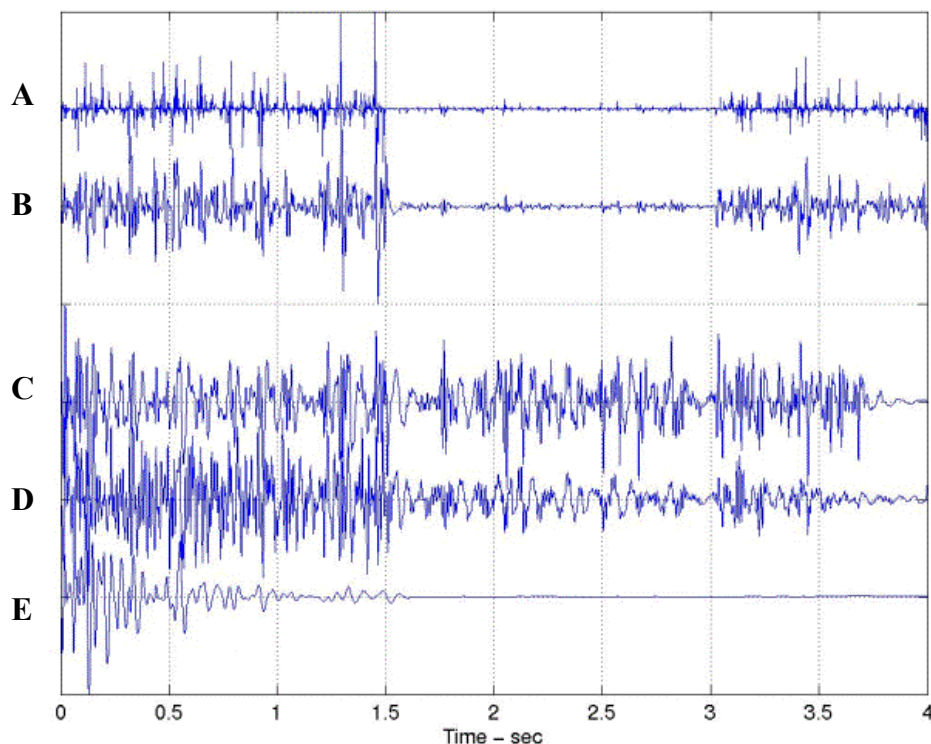
Figure 4.7.: Trace **A** is the reflectivity series. Trace **B** is a bandlimited version of trace **A**, for comparison to the whitened traces. The result of the time variant spectral whitening is represented by **C.** The wavelet transform spectral whitening method yields trace **D**. Trace **E** represents the attenuated trace (input trace), Q=25.

There is no apparent advantage of the WTSW method compared to the TVSW, however, the WTSW is a novel approach in introducing the WT to seismic data processing.

4.2.3 The WT filtering by semblance weighting

The WT is used here to filter seismic data in a time-frequency sense. The primary consideration is how can a set of weights be chosen to apply to the WT coefficients. There are infinitely many possible schemes for this. In this example the use of a time-domain semblance measure to prescribe the weights is investigated.

The filtering was applied to a final stack of a 10Hz array of Blackfoot data (illustrated in Figure 4.8), recorded in the Blackfoot field, same data used to test the Gabor deconvolution, in section 3.5, here is represented from left to right.

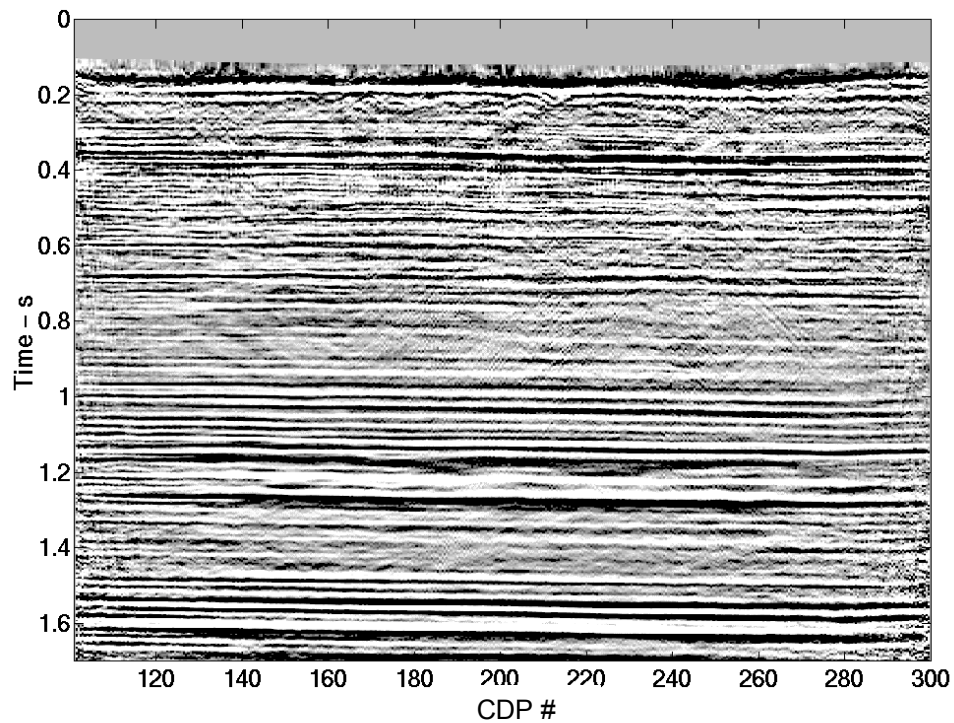Figure 4.8.: The Blackfoot stacked section.

In this study, the following procedure was used for filtering.

1. Select the desired wavelet basis and a level of decomposition.

2. Calculate multichannel semblance coefficients with smoothing operators of different sizes for the stacked section.

3. Apply the WT to the seismic traces from the stacked section. The decomposition

level in this example is 2.

4. Apply the WT to the semblance traces. This should extend to the same level of decomposition as for the seismic traces, respectively 2 in this example.

5. Weight the wavelet coefficients of the seismic traces with the wavelet coefficients of the semblance traces, that is multiply their wavelet transforms together.

6. Inverse transform the filtered wavelet coefficients.

7. Apply a time variant spectral whitening (TVSW) operator (as described in section 4.2.2.) to the WT filtered stack.

Using Mallat's algorithm, the level of decomposition was chosen after considerable experimentation. The level of decomposition used for this experiment was 2. For the level 1 of decomposition, we get 1 set of decomposition coefficients and one set of detail coefficients. The highest frequencies of the signal lays in the detail part of decomposition whereas the lowest frequencies in the approximation part of the decomposition. For the level 2 of decomposition the approximation coefficients of the level 1 which represents a smoothed version of the original signal downsampled by 2 is again decomposed into another level of detail coefficients which contain the highest frequencies for this level and a set of approximation coefficients. Level 2 implies that the trace in wavelet domain is composed of the detail coefficients of level 1, detail coefficients of level 2 (coarser than 1), and approximation coefficients of level 2.

The Blackfoot stacked section decomposed for level 2 is illustrated in Figure 4.9.
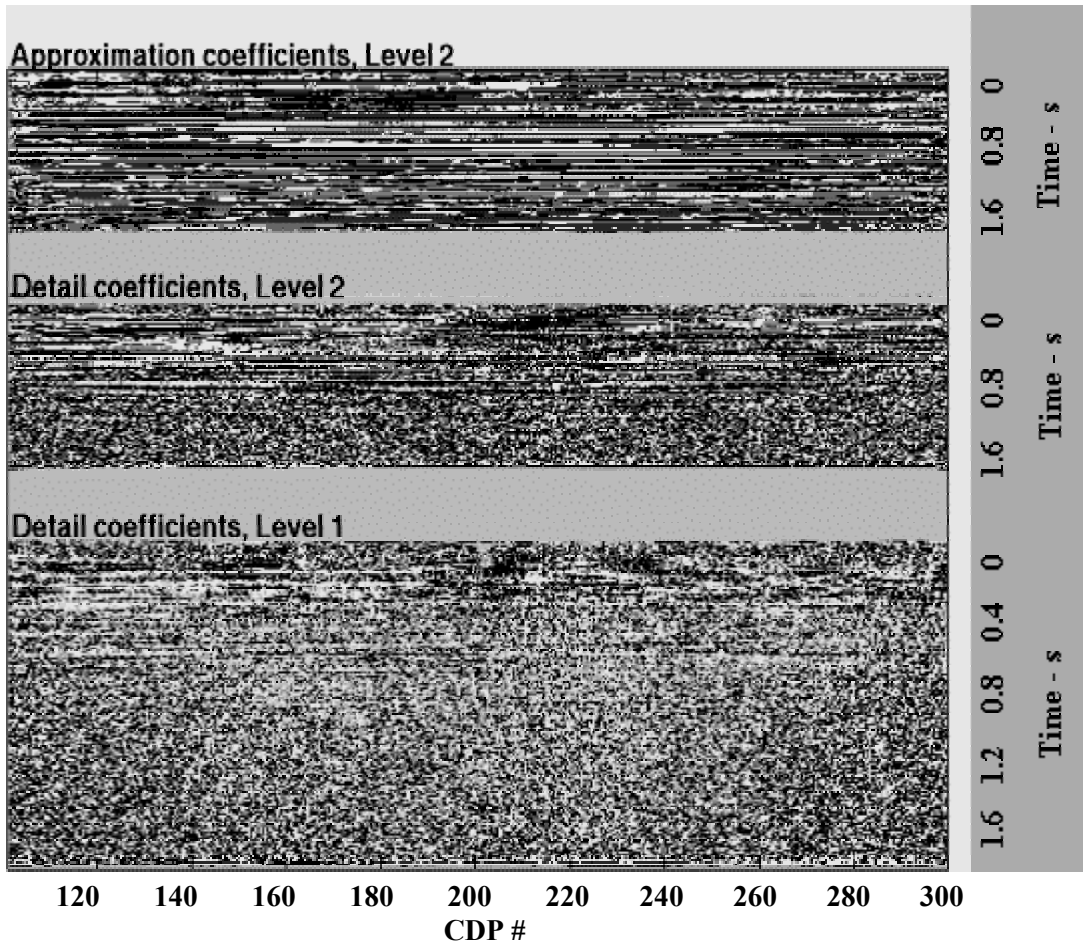
Figure 4.9.: The Blackfoot Stacked section decomposed with Mallat's algorithm to level 2, with the Battle-Lemarie wavelet.

The semblance coefficients are given by the formula

$$\sigma(x,t) = \frac{1}{\Delta} \frac{[S \bullet a]^2}{S^2 \bullet a}(x,t) ,$$

(4.17)

where a is a small averaging function, S is the seismic data matrix, Δ is a normalizing constant that depends on a, and $\bullet$ denotes a 2D convolution. In this study , a was a 2D boxcar n traces wide and N samples high.

Currently, the coherence measurements are used to detect stratigraphic features and faults ,therefore, is one of the most important properties of seismic reflection data (Bahorich and Framer, 1994). Among the formulations that exist for obtaining coherence estimates are cross correlation, semblance, and eigendecomposition of the data covariance matrix (Gzerszkorn and Marfurt, 1999). In the Blackfoot experiment a semblance algorithm was used. The semblance, as a measure of multichannel coherence can be calculated using different sizes of an operator. An operator higher than 31 samples (15 ms) in the case of the Blackfoot data will blur stratigraphy associated with both deeper and shallower times about the zone of interest. Of the same importance is the width of the semblance operator for the lateral extent of the interest zones. In the case of Blackfoot data, a window wider than 25 traces will also smear the lateral extent of the zone of interest (i.e. the Glauconitic incised valleys). The semblance operators with good results in this experiment are: 9 x 3, 3 x 9, and 5 x 15.

Subsequently, the sections 3,4,5,6 and 7 from the methodology were applied to the Blackfoot data.

4.3 Conclusions of the WT filtering by semblance weighting

Figure 4.10 illustrates the Blackfoot stacked section after the TVSW was applied. In Figure 4.11, a semblance operator of 9x3 served in filtering the data. The second semblance operator used was a 3x9 boxcar. Figure 4.12 shows similarities with Figure 4.11, that is the major events have been preserved and the non-coherent noise has been suppressed. The results of the WT filter that uses a 5x15 semblance operator are the final test in this study (in Figure 4.13). The valley of the Glauconitic channel can be distinguished between the CDP numbers from 170 to 180 in all Figures (4.10 to 4.13.) at around 1.19 seconds.

In this example, the WT filtering technique was applied to the final stack followed by TVSW technique. The resolution seems to be improved as a consequence of the WT filtering by semblance weighting. Prior to applying this method, it is essential to eliminate the coherent noise such as multiples and shallow reflections. This technique increases the resolution of subtle stratigraphic features, such as Glauconitic channels.
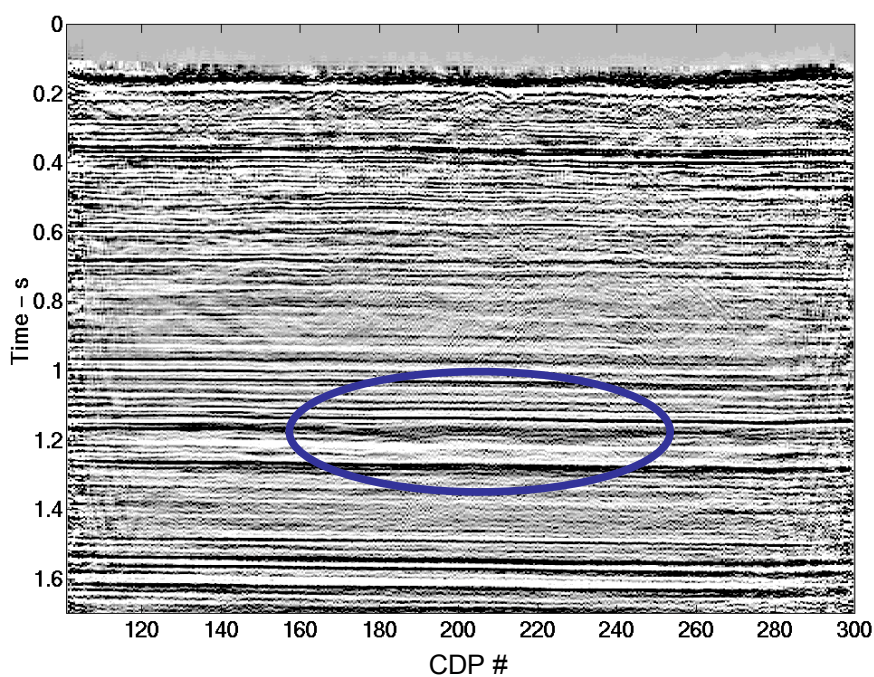
Figure 4.10.: Similar to Figure 4.8 except that the data has been through TVSW. The Glauconitic channels can be identified in the black oval, between CDP's # 180 - 240.

Figure 4.11.: The TVSW was applied after the WT filtering (9x3 semblance operator) (To be compared with Figures 4.10, 4.12, and 4.13). The Glauconitic channels can be identified in the black oval, between CDP's # 180 - 240.

Figure 4.12.: Same as Figure 4.11, but the semblance operator was 3x9 (To be compared with Figures 4.10, 4.11, and 4.13).

Figure 4.13.: Stacked data of Figure 4.8. The TVSW technique was applied after the WT filtering (5x15 semblance operator). (To be compared with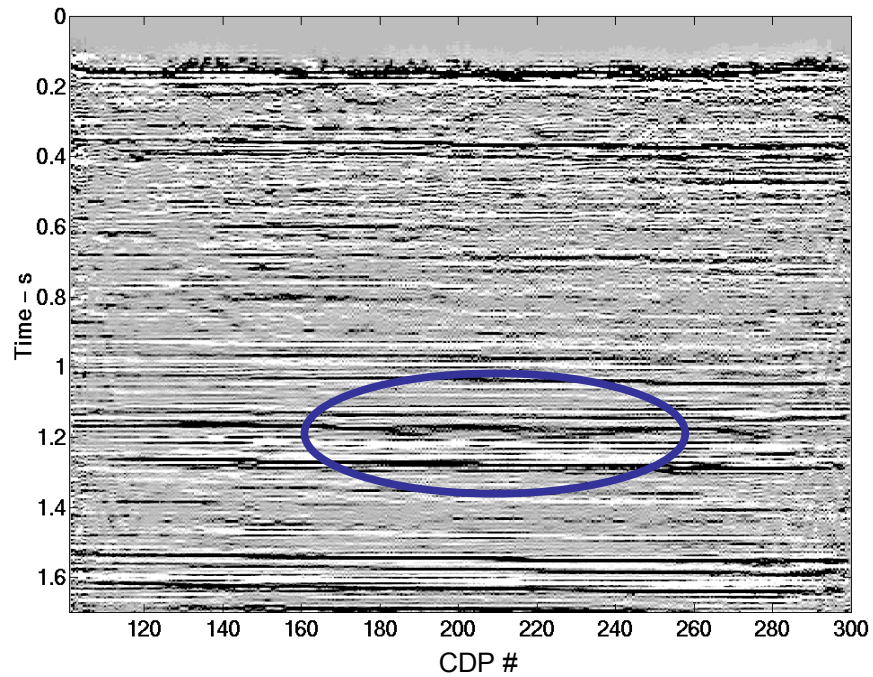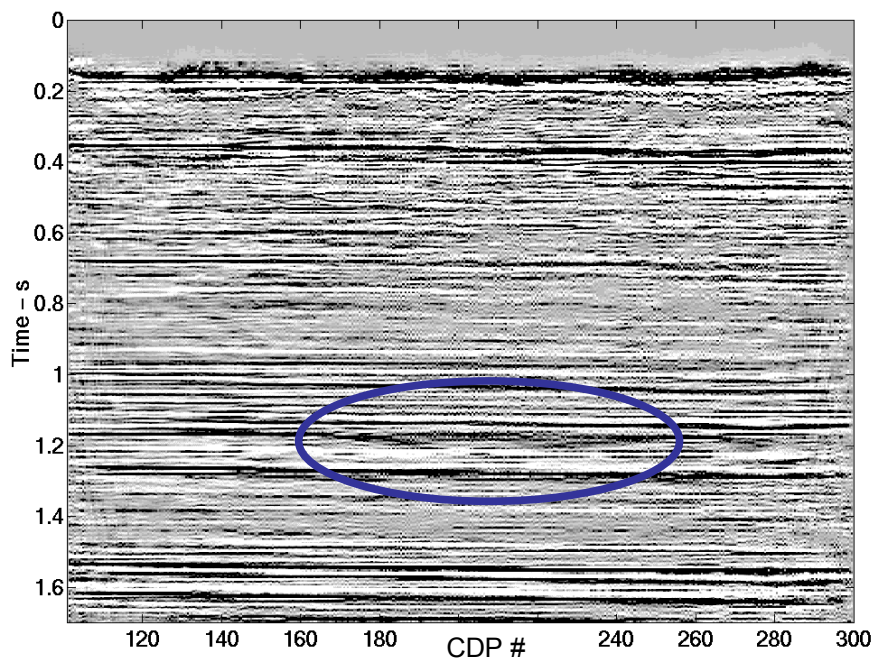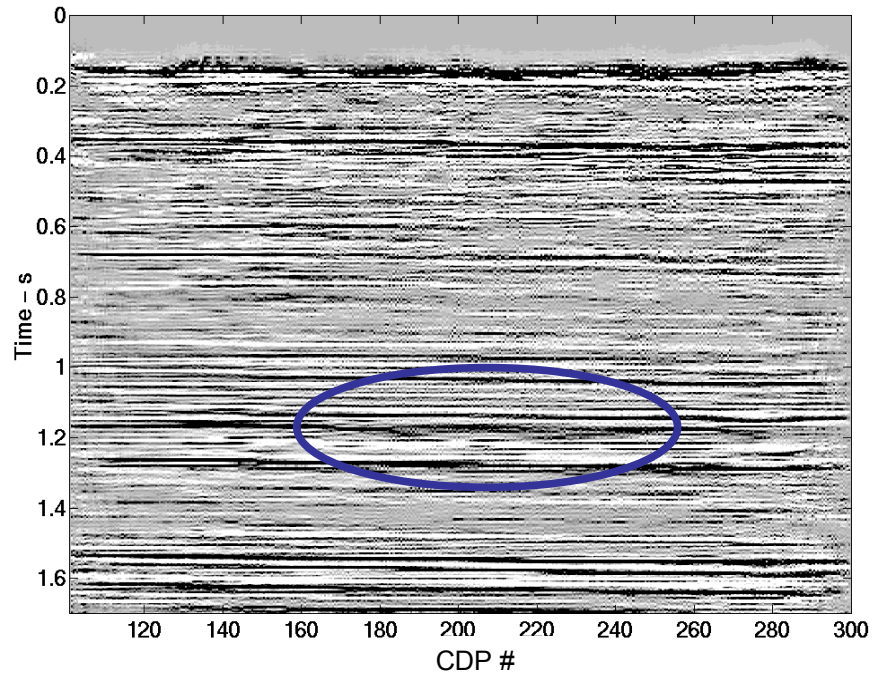 Figures 4.10, 4.11, and 4.12). The Glauconitic channels can be identified in the black oval, between CDP's # 180 to 240.

CHAPTER 5

5. CONCLUSIONS AND FUTURE WORK

5.1 Conclusions

The main purpose of this work was to investigate and improve new methods to compensate for the nonstationarity of the seismic signals, as well as to enhance the time resolution. This goal is achieved by deconvolution (which approximately corrects for the source signature and attenuation effects) in the Gabor deconvolution case, and by filtering, using a set of semblance weights in the wavelet domain, in the wavelet transform filtering case. The Gabor and wavelet transform were employed in this research and the mathematics behind these methods was studied.

The classical approach to overcome the decay in time of a signal uses the stationary convolutional model and the time domain Wiener spiking deconvolution described in chapter 1 and additional methods, such as successive time gates in calculating the deconvolution operator, the TVSW technique, and the inverse Q filtering. As an alternative to these methods used currently in the industry the Gabor deconvolution (based on Gabor transform) provides superior results in enhancing the resolution of the seismic data restoring the relative amplitudes (in the hyperbolic smoothing case) encountered in seismic signals. The more general nonstationary convolutional model employed in the Gabor deconvolution case was reviewed and explained in comparison to the particular stationary convolutional model.

The Gabor deconvolution uses a data-dependent operator, which is derived from the Gabor magnitude spectrum. The Gabor magnitude spectrum preserves the time-variant character of a given signal and thus the Gabor deconvolution is a proven flexible,

self-adaptive method, which can handle highly attenuated signals as well as moderately attenuated signals.

The first step in the Gabor deconvolution algorithm is to compute the magnitude spectrum of the input trace. In the Gabor domain, the magnitude spectrum of a trace contains the reflectivity, the attenuation and the source signature information. The Gabor magnitude spectrum is initially smoothed in order to suppress the reflectivity information and thus to isolate only the source signature and the attenuation function which are inverted to form the deconvolution operator. Then the deconvolution operator is applied to the magnitude spectrum of the trace to recapture the reflectivity information, or more precisely, an approximation of the reflectivity series. The smoothing technique is fundamental for the result of the deconvolution. From the two smoothing techniques, that were investigated in the Gabor deconvolution case, the boxcar smoother was previously used by Schoepp (1998) in the mixed domain nonstationary deconvolution case (explained in section 3.1), while the hyperbolic smoother was derived and applied for the first time in this thesis. In either case, the amplitude spectrum of the deconvolution operator can be computed as a minimum-phase operator (using the Hilbert transform) or left as zero phase. The advantage of the hyperbolic smoother over the boxcar smoother resides in the fact that the hyperbolic smoother adapts better to the constant Q model of attenuation (described in section 2.4) in the sense that it selects the attenuation information more accurately. Thus, for an exponentially decaying signal, the hyperbolic smoother offers a physically valid result (it removes the reflectivity information from the deconvolution operator), whereas in the boxcar smoother case, an imprint of the reflectivity is still present in the deconvolution operator. This imprint of the reflectivity series in the deconvolution operator yields a biased result, similar to an AGC applied to restore the attenuated amplitude.

In the wavelet transform case, a new filtering technique has been tested. This method is based on wavelet transform and semblance measurements on a stacked section. The resolution seems to be improved as a consequence of this technique. Prior to

applying the WT filtering by semblance weighting it is essential to eliminate the coherent noise such as multiples and shallow reflections. In a free coherent noise environment, this technique increases the resolution of subtle stratigraphic features, such as Glauconitic channels, by suppressing random noise.

5.2 Future work

Even though the basic work was introduced in this thesis, in the Gabor deconvolution case, I would propose, for the real data that an automatic first-break picking be used prior to designing the deconvolution operator. By using the first break picking the deconvolution operator becomes offset dependent and the noise (if present) before the first break does not contaminate the process.

In the wavelet transform case, the two-dimensional wavelet transform can be employed to analyze separately, and if desired, filter, different events (vertical, horizontal and dipping), before stack, as well as after stacking. Also, the wavelet transform can be introduced in the Gabor deconvolution algorithm as a third method to smooth the magnitude Gabor spectrum, using a certain level of approximation.

REFERENCES

Aki, K. and Richards, P.G. 1980, Quantitative seismology, theory and methods: W. H. Freeman and Co., volume 1.

Bahorich, M.S. and Farmer S.L., 1995, 3-D seismic discontinuity for faults and stratigraphic features: the coherence cube, 65th Ann. Internat. Mtg, Soc. Expl. Geophys., Expanded Abstracts, 1532-1534.

Barnes, A.E., 1993, Instantaneous spectral bandwidth and dominant frequency with applications to seismic reflection data, Geophysics, **58**, 419-427.

Berkhout, A.J., 1974, Related properties of minimum-phase and zero-phase time functions, Geophysical Prospecting, **24**, 863-709.

Berkhout, A.J., 1996, Seismic resolution: a key to detailed geologic information, in Deconvolution 2, Robinson, E.A. and Osman-Osman, M., Eds., Society of Exploration Geophysicists Geophysics Reprint Series, **17**, 51-55.

Bracewell, R. N., 1965, The Fourier transform and its applications: McGraw-Hill.

Brigham, E.O., 1974, The Fast Fourier Transform: Prentice Hall Signal Processing

Chakraborty, A. and Okaya, D., 1994, Application of wavelet transform to seismic data, 64th Ann. Internat. Mtg, Soc. Expl. Geophys., Expanded Abstracts, 725-728.

Chakraborty, A. and Okaya, D., 1995, Frequency-time decomposition of seismic data using wavelet-based methods, Geophysics, **60**, 1906 - 1916.

Claerbout, J. F., 1976, Fundamentals of geophysical data processing, with applications to petroleum prospecting: McGraw-Hill.

Cohen, L., 1995, Time-frequency analysis: Prentice Hall Signal Processing

Daubechies, I., 1992, Ten lectures on wavelets: Society for Industrial and Applied Mathematics.

Donoho, P., Ergas, R.. and Villasenor, J., 1995, High-performance seismic trace compression, 65th Ann. Internat. Mtg, Soc. Expl. Geophys., Expanded Abstracts, 160-163.

Gzerstenkorn A. and Marfurt K.J., 1999, Eigenstructure-based coherence computations as an aid to 3-D structural and stratigraphic mapping, Geophysics, **64**, 1468-1479.

Hargreaves, N.D., 1992, Air-gun signatures and the minimum-phase assumption, Geophysics, **57**, 263-271.

Hamilton, E. L., 1972 , Compressional wave attenuation in marine sediments, Geophysics, **37**, 620-646.

Henley, D.C., and Margrave, G. F., 2001, A ProMAX implementation of nonstationary deconvolution, CREWES Research Report, 203-222.

Johnston, D.H., and Toksoz, N.M. Eds, 1981, Seismic Wave Attenuation: Society of Exploration Geophysicists, Geophysics Reprint Series **2**.

Karl, J. H., 1989, An Introduction to Digital Signal Processing: Academic Press.

Keller, W., 2000, Application of Wavelets, Geomatics Engineering 699 Course lecture notes: University of Calgary.

Kjartansson, E., 1979, Constant Q wave propagation, Journal of Geophysical Research, **84**, 4737-4748.

Lay, T. and Wallace T.C., 1995, Modern Global, Seismology: Academic Press.

Leinbach, J. 1996, Wiener spiking deconvolution and minimum-phase wavelets, a tutorial, in Deconvolution 2, Robinson, E.A. and Osman-Osman, M., Eds., Society of Exploration Geophysicists Geophysics Reprint Series, **17**, 51-55.

Mallat, S., 1998, A wavelet tour of signal processing: 2nd ed. Academic Press.

Mallat, S., 1989, Multiresolution approximation and wavelets, Trans. Amer. Math. Soc., **315**, 69-88.

Margrave, G. F., 1998, Theory of nonstationary linear filtering in the Fourier domain with application to time variant filtering: Geophysics, **63**, 244 -259.

Margrave, G. F., 1999, Methods of Seismic data processing, Geophysics 657 Course lecture notes: University of Calgary.

Margrave, G. F. and Lamoureux, M.P., 2001, Gabor deconvolution, CREWES Research Report, 241-276.

Mertins, A., 1999, Signal Analysis; wavelets, filter banks, time-frequency transforms and applications: John Wiley & Sons.

O'Connell, R.J., and Budiansky, B., 1978, Measures of dissipation in viscoelastic media, Geophysical Research Letters, **5**, 5-8.

Qian, S and Chen, D., 1996, Joint Time-Frequency Analysis: Prentice Hall.

Robinson, E.A., 1966, Multichannel z-transforms and minimum-delay: Geophysics, **31**, 482-500.

Robinson, E. A., Osman, O.M., 1996, Introduction to deconvolution, in Deconvolution 2, Robinson, E.A. and Osman-Osman, M., Eds., Society of Exploration Geophysicists Geophysics Reprint Series, **17**, 1-48.

Robinson, E.A. .and Treitel, S., 1980, Geophysical Signal Analysis: Prentice-Hall.

Rodriguez, J.M. and Mansar, S., 1995, Analyzing and correcting seismic phases using the wavelet transform, 58th Ann. Mtg. Eur. Assn. Geosci. Eng., Expanded Abstracts, Session: P187.

Schoepp, A., 1998, Improving seismic resolution with nonstationary deconvolution, M.Sc. thesis, University of Calgary.

Sheriff, R.E., 1991, Encyclopedic dictionary of exploration geophysics: 3rd ed. Society of Exploration Geophysicists.

Sheriff, R.E. and Geldart, L.P., 1995, Exploration Seismology: 2nd ed. Cambridge University Press.

Taner, M.T. and Koehler, F., 1981, Surface consistent deconvolution, Geophysics **46**, 17-22.

Taner, M.T., Koehler, F. and Sheriff, R.E., 1979, Complex seismic trace analysis, Geophysics **44**, 1041-1063.

Yilmaz, O., 1987, Seismic Data Processing: Society of Exploration Geophysicists.

Ziolkowski, A., 1984, Deconvolution: International Human Resources Development.

Ziolkowski, A., 1991, Why don't we measure seismic signatures?: Geophysics, 56, 190-201.